Spring 2023

High-Performance Wide Bandgap Semiconductor Power Modules Enabled by Advanced Two-Phase Mini-Channel Cooling

Bo Tian

Recommended Citation

Tian, B.(2023). *High-Performance Wide Bandgap Semiconductor Power Modules Enabled by Advanced Two-Phase Mini-Channel Cooling.* (Doctoral dissertation). Retrieved from https://scholarcommons.sc.edu/etd/7356

HIGH-PERFORMANCE WIDE BANDGAP SEMICONDUCTOR POWER MODULES ENABLED BY ADVANCED TWO-PHASE MINI-CHANNEL COOLING

by

Bo Tian

Bachelor of Science
Shandong University, 2001

Doctor of Philosophy
Beijing University of Technology, 2010

Submitted in Partial Fulfillment of the Requirements

For the Degree of Doctor of Philosophy in

Electrical Engineering

College of Engineering and Computing

University of South Carolina

2022

Accepted by:

Enrico Santi, Major Professor

Chen Li, Major Professor

Roger Dougal, Committee Member

Adel Nasiri, Committee Member

Jamil A. Khan, Committee Member

Cheryl L. Addy, Interim Vice Provost, and Dean of Graduate School

ACKNOWLEDGMENTS

First of all, I would like to express my sincere gratitude and appreciation to my Ph.D advisor, Dr. Enrico Santi, for his guidance, patience, and support in my doctoral study. I would like to thank my Ph.D co-advisor Dr. Chen Li, his support and encouragement is very important to my research. I'm so lucky with supporting by two great professors.

I would appreciate my committee members, Dr. Roger Dougal, Dr. Adel Nasiri, and Dr. Jamil A. Khan for their invaluable guidance and help in my research.

I would also like to thank all friends and colleagues in power electronics group and thermal group at University of South Carolina I worked with. I would like to express my sincere appreciation to Dr. Wei Chang, Kai Luo, Dr. Andrew Wunderlich, Dr. Hessam Abdollahi, Dr. Silvia Arrua, Dr. Soheila Eskandari, Byunhee Moon, Dr. Kang Peng, Dr. Jonathan Siegers, Dr. Ozan Gulbudak.

I gratefully acknowledge the support of Office of Naval Research by grants N000141612956 and N000142112124. This work was approved for public release-Distribution Statement DCN# 43-10636-22.

Thanks Dr. Daniel Martin from Wolfspeed and Mr. Bill Bradley from the Machine Shop at the University of South Carolina for their great support in this work.

Finally, I would like to thank my wife, my son and my parents for their endless support and love.

ABSTRACT

There is a widespread need for high performance wide bandgap power modules in both commercial and military applications. However, given the rapid advancements of wide bandgap power module technology, conventional cooling solutions have not kept up and do not provide the thermal management performance needed for high power density. Based on the two-phase cooling approach, two-phase microchannels operating at low fluid flow rates with low pressure drops have huge potential in enabling higher power density applications. Several studies have illustrated the potential great advantages of two-phase cooling compared to single-phase cooling in terms of maximum device temperature, spatial thermal distribution and required pumping power, but no experimental validation for a power module application has been presented.

In this study, the objective is to achieve a power module with high thermal performance with two-phase mini-channel cooling. Well known challenges are local dryouts, non-uniform temperature distribution, larger channel length causing two-phase flow instability, controlling flow rate to acquire the optimized flow boiling performance. To overcome the challenges above, the study concentrates on the design and optimization of two-phase mini-channel cooling on power module:

a) Simulation-based evaluation of performance of two-phase cooling applied to power module. This approach provides an approximate method to quantify the achievable thermal performance of two-phase cooling, which serves as a guide to subsequent experiments. Based on the simulation results and analysis, the advantages of two-phase cooling are

summarized as: thermal power is increased by a factor of 3 for the same junction temperature rise; reduce difference between junction and case temperature ΔT_{jc} increasing the number of allowable thermal cycles by more than 400X; reduction of spacing among SiC chips by a factor of 3 can lead to a 9X reduction of parasitic switching loop inductance; the 10,000 X reduction in cooling flow rate brings a huge reduction in sizes of the pump, heat exchangers and coolant piping.

b) Initial design of mini-channel coldplate. The initial design of mini-channel coldplate for power module is completed and the coldplate is fabricated to prove the feasibility of the approach. Hydrofluoroether (HFE), which has a low boiling point, is used as a dielectric coolant in test to demonstrate the advantages of two-phase cooling vs single-phase cooling. Experimental results show that up to 81% improvement in junction temperature rise and 2.41 times reduction of thermal resistance of coldplate are achieved in two-phase cooling.

c) Design improvements: slot structure, porous structure, and micro-gap. To solve these problems, the two-phase mini-channel coldplate is optimized by three solutions. The slot structure introduces a lateral flow path to avoid the formation of large vapor slugs, the maximum power dissipation increases ~115W achieved by experiment. The porous structure utilizes capillary force to hold more liquid on the surface to act as a reservoir. The porous structure has been experimentally demonstrated with a 300W increase of maximum power dissipation and a 37.5% reduction of the thermal resistance. Micro-gap structure allows rewetting flow and vapor expansion across the micro-gap, preventing slug formation. An optimized micro-gap 60 µm is achieved in the study, which makes a similar maximum power dissipation with porous structure.

d) Novel micro-gap structure. A novel micro-gap structure with reservoir channel is proposed to improve the overall thermal performance of two-phase mini-channel coldplate. The proposed micro-gap structure introduces reservoir channel allowing rewetting flow to avoid dryout. The novel design combined micro-gap and porous structure is demonstrated on a copper plate and reduced case temperature to 13 °C compared with conventional micro-gap mini-channel. An invention disclosure has been filed.

e) Integration of two-phase mini-channel structure on the module baseplate. A power module with integrated two-phase mini-channel on the baseplate is proposed, which has a significant reduction of thermal resistance by removal of baseplate and thermal interface material (TIM). Furthermore, to remove the baseplate with a function as a heat spreader, a higher HTC cooling is needed. Therefore, two-phase mini-channel is one of the best solutions in this case, which enhances the overall thermal performance of power module. The experimental results show that total thermal resistance from junction to coolant at inlet $R_{th(j-in)}$ of proposed module is reduced 36.7%, which approximately matches the value from theoretical calculation. Approximately 2X increase of maximum power dissipation is achieved at 25ml/min flow rate.

f) Study on the effect of channel height on two-phase cooling performance by experiment. The channel height impact on the flow boiling performance was experimentally investigated based on heat transfer measurement and visualization via a high-speed camera. The case/wall temperature of the mini-channels was chosen as the main restraint for the testing. The experiment results are compared with a modified flow boiling model. The results show that the maximum heat flux ~70W/cm^2 (heating power 1050W) is achieved in a designed channel height.

TABLE OF CONTENTS

LIST OF TABLES

LIST OF FIGURES

CHAPTER 1

INTRODUCTION

There is a widespread need for high performance wide bandgap power modules in both commercial and military applications. For example, the Department of Energy Electric Drive Technology Roadmap requires a 35% size reduction and a 40% weight reduction by 2022 [1]. The 2015 International Technology Roadmap for Semiconductors requires an increase of 59% in spatial power density of DC-DC converters by 2021 and of 85% by 2023 [2]. Advanced ships require high power density power electronic systems that can process required power while meeting stringent size and weight requirements. In particular, the All-Electric-Ship concept critically depends on the availability of switching converters with power densities vastly exceeding the current state-of-the-art. All power used for propulsion, for all loads, and for weapons aboard the Electric Ship is processed by one or more switching converter power stages. Given the resulting high penetration of switching converters, their size and weight become critical. This has led to a great interest by the Navy in wide bandgap power semiconductor devices because they are expected to lead to at least a doubling of power density according to the 2015 Naval Power and Energy Systems Technology Development Roadmap [3].

Power modules are complex electro-thermo-mechanical devices that have competing thermal and electrical requirements [4]. From an electrical standpoint, they must provide optimized interconnections of the power semiconductor devices. Achieving low parasitic switching loop inductances is critical for reduced switching losses, for reduced voltage stress on semiconductor devices and for reduced electromagnetic interference (EMI). From a thermal standpoint, power modules must provide an effective high heat flux path to remove the heat generated at the semiconductor junction due to switching and conduction losses. From a mechanical standpoint, they must provide mechanical support and protection to the power semiconductor devices. High power cycling and thermal cycling capability is critical for module reliability. These requirements are contradictory in nature: to reduce parasitic inductances, power devices should be placed as close as possible to each other, but this causes increased temperatures and makes it extremely challenging to effectively remove the generated waste heat. Power modules are designed to provide an optimized trade-off among these conflicting requirements, and improved cooling performance is a key enabler for the miniaturization and performance optimization of power modules.

Conventional power module cooling solutions are widely available commercially. For high heat flux and high heat dissipation requirements liquid cooling is used. The module is bolted onto a water-cooled cold plate with a thermal grease interface to reduce the contact thermal resistance between module baseplate and cold plate. Recently, to improve thermal performance, a baseplate with integrated pin fin structure has been proposed by various manufacturers for electric vehicle and hybrid electric vehicle applications. Fuji Electric reports a 30% reduction in thermal resistance and a 40% reduction in size compared to the conventional solution [5]. Mitsubishi Electric proposes a similar solution for its 7th generation IGBT module and obtains similar performance improvements [6]. The approach has also been used for SiC modules [7, 8]. However, given the rapid advancements of wide bandgap power module technology, conventional cooling solutions have not kept up and do not provide the thermal management performance needed for high power density.

1.1 Thermal management of power module

Modern power module structure is based on direct bonded copper (DBC), as shown in Figure1.1. From top to bottom, multiple layers are attached together, including chip, solder, DBC (copper/ceramic/copper), solder, baseplate (heat spreader), thermal interface material (TIM, such as thermal grease), and coldplate (air or liquid cooling). The heat is generated by chip on the top and propagated through each layer. The vertical propagation of heat is dominant, because the thickness is much smaller than length and width of power module. Generally, the heat spreading angle is considered as 45˚ to calculate the effective heat propagation area. There are temperature differences between top and bottom of each layer due to thermal resistance, and the relationship between temperature difference, thermal resistance and power dissipation is given in (1.1).

$$\mathit{\Delta} T = P_{diss} \times R_{th} \tag{1.1}$$

Where ΔT is temperature difference between top and bottom of each layer, P_{diss} is power dissipation, R_{th} is the total thermal resistance of each layer on the heat propagation path.

Junction Temperature (T_j), that is the temperature of chip, is an important parameter in thermal management of power module because the module has a maximum allowable junction temperature and will fail if this temperature is exceeded.

The maximum operating power of the power module is limited by the maximum value of T_j, which is 175 ˚C for current Si- and SiC-based power modules. According to (1.1), thermal resistance is a key factor to manage T_j. An equivalent Cauer RC network is used for power module thermal resistance analysis as shown in Figure 1.2. The thermal resistance, R_i, of the i^{th} layer, due to the conductive heat transfer is calculated by (1.2):

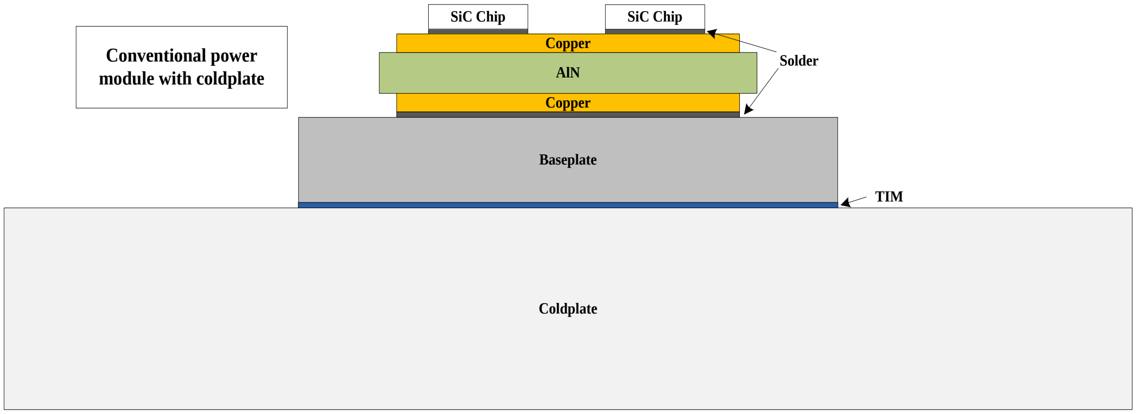

Figure 1. 1 Schematic of conventional power module structure

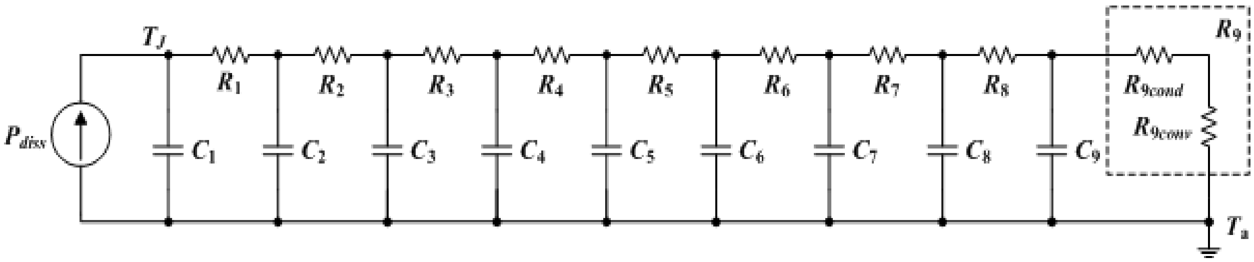

Figure 1. 2 Equivalent Cauer RC thermal network

$$R_i = \frac{d_i}{k_i A_i} \tag{1.2}$$

where d_i is the thickness, A_i is the effective cross-section area, considering a spreading angle for conductors, and k_i is the thermal conductivity of the i^{th} layer. The resistance of the coldplate consists of two series resistances R_{cond} and R_{conv} due to the conductive and convective heat transfer, respectively. The latter is inversely proportional to the convection heat transfer coefficient (HTC) of the sink, h, and surface area exposed to the fluid, A, as shown in (1.3).

$$R_{conv} = \frac{1}{hA} \tag{1.3}$$

Therefore, to reduce the thermal resistance of each layer, smaller thickness, larger effective area, and higher thermal conductivity are preferred. Additionally, a better coldplate with high HTC is required.

Besides maximum chip temperature, the temperature difference ΔT_{jc} between junction and case temperature are also important for reliability of power module. Smaller ΔT_{jc} allows power modules to sustain a larger number of thermal cycles. Above all, lower maximum chip temperature and higher case temperature are desirable in application to reduce chip thermal stress and improve heat transfer.

1.2 Background of single/two-phase microchannel cooling

The physical dimensions of the micro/mini-channels are characterized by the hydraulic diameter defined as (1.4).

$$D_h = \frac{4\,A}{P} \tag{1.4}$$

where D_h is the hydraulic diameter, A is the area of the cross-section, and P is the perimeter of the cross-section. The hydraulic diameter generalizes the concept of diameter to non-round channels. Generally, channels having a hydraulic diameter of 10–200 μm are called microchannels, whereas channels having a hydraulic diameter of 200 μm to 3 mm are called mini-channel.

Single-phase microchannels have been proposed for improved thermal performance more than three decades ago [9]. Microchannels have a much higher heat transfer surface area to fluid volume ratio, which allows convection to be enhanced compared to macro-scale systems. As the hydraulic diameter decreases in microchannels, the heat transfer coefficient increases, providing an excellent cooling mechanism. Based on the heat transfer theory, in the single-phase regime, the relationship between the convective heat transfer coefficient (HTC) h_c and hydraulic diameter D_h is clearly shown in equation (1.5).

$$h_c = N_u \frac{K_f}{D_h} \tag{1.5}$$

Where Nu is Nusselt number, which is a constant related with cross-section and boundary conditions of channels, K_f is thermal conductivity of fluid and D_h is hydraulic diameter. As the hydraulic diameter decreases in microchannels, the heat transfer coefficient increases significantly, providing an excellent cooling mechanism. In theory, it is up to a ~ 1000 times increase of h_c compared between conventional coldplate (dozens of millimeters level of D_h) and microchannel (dozens of micrometers level of D_h). For mini-channel, the increase of h_c is ~ 10 – 100 times. However, single-phase microchannel cooling has been achieved at cost of prohibitive pumping power and high temperature difference between inlet and outlet.

Phase change of a fluid can cause a substantial amount of heat to be absorbed (latent heat of evaporation). When a liquid turns into a gas or a gas into a liquid, the temperature reaches a constant temperature until the percentage composition of the fluid is either solely liquid or solely vapor. The evaporation of fluid results in the absorption of heat during the phase change between liquid and vapor. This is the fundamental of two-phase cooling. The heat flux in single-phase and two-phase microchannel cooling is defined in equation (1.6) and (1.7) respectively.

$$Q = \dot{m} C_p (T_c - T_{in}) \tag{1.6}$$

$$Q = \dot{m} h_{fg} \tag{1.7}$$

Where Q is heat flux, $\dot{m}$ is mass flow rate, C_p is specific heat, T_c is coldplate temperature at heating side, T_{in} is coolant temperature at inlet of coldplate, and h_{fg} is latent heat. Using water as an example, the latent heat of water is ~500 times larger than specific heat, therefore, the heat flux of two-phase cooling, corresponding to the power dissipation of power modules, is ~10 times larger than that of single-phase when the temperature difference $(T_c - T_{in})$ is up to 50˚C. Beside the superior thermal performance, two-phase microchannels improve spatial temperature uniformity and reduce flow rate, and, hence, reduce pumping power and the size and weight of entire cooling system.

The mechanism of two-phase cooling is complicated, strongly depending on the channel shape, dimension, surface roughness, heating method, coolant properties, etc. Recent studies of two-phase microchannels (TPM) operating at low fluid flow rates with low pressure drops have shown huge potential in enabling higher power density applications [10-14]. Flow boiling in miniaturized channels has been studied in the last decade as a promising solution to enhance heat transfer and reduce coolant flow rate, resulting in reduced pumping power, by taking advantage of the latent heat of evaporation [15-18].

Tremendous progress has been made in understanding transport mechanisms in heat transfer [19-21], two-phase flow instabilities [22-25], and critical heat flux (CHF) [26-30]. Various techniques such as artificial cavities [31, 32], microcoatings [33], nanocoatings [34, 35], restrictors [25], pin fins [36], and microjets [37] have been developed to enhance flow boiling in microchannels in terms of HTC, pressure drop (Δp), two-phase flow stability and CHF. Regarding two-phase cooling applied to power modules, a few parametric and simulation studies have been recently reported [38-40]. These studies clearly illustrate the potential great advantages of two-phase cooling compared to single-phase cooling in terms of maximum device temperature, spatial thermal distribution and required pumping power, but no experimental validation for a power module application has been presented.

1.3 Contributions in this study

In the study of two-phase microchannel heat transfer, the critical physical parameter of the microchannel is its maximum length – which limits the maximum heat transfer area – and the physical dimensions of the microchannels (or mini-channels) used. Theoretical studies have demonstrated the superior performance of two-phase cooling [41,42] for microchannels with a typical channel length of 10 mm [14, 41]. These dimensions are quite small compared to what is needed for power module applications.

Considering the dimensions of a typical high power module, the length of Wolfspeed^{TM} SiC power module package is up to 80 mm long [43]. Note that this power module is one of the smallest for this power rating, compared with 106mm length of conventional IGBT [44] and 128mm length of press-pack IGBT [45]. The channel length required for this kind of package is at least 40 - 60mm in order to cover the effective heating area, which is 4 - 6 times larger than that of two-phase microchannels in the literature. Two-phase micro/mini-channel cooling is unproven for these large heating areas. This scaling problem is the major challenge for the successful application of two-phase cooling to power modules. This is the challenge of the proposed study: demonstrating feasibility of two-phase cooling for the scaled-up case of power modules.

Additionally, it would be highly desirable to use mini-channels rather than microchannels. The reasons why the larger hydraulic diameter is desirable are ease of manufacturability and mitigation of the fouling problem – the accumulation of dirt in the channel clogging it and reducing the heat transfer effectiveness. Therefore, increasing the hydraulic diameter to mini-channel level is a good option.

In conclusion, the present study aims to demonstrate two-phase mini-channel cooling overcoming the challenges of scaling up to a much larger heating area and increasing the hydraulic diameter of the channel. Well known challenges are local dryouts, non-uniform temperature distribution, larger channel length causing two-phase flow instability, controlling flow rate to acquire the optimized vapor quality – that is the mass fraction of vapor in a saturated mixture of liquid and vapor.

In this study, the objective is to achieve a power module with high thermal performance with two-phase mini-channel cooling. To overcome the challenges above, the study concentrates on the design and optimization of two-phase mini-channel cooling on power module, and the contributions are:

a) **Simulation-based evaluation of performance of two-phase cooling applied to power module.** This approach provides an approximate method to quantify the achievable thermal performance of two-phase cooling, which serves as a guide to subsequent experiments.

b) **Initial design of mini-channel coldplate.** The initial design of mini-channel coldplate for power module is completed and the coldplate is fabricated to prove the feasibility of the approach. Hydrofluoroether (HFE), which has a low boiling point, is used as a dielectric coolant in test to demonstrate the advantages of two-phase cooling vs single-phase cooling. The test results show that up to 81% improvement in junction temperature rise and 2.41 times reduction of thermal resistance of coldplate are achieved. However, under some conditions performance is limited by local dryout, non-uniform temperature distribution and flow instability, well-known problems of the two-phase cooling approach.

c) **Design improvements: slot structure, porous structure, and micro-gap structure.** To solve these problems, the two-phase mini-channel coldplate is optimized by three solutions, slot structure, porous structure and micro-gap structure. The slot structure introduces a lateral flow path to avoid the formation of large vapor slugs. The porous structure utilizes capillary force to hold more liquid on the surface to act as a reservoir. Micro-gap structure allows rewetting flow and vapor expansion across the micro-gap, preventing slug formation. Experimental validation shows that the improvements enhance the flow boiling performance reducing the thermal issues mentioned above.

d) **Novel micro-gap structure.** A novel micro-gap structure with reservoir channel is proposed to improve the overall thermal performance of two-phase mini-channel coldplate. The proposed micro-gap structure introduces reservoir channel allowing rewetting flow to avoid dryout. The novel design combined micro-gap and porous structure is demonstrated on a copper plate and reduced case temperature significantly compared with conventional micro-gap mini-channel. An invention disclosure has been filed.

e) **Integration of two-phase mini-channel structure on the module baseplate.** A power module with integrated two-phase mini-channel on the baseplate is proposed. According to the analysis of thermal resistance composition in commercial power module, the total thermal resistance is reduced significantly by removing baseplate and thermal interface material (TIM). Based on theoretical calculations, a 38.1% reduction of total thermal resistance is achieved compared to the power module with conventional cooling. Furthermore, to remove the baseplate with a function as a heat spreader, a higher HTC cooling is needed. Therefore, two-phase mini-channel is one of the best solutions in this case, which enhances the overall thermal performance of power module.

f) **Study on the effect of channel height on two-phase cooling performance by experiment.** The channel height impact on the flow boiling performance was experimentally investigated based on heat transfer measurement and visualization via a high-speed camera. The case/wall temperature of the mini-channels was chosen as the main restraint for the testing. The experiment results are compared with a modified flow boiling model. The objective of this study is to better understand the impact of a key design parameter on the flow boiling in mini-channels for SiC power module cooling applications.

CHAPTER 2

EVALUATION OF PERFORMANCE OF POWER MODULE WITH TWO-PHASE COOLING BY SIMULAITON

2.1 Thermal performance analysis using Ansys

In this section, the performance of a power module with two-phase cooling (named "novel power module") is simulated. The novel and conventional power modules are modelled using Ansys thermal simulation software with the parameters specified in Table 2.1. The HTC value used for two-phase cooling in the novel power module has been experimentally demonstrated at component level [11-14]. Figure 2.1 shows the steady-state temperature distribution enabled by the novel and conventional power modules with the same number of chips (4 chips), for the same power dissipation level (50W per chip, 200W total) and for the same module footprint. The difference in maximum chip temperature

Table 2.1 Thermal Simulation Parameters

Module dimensions	80 x 59 mm
Chip dimensions	6 x 3 mm
X-axis distance between chips	13 mm
Y-axis distance between chips	36 mm
Inlet coolant temperature novel module	100 ℃
Inlet coolant temperature conventional module	90 ℃
Heat transfer coefficient novel module	50 kW/(m^2K)

between the novel power module (136℃) and the conventional power module (156℃) is 20℃, which is a 36% reduction in chip temperature rise. Moreover, the simulation shows that in the conventional power module the temperature of a chip is affected by the adjacent chip (notice the elevated temperature between the two upper or lower chips), whereas in the novel power module there is basically no interaction. This shows that in the novel structure it would be possible to place the chips closer together without a strong negative effect on temperature.

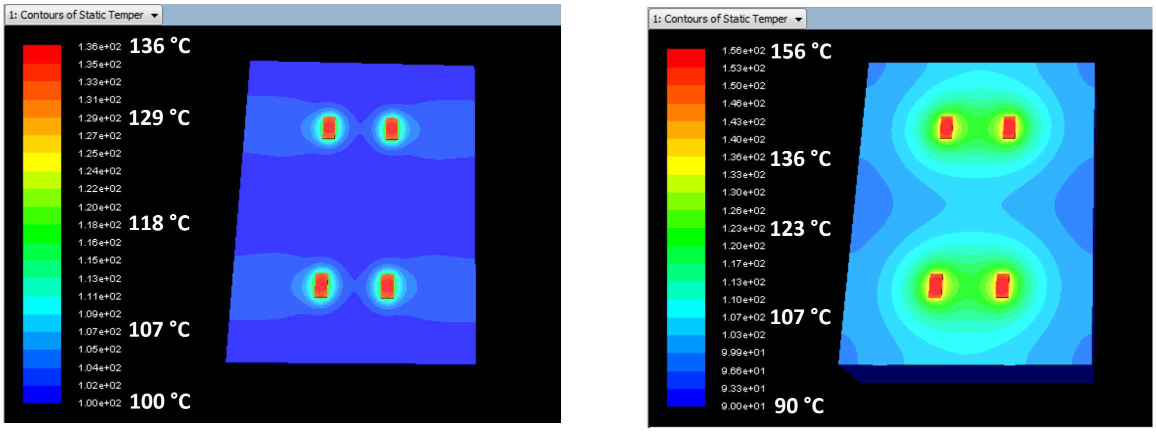

(a) (b)

Figure 2. 1 Thermal simulation for novel (a) and conventional (b) power module with 50W/chip (200W total)

Therefore, in Figure 2.2 for the novel power module with two-phase cooling the number of chips is doubled (8 chips) and the power per chip is increased to 80W for a total power dissipation of 640W, more than three times larger than in Figure 2.1. In this case the maximum chip temperature is 159℃, approximately equal to the maximum chip temperature for the conventional power module dissipating 200W shown in Figure 2.1 (b). This 3X increase in power dissipation capability is due to the increased heat flux with two-phase microchannel cooling and the elimination of an interface layer. The removed layer is the TIM layer shown in Figure 1.1, which is usually placed between baseplate and heat sink to improve the thermal contact. Thermal resistance of TIM layer constitutes a large contribution to the total thermal resistance of power module.

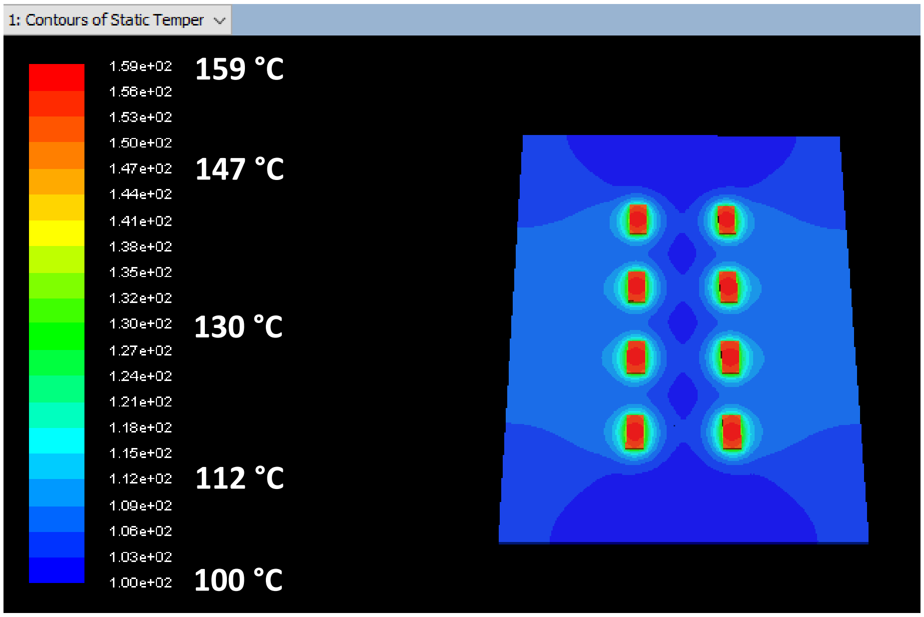

Figure 2. 2 Thermal simulation for novel power module with 80W/chip (640W total)

2.2 Estimated Reduction of Size & Weight

The novel power module with two-phase mini-channel cooling of Figure 2.3 has reduced size and 3X weight reduction owing to higher power density. A case study is now presented with performance comparison to a conventional power module.

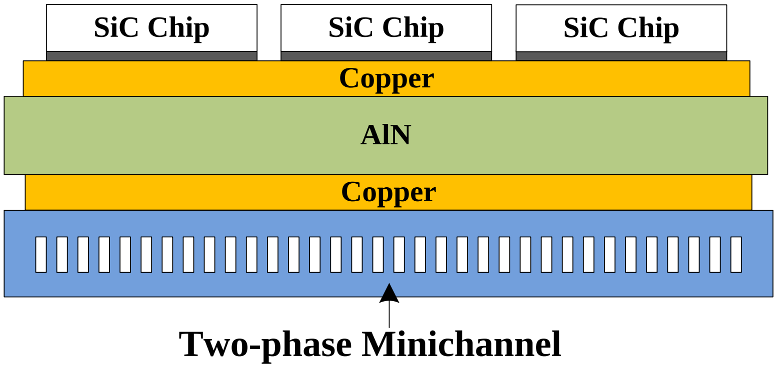

Figure 2.3 Power module with two-phase mini-channel cooling

Wolfspeed^{TM} has a SiC MOSFET half bridge module CAS120M12BM2 [46]. with 4 chips having a total weight of 290g. The weight of the baseplate is 174g, approximately 60% of total weight. Assuming a 3-phase converter realized using these modules, the total weight for 3 modules and one coldplate (HI-CONTACT^{TM} liquid cold plate 416501U00000G by AAVID THERMALLOY, weight 1020g) is 3 x 290 + 1020 = 1890g. Since, as shown in Figure 2.2, the novel module has 3X dissipation power capability, we can replace the three modules with a single novel power module, which has a weight of 290 x (1-0.6) + 460 = 576g due to the removal of the baseplate and addition of the lightweight (460g) two-phase microchannel structure of Figure 2.3. This is a 3X reduction in weight.

The system-level reduction in size and weight is much larger due to the extremely small flow rate required for two-phase heat transfer. According to [47], only 11.2µL/s flow rate is needed to handle heat flux of 184W/cm^2 over an area of 0.2cm^2, whereas 8L/min = 133,333µL/s is needed in conventional coldplate, which is 10 thousand times larger.

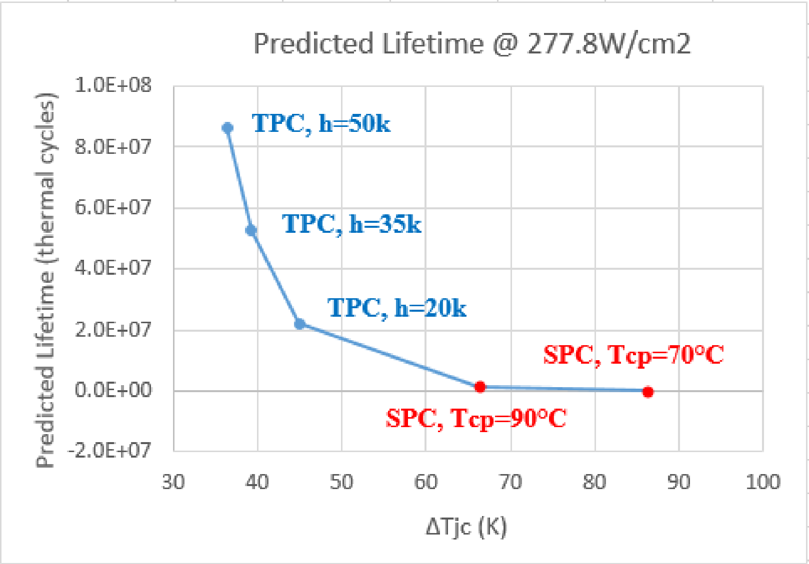

Figure 2.4 Lifetime as a function of ΔT_{jc} following [48]

Therefore, the auxiliary cooling equipment in the cooling system, such as pump, coolant pipes, heat exchanger, etc. will have much smaller size and weight with use of two-phase cooling.

2.3 Improved lifetime of novel power module

As described above, the temperature difference ΔT_{jc} between junction and case is also important for reliability of power module. Smaller ΔT_{jc} is helpful for power modules to sustain a larger number of thermal cycles. The case temperature of the coldplate for conventional power module is usually set as 70 - 90 ℃, whereas for the novel power module it is 100 ℃ due to phase change using water as coolant. Following [48], the lifetime of power module for different cooling conditions, given by the number of thermal cycles before failure, can be predicted as a function of ΔT_{jc} as shown in Figure 2.4. The figure clearly shows that the lifetime of power module increases significantly with improved two-phase cooling (TPC) compared to conventional single-phase cooling (SPC) and the best lifetime of power module with TPC is 400 times larger than with SPC coldplate at 70 ℃ and 60 times larger than with SPC coldplate at 90 ℃.

2.4 Electrical Performance Improvement due to Reduced Parasitics

Along with the reduction of module size using two-phase cooling, the effective switching loop inductance is reduced as pictorially shown in **Error! Reference source not found.**2.5. Reduced parasitic inductance improves the inductive switching performance of the module. The effect of switching loop inductance on switching losses can be quantified using the analytical switching loss model presented in [49]. The parasitic switching loop inductance stores energy during conduction, which is dissipated at turn-off. Additionally, the parasitic inductance in combination with the semiconductor device capacitances causes overshoot and ringing in the voltage and current waveforms during the switching transitions. The overshoot and ringing are a major cause of increased device stress and increased EMI. These effects, which are especially severe for wide bandgap semiconductor devices due to their higher switching speed, have forced switching converters designers to slow down switching transitions, causing additional losses and negating the speed advantages of these new devices. A reduction by a factor of 3 in the distance between chips can lead to a reduction by a factor of 9 in switching loop area, which gives a 9X reduction in the switching loop inductance contribution due to the module layout. The actual total loop inductance reduction will be somewhat smaller due to the fact that the overall loop inductance includes the connections to the decoupling capacitors [50] but has the potential to significantly improve the power module switching performance.

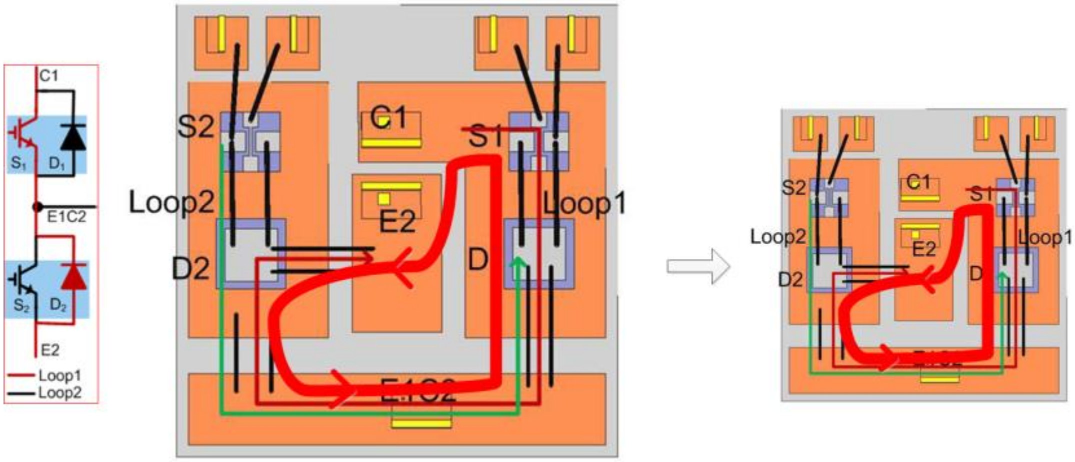

Figure 2.5 Reduced switching loop inductance

To quantify the reduction of parasitics, Ansys Q3D simulation is used to extract parasitic inductances in power module. In Figure 2.6 a structure based on the dimensions of Wolfspeed™ SiC MOSFET module CAB450M12XM3 is constructed. The module is a half bridge design, 5 chips in parallel for both the high-side and low-side. There are 3 terminals for electrical connections, from left to right, Drain 1(D1), Source 2 (S2), and Drain 2/Source 1(D2/S1). The size and position of chips in simulation are the same as in the product. The thickness and number of bonding wire strands and the area of the terminals are the same as in the product, and the shape of bonding wire is simplified as a straight line, which has negligible effect on inductance calculation. The simulated parasitic inductance Lp from D1 to S2 is 6.71nH, which matches the value of 6.7nH from datasheet quite well.

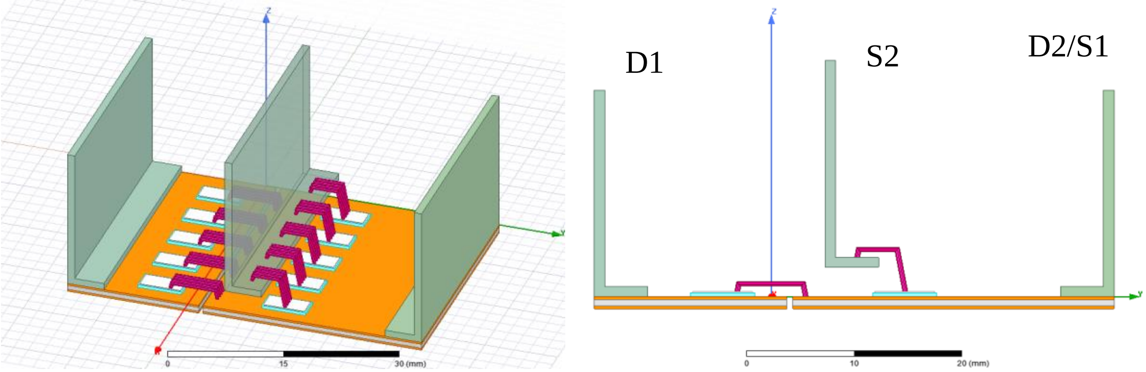

(a) (b)

Figure 2.6 Q3D simulation of Wolfspeed^{TM} SiC power module (a) top view, (b) side view.

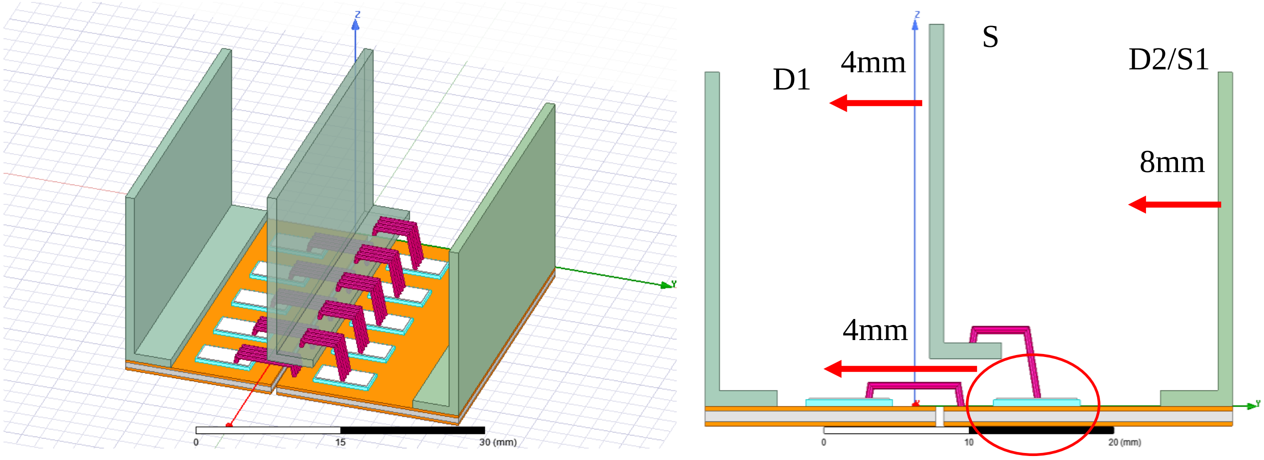

Figure 2.7 Shrunk-down power module

Table 2.2 Simulated parasitic inductance: Regular vs Shunk-down module

	Module active area (mm^2)	Parasitic inductance (nF)
Regular module	56 x 32 = 1792	6.71
Shunk-down module	44 x 32 = 1408	4.51
Reduced percentage	21.4%	32.8%

As discussed above, the parasitic inductance is reduced when power module size is shrunk-down. In Figure 2.7, the power module is shrunk-down by moving S2 and chips on the right 4mm and D2/S1 8mm to the left, which makes both groups of chips stay closer. The simulated results are summarized in Table 2.2. The total active area of power module is reduced by $12 \times 32 = 384$ mm^2, which is 21.4% of total area. The parasitic inductance Lp is 4.51 nH, which represents a 32.8% reduction of total inductance.

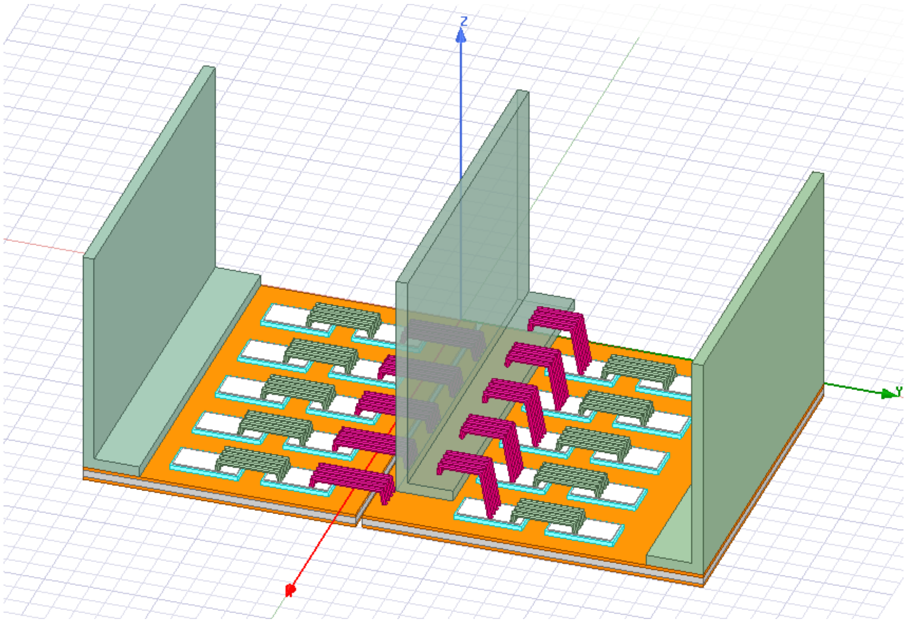

Figure 2.8 Double chips at the same area

Moreover, two-phase cooling allows increasing power density, not only by shrinking down the module, but also by making it possible to add more chips for the same area. In Figure 2.8, the number of chips on both sides is doubled in parallel and the total area is the same as for the regular module, which means that the current rating is doubled. The price to pay is that the value of parasitic inductance increases to 9.31 nH, which is a 39% increase.

2.5 Summary of two-phase cooling

Based on the simulation results and analysis, the advantages of two-phase cooling are summarized as below.

- **Increased module power density** – the baseplate and coldplate will be eliminated and the thermal power is increased by a factor of 3 for the same junction temperature rise, leading to a 3X reduction in weight in an example system compared to commercial products.
- **Increased lifetime** – two-phase cooling can reduce difference between junction and case temperature ΔT_{jc} during thermal cycling and achieve more uniform thermal distribution, increasing the number of allowable thermal cycles by more than 400X.
- **Improved electrical performance** – reduction of spacing among SiC chips by a factor of 3 can lead to a 9X reduction of parasitic switching loop inductance contributed by the module. This can lead to significantly reduced overshoot and ringing during switching, reduced electromagnetic interference (EMI) and lower switching losses.
- **Reduced required cooling fluid flow rate** – the required two-phase cooling flow rate (~11.2µL/s flow rate) is reduced by 4 orders of magnitude compared to a conventional cold plate, requiring 8L/min (133,333µL/s) in handling a heat flux of 184W/cm^2 over an area of 0.2cm^2, as reported in [47].
- **Reduced system size and weight** – the 10,000 X reduction in cooling flow rate brings a huge reduction in sizes of the pump, heat exchangers and coolant piping.

CHAPTER 3

DESIGN AND FABRICATION OF TWO-PHASE MINI-CHANNEL COLDPLATE FOR SIC POWER MODULE

Compared with conventional fundamental studies of two-phase microchannels used for cooling, the dimensions of a power semiconductor power module are large. A larger hydraulic diameter (more than 1mm) is needed to satisfy the demand of cooling for high power module. Therefore, the mini-channel is chosen in this work. In this chapter, the design and fabrication of two-phase mini-channel coldplate (TPMC) for SiC power module is presented. Different designs and optimizations are proposed to improve thermal performance of TPMC. The work focuses on the experimental demonstration of two-phase cooling and comparison between two- and single-phase cooling with mini-channel. The experimental setup is introduced in Section 3.1, preliminary test results are presented in Section 3.2 and the optimization of the two-phase mini-channel structure is presented in Section 3.3.

3.1 Design of Experimental Setup

3.1.1 Power module under test

The experimental validation uses Wolfspeed^{TM} SiC MOSFET module CAB450M12XM3 shown in Figure 3.1. The module is a half bridge design, 5 chips in parallel for both the high-side and low-side. It has half the weight and volume of a standard 62 mm module [51], such as Infineon IGBT module FF450R12KT4P. There is an integrated NTC (Negative temperature coefficient) thermistor on the right-downside corner, which will be used to estimate the average junction temperature in the module during test. The module is a typical representative of current trend of power module design for high power and high switching frequency applications: small size and weight, low parasitic inductance, high power density and high temperature capability (175 °C continuous junction operation). Since module operation is thermally limited, improved thermal management of the module can significantly improve its overall performance.

(a) External view (b) Internal view

Figure 3.1 Wolfspeed^{TM} SiC MOSFET module.

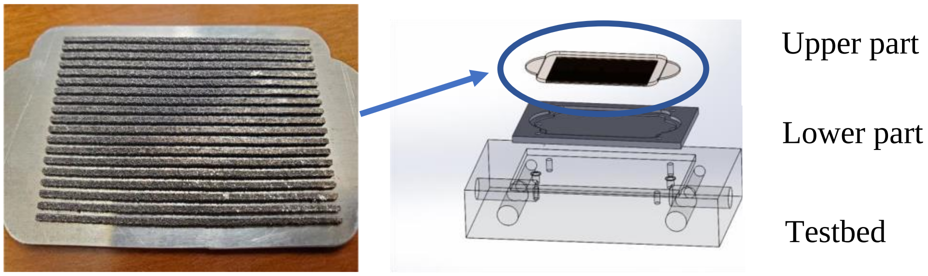

(a) Upper part of mini-channel structure (b) Coldplate with testbed

Figure 3.2 Mini-channel cooling coldplate with testbed

3.1.2 Mini-channel coldplate and testbed

Based on the module dimensions, the mini-channel coldplate is designed with the same area as the module baseplate, as shown in Figure 3.2. The coldplate is made of aluminum and the upper and lower parts are sealed together after channels are fabricated as shown in Figure 3.2 (b). The upper part of the mini-channel structure shown in Figure 3.2 (a) is fabricated by 3-D printing. More details of design and fabrication will be discussed in the following sections. The channels have length × width × depth equal to 59.75mm × 1mm × 1mm. The power module is mounted on top of the upper part of the mini-channel structure. The inlet and outlet are located in the lower part to connect the coolant lines. A testbed support structure in Figure 3.2 (b) is added for ease of mounting sensors. The punched holes on side walls of testbed are used to connect coolant loop and install thermocouples and pressure transducers for monitoring temperature and pressure drop of coolant between inlet and outlet. The mini-channel coldplate is embedded on the top side of testbed, then power module and coldplate are bolted together with a thin coating of thermal paste MX-4.

3.1.3 Control and protection circuit

The control circuit is designed to provide a precisely controllable amount of power dissipation on the SiC MOSFET devices by operating them in the dissipative saturation region. The power supply operates in constant current mode and the drain-source voltage drop is controlled to provide the desired power dissipation. The control circuit, based on a diode multiplier approach, adjusts power dissipation independently on low-side and high-side of module, as shown in the green circle portion of Figure 3.3. In the circuit, the relationship between gate-source voltage V_{gs1} and drain-source voltage V_{ds1} is given by (3.1).

$$V_{ds1} = V_{gs1}\,(R_1 + R_2)/R_2 \tag{3.1}$$

Assuming R_2 is constant, R_1 can be varied to adjust the value of Vds1. The same approach is used for V_{gs2} and V_{ds2} as well. Potentiometers R_1 and R_{11} can be used to impose equal power dissipation on low side and high side MOSFETs.

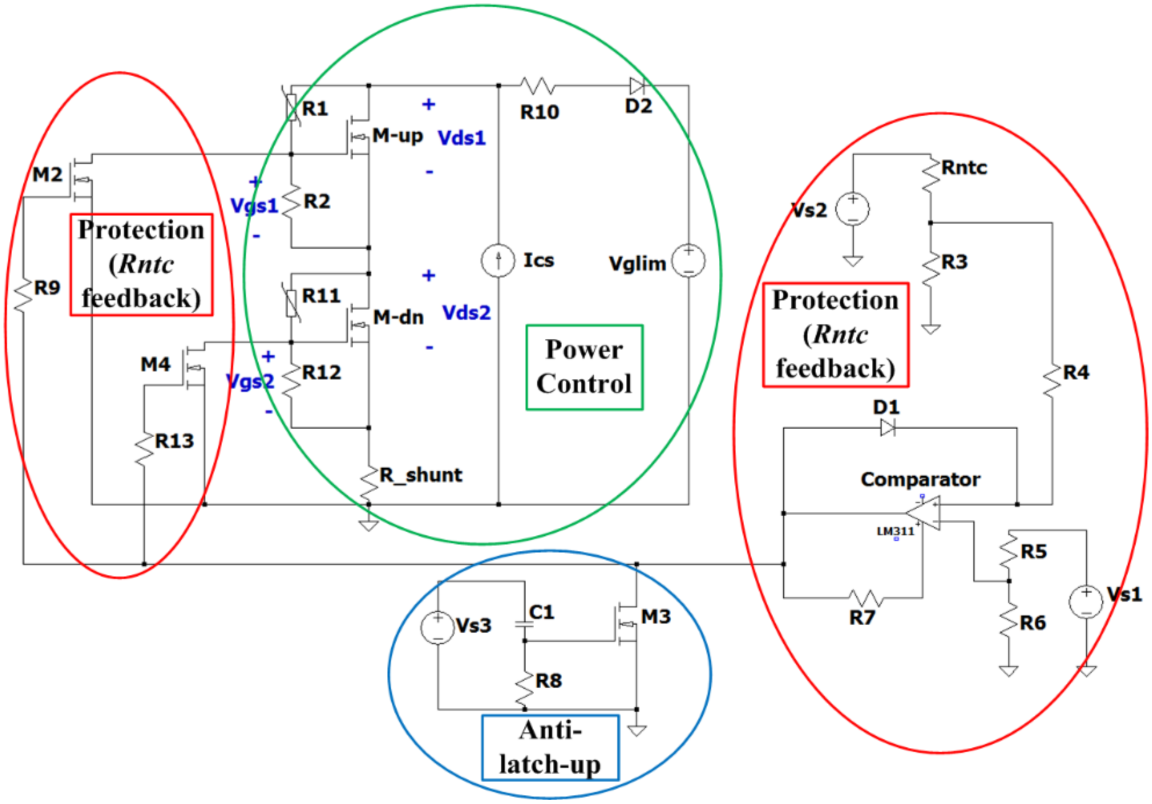

Figure 3.3 Control and protection circuit

The protection circuit, shown in the red circle portions of Figure 3.3, provides overtemperature protection by monitoring the value of NTC thermistor R_{ntc} integrated in the power module. A latching comparator triggers when the NTC temperature exceeds a threshold set by resistors R_5 and R_6. Diode D_1 provides the latching functionality in case of overtemperature. The high voltage of the comparator output turns on MOSFETs M_2 and

M_4, turning off the power module SiC MOSFETs. The blue circle portion of Figure 3.3 prevents latch-up of the comparator at turn-on.

3.1.4 Experimental setup

The experimental setup diagram in Figure 3.4 shows the coolant, electric power and data acquisition systems. The coolant loop includes a N_2 coolant tank, an input-side coolant reservoir, a digital flow meter to monitor coolant flow rate, a coldplate attached to power module, and an output-side coolant reservoir. The electrical system includes the power supply operating as a current source, the control and protection circuit described above, and the power module. A resistive current shunt is used in the control circuit to measure the value of SiC MOSFET current – see Shunt Resistor $R_{\_shunt}$ in the green circle portion of Figure 3.3. The Data Acquisition System acquires all variables of interest. The Agilent 34972A data acquisition system is used to measure inlet and outlet temperatures of coldplate, module case temperatures measured by three thermocouples mounted underneath the chips on each side and in the middle (red dots in Figure 3.4), junction temperature measured by the built-in NTC thermistor of the power module, SiC MOSFET voltages and currents used to calculate power dissipation separately on high and low sides, and coolant pressure of inlet and outlet of coldplate to calculate pressure drop.

There are a few reasons to monitor case temperatures. Firstly, case temperature is needed to estimate junction temperature using (3.2).

$$T_J = T_C + P_{diss} \cdot Z_{th(JC)} \tag{3.2}$$

where T_j is junction temperature of chip, T_c is case temperature, P_{diss} is the power dissipated in the power module – obtained by multiplying drain-source voltage V_{ds} by conduction current I_d and $Z_{th\,(jc)}$ is the junction-to-case thermal impedance. In the steady

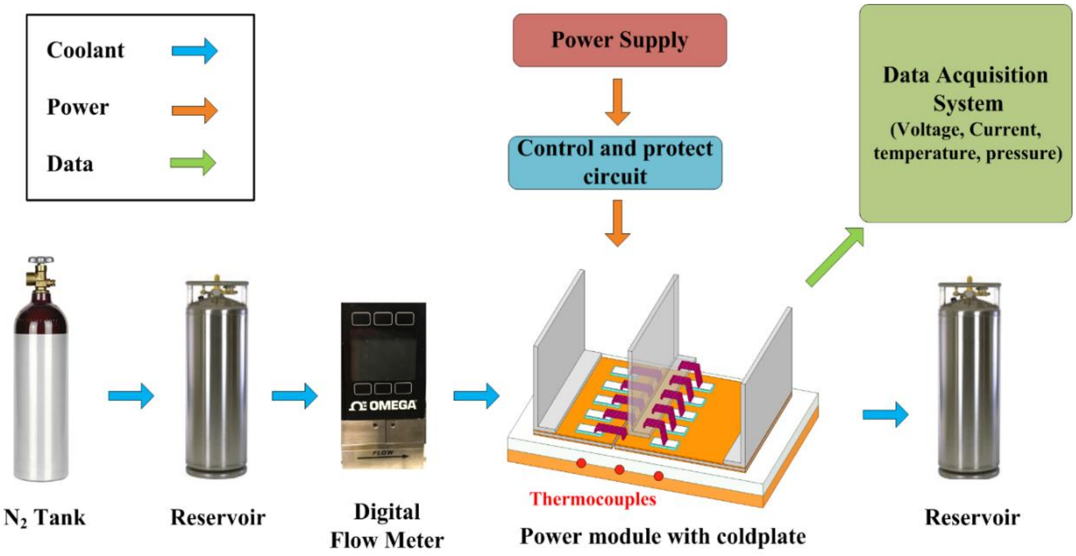

Figure 3.4 Experimental setup of two-phase cooling

state, thermal resistance $R_{th\ (jc)}$ is considered as given in the datasheet. The value of T_j estimated by T_c is more accurate than just assuming T_j to be equal to the temperature of the NTC thermistor. It is helpful to monitor junction temperature accurately during test. Furthermore, T_j estimated by T_c is used to calibrate the overtemperature protection threshold based on the NTC thermistor temperature in the protection circuit. Secondly, case temperatures are used to observe the uniformity of thermal distribution, which plays a critical role in the reliability of the power module, as described above. An uneven thermal distribution means different ΔT_j on each chip during a power cycle. As a result, the module can fail earlier than expected due to overheating on any of the chips. Thirdly, monitoring case temperature provides a way to establish whether the coolant stays in the single-phase cooling regime or enters two-phase cooling regime.

3.1.5 Coolant used in test

Novec™ 7100 is a proprietary hydrofluoroether (HFE) from 3M, whose properties are shown in Table 3.1 compared to water. Its boiling point is 61 °C and it is good as a heat

Table 3.1 Properties of HFE-7100 vs. Water

Propeties	HFE-7100	Water
Latent heat of vaporization (kJ/kg)	111.6	2264.76
Specific heat, 25 °C, 1 ATM (J/kg·K)	1183	4179
Liquid thermal conductivity (W/m·K)	0.069	0.6
Boiling point, 1 ATM(°C)	61	99.97
Liquid density, 25 °C (kg/m^2)	1520	1000
Kinematic viscosity (cSt)	0.37	1.0038
Surface tension, 25 °C (mN/m)	13.6	72
Vapor pressure, 25 °C (kPa)	26.9	3.17

transfer fluid due to its excellent environmental, health and safety profile. Specifically, HFE is a dielectric fluid with dielectric strength more than 10kV/mm [52]. This property makes it well-suited as a coolant for power electronics. HFE is preferred during initial design and test due to its low boiling point, which is convenient to observe the phase change between single- and two-phase. Water is a better option for high power operation because it has a higher latent heat of vaporization, specific heat and thermal conductivity.

3.2 Preliminary test results with 3-D print mini-channel

In this section the test results of 3-D print mini-channel are presented to show thermal performance of two-phase mini-channel cooling (TPMC) compared to single-phase mini-channel cooling (SPMC). The test is performed at three different flow rates: 1) 12.5ml/min, 2) 25ml/min and 3) 50ml/min. At each flow rate, different amounts of power dissipation are applied to the module and thermal performance is characterized. As described in previous section , HFE-7100 is used as coolant in the test. It is of interest to monitor thermal performance of power module in both single-phase regime (coolant temperature lower than HFE boiling point 61 °C) and two-phase regime (coolant temperature higher than HFE boiling point 61 °C).

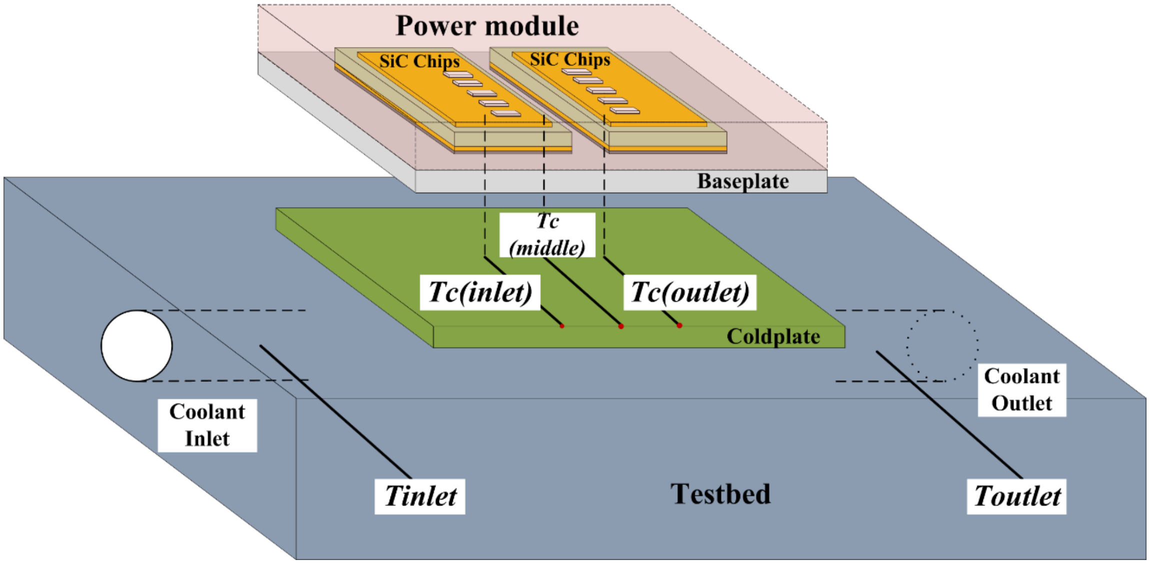

Figure 3.5 Schematic of thermocouples distribution

The operating conditions at the phase transition points for each of the three flow rates are listed in Table 3.2, where T_{outlet} is coolant temperature at outlet of coldplate, T_C(inlet)

Table 3.2 Summary of Phase Transition Points

Flow rate (ml/min)	P_{diss} (W)	T_{outlet} (°C)	$T_{C(inlet)}$ (°C)	$T_{C(middle)}$ (°C)	$T_{C(outlet)}$ (°C)
12.5	22.50	59.18	61.18	61.51	61.25
25	47.52	57.65	60.84	61.77	62.17
50	73.13	54.83	63.36	63.72	63.92

is module case temperature close to the side of coldplate inlet, T_C(outlet) is module case temperature close to the side of coldplate outlet, and $T_{C(middle)}$ is module case temperature in the midpoint between inlet and outlet of coldplate. The distribution of thermocouples is shown in Figure 3.5.

For each point, phase transition starts when T_C becomes larger than HFE boiling point 61 °C. However, the values of T_{outlet} are lower than 61 °C, which means that case temperature T_C is a better indicator of phase transition than outlet temperature T_{outlet}. The difference between the three measured case temperatures T_C at each flow rate is small, less than 1.5 °C. This indicates a uniform thermal distribution on the baseplate surface. Table 3.2 also shows that phase transition occurs at larger power dissipation for higher flow rate due to higher heat transfer capability. Higher flow rate leads to better cooling performance in single-phase cooling, but this is no longer true for two-phase cooling.

Another important indicator of phase transition is temperature variation ΔT of coolant between inlet and outlet of coldplate in Figure 3.6. The phase transitions arise at

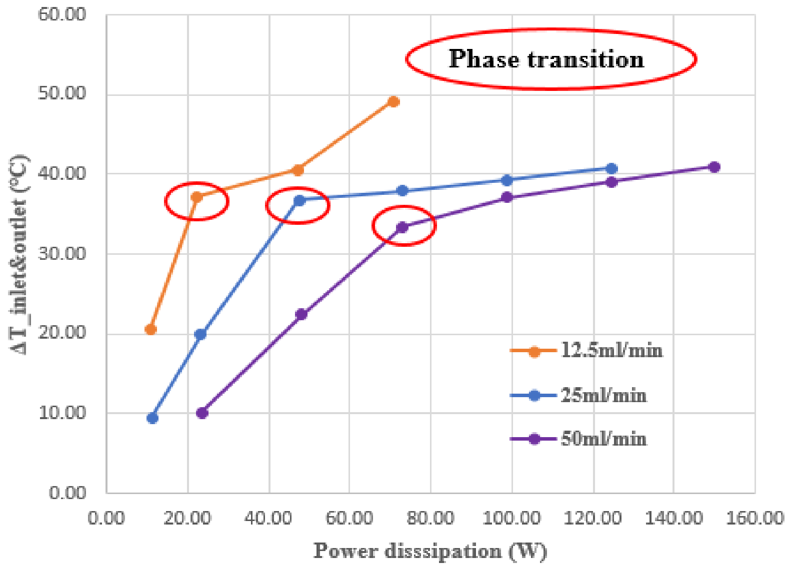

Figure 3.6 Temperature variation ΔT between inlet and outlet of coldplate

inflection points indicated by red ovals. In single-phase regime, ΔT exhibits an approximately linear increase with power dissipation, but it shows only a minor variation after phase transition, due to the fact that $T_{c(outlet)}$ becomes approximately constant at the boiling point temperature of coolant.

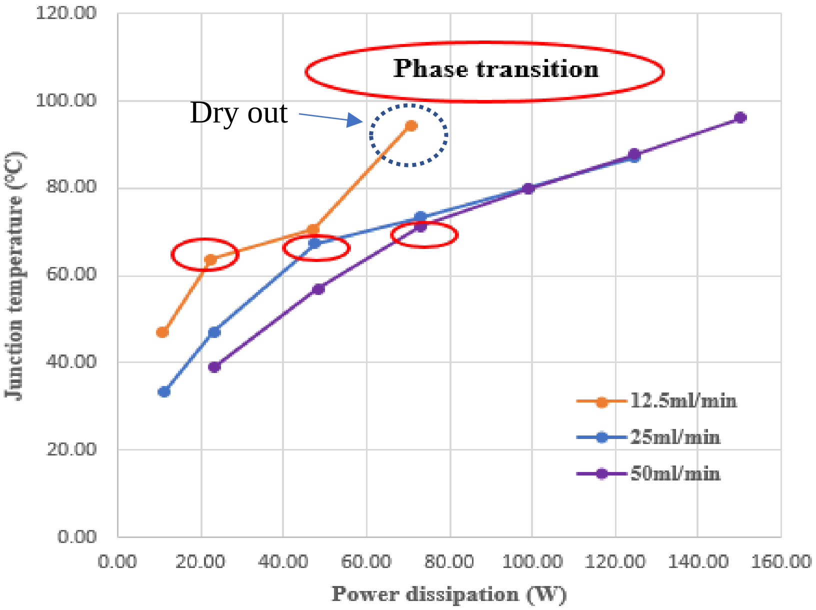

Figure 3.7 Junction temperature T_J estimated by T_C

The curve of junction temperature T_j (estimated from T_C using (3.2)) vs. power dissipation P_{diss} is shown in Figure 3.7. The slope of this curve after phase transition, defined as S_{2P}, is clearly smaller than the slope before phase transition, defined as S_{1P}. This shows that the thermal performance of TPMC is better than SPMC. The variations of power dissipation $\Delta P_{diss-1p}$ and junction temperature ΔT_{J-1p} before phase transition, and the $\Delta P_{diss-2p}$ and ΔT_{J-2p} after phase transition are compared in Table 3.3. For 25ml/min and 50ml/min, the values of ΔT_{J-2p} are significantly smaller than ΔT_{J-1p} for a similar power dissipation variation. The advantage can be seen by examining the first three data points of the

12.5ml/min curve. At this flow rate, $\Delta T_{J\text{-}2p}$ is only 6.89 °C compared with 16.76 °C of $\Delta T_{J\text{-}1p}$ when $\Delta P_{diss\text{-}2p}$ is approximately twice the value of $\Delta P_{diss\text{-}1p}$.

Table 3.3 Variation of power dissipation and junction temperature

Flow rate (ml/min)	$\Delta P_{diss\text{-}1p}$ (W)	$\Delta T_{J\text{-}1p}$ (°C)	$\Delta P_{diss\text{-}2p}$ (W)	$\Delta T_{J\text{-}2p}$ (°C)
12.5	11.58	16.76	24.7	6.89
25	24.34	20.41	25.56	5.99
50	24.92	14.53	25.78	8.39

To quantify the difference between the two cooling regimes, the quantity R_P is introduced in (3.3) as a function of S_{2P} over S_{1P}.

$$R_P = 1 - \frac{S_{2P}}{S_{1P}} \tag{3.3}$$

The values of S_{1P}, S_{2P}, R_P are listed in Table 3.4. R_P represents the improvement in junction temperature rise per unit power dissipation of TPMC compared with SPMC. For example, for 12.5ml/min flow rate, T_j for TPMC increases with power dissipation at a rate that is 81% improvement over the rate for SPMC. According to the data in Table 3.3, the advantage of TPMC is more significant at low flow rate, and less significant at higher flow rate. The R_P column shows the 58% improvement of T_j rise at 50ml/min versus the 73% improvement at 12.5ml/min and the 81% improvement at 25ml/min.

Thermal resistance of coldplate $R_{th(cp)}$ is a key parameter to quantify thermal performance directly. The definition is given in (3.4).

$$R_{th(cp)} = \left[Average(T_c) - \frac{T_{inlet} + T_{outlet}}{2} \right] / P_{diss} \tag{3.4}$$

Table 3.4 Parameters for thermal performance comparison

Flow rate (ml/min)	S_{1P} (°C /W)	S_{2P} (°C /W)	R_P (%)
12.5	1.45	0.28	81
25	0.94	0.25	73
50	0.66	0.27	58

The variation of $R_{th(cp)}$ with power dissipation at different flow rates is shown in Figure 3.8. The figure clearly shows that $R_{th(cp)}$ for TPMC case decreases remarkably compared with $R_{th(cp)}$ for SPMC case. The minimum of $R_{th(cp)}$ for TPMC case is 2.41 times, 2.37 times and 1.91 times smaller than that for SPMC case. As discussed previously in this section, the flow rate is no longer the dominant factor affecting the thermal performance for two-phase cooling. This is shown by the data in Figure 3.8. Between 70W and 125W the thermal resistance for the three flow rates is approximately the same.

In summary, the test results of initial mini-channel design demonstrate the advantages of TPMC compared with SPMC, but also point out some problems. A dryout problem can be observed in Figure 3.6 – see the last data point of the 12.5ml/min curve showing a sharp temperature increase. The local dryout tends to happen in the region close to the coolant outlet due to the accumulated heat and vapor flow. Another issue is relatively low maximum cooling power capability, caused by low heat transfer efficient.

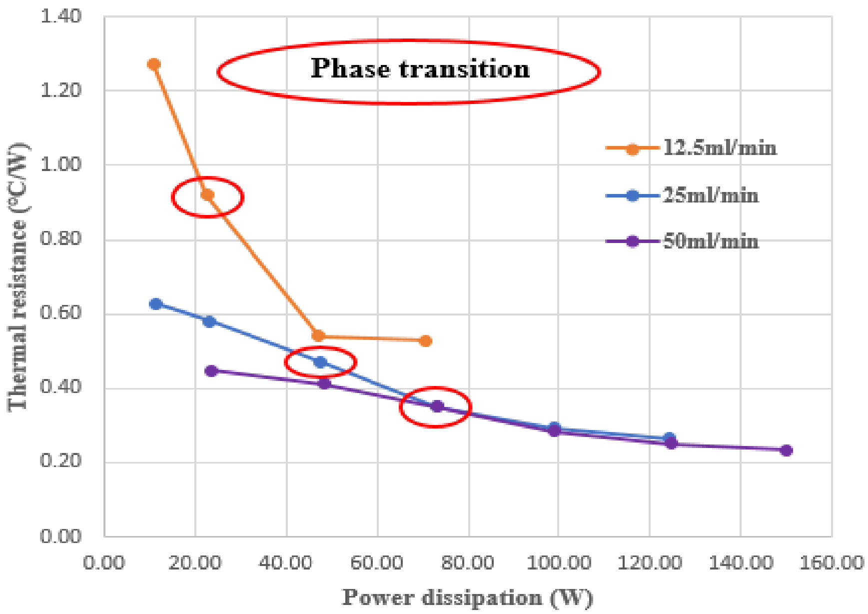

Figure 3.8 Thermal resistance calculated by T_C, T_{inlet}, T_{outlet} and P_{diss}

3.3 Optimization of mini-channel structure

To solve the two issues mentioned above, local dryout and low cooling capability, the mini-channel structure is redesigned to enhance flow boiling performance and water is used as coolant to increase cooling capability. As shown in Table 3.2, water has a better heat transfer performance vs HFE, such as ~20 times higher in latent heat and ~10 times larger in thermal conductivity. The solutions of optimized mini-channel structure include slot structure, micro-gap structure, and porous structure.

The slot structure is used in micro-channel to achieve rapid and sustainable nucleate boiling, and thus enhance heat transfer coefficient and critical heat flux [53]. In this design, the slots are fabricated by 3-D printing, as shown in Figure 3.9. The slots are introduced on the wall of channels, which enhance the lateral flow between the channels. The function of slots is like a jet nozzle. The coolant is accelerated to pass the slots and avoid a large vapor slug generated in the channel, which improves the flow boiling performance.

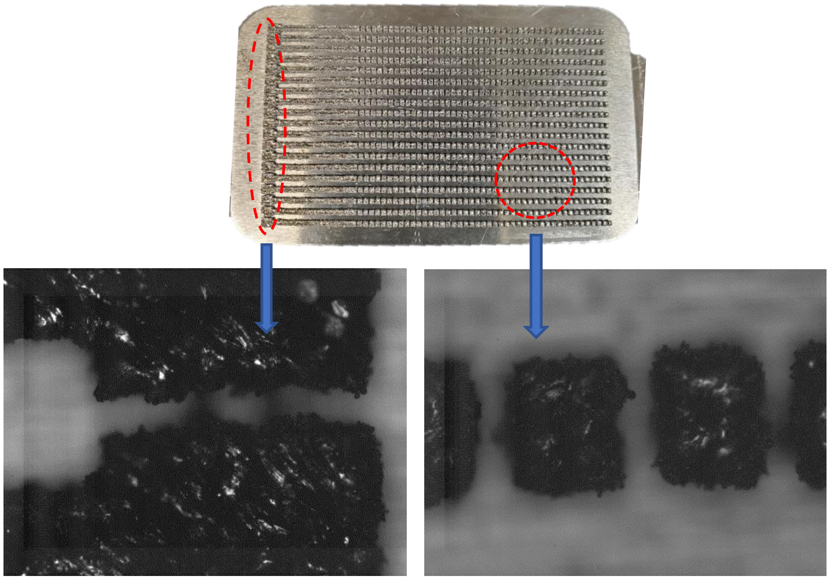

Figure 3.9 Slot structure by 3-D print

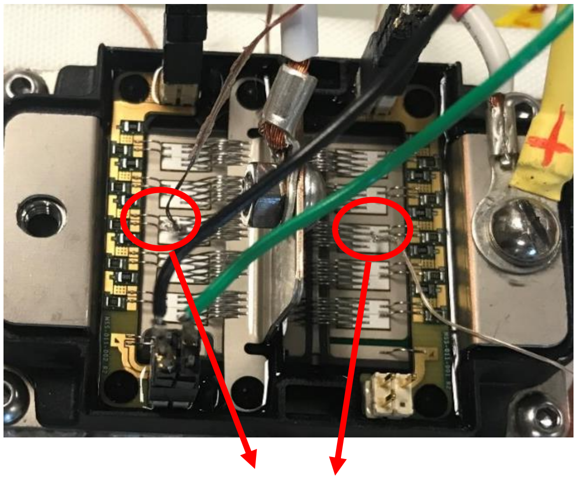

Thermocouples

Figure 3.10 Thermocouples for measurement of junction temperature

In the tests, both HFE and pure water are used to compare the thermal performance at different flow rate, 12.5ml/min, 25ml/min, 50ml/min, and 100ml/min respectively. The test setup as Figure 3.4 is used in experiments, adding two direct contact thermocouples on the middle chips of both sides to measure the junction temperature accurately as shown in Figure 3.10.

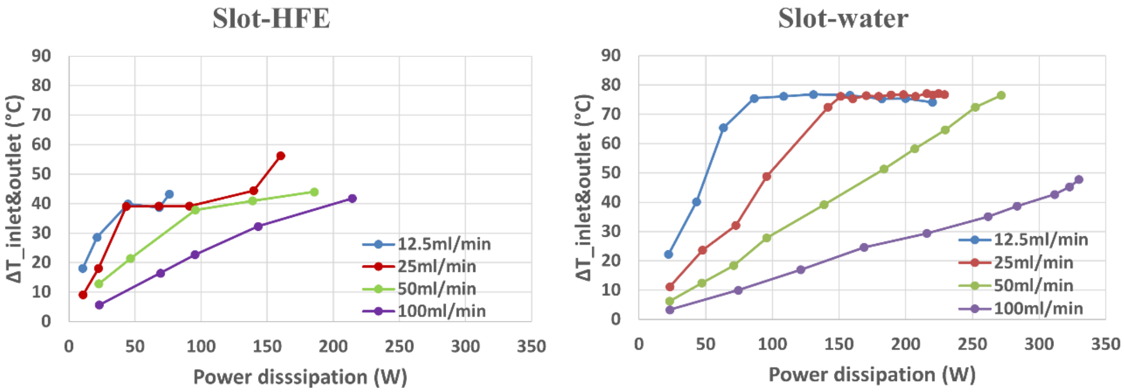

Figure 3.11 ΔT between inlet and outlet for slot structure with HFE and water

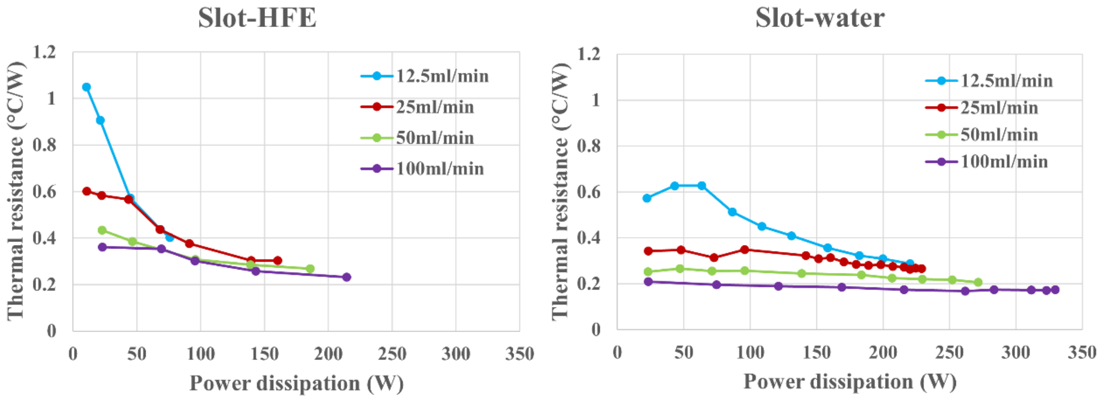

Figure 3.12 Thermal resistance of coldplate for slot structure with HFE and water

In Figure 3.11, ΔT between inlet and outlet for HFE and water is plotted. The difference between values of ΔT is resulting in the different boiling point 61 °C for HFE and 100 °C for water at 1 atmosphere. For the same reason, the coldplate with HFE enters two-phase regime earlier than with water, that is, the boiling starts at a lower power dissipation. Benefiting from a better property of water, the coldplate with water works at a higher power dissipation, especially at a higher flow rate. The maximum power dissipation increases ~115W. At the same time, the thermal resistance of coldplate with water is lower than with HFE, resulting in the larger ΔT between inlet and outlet, as shown in Figure 3.12.

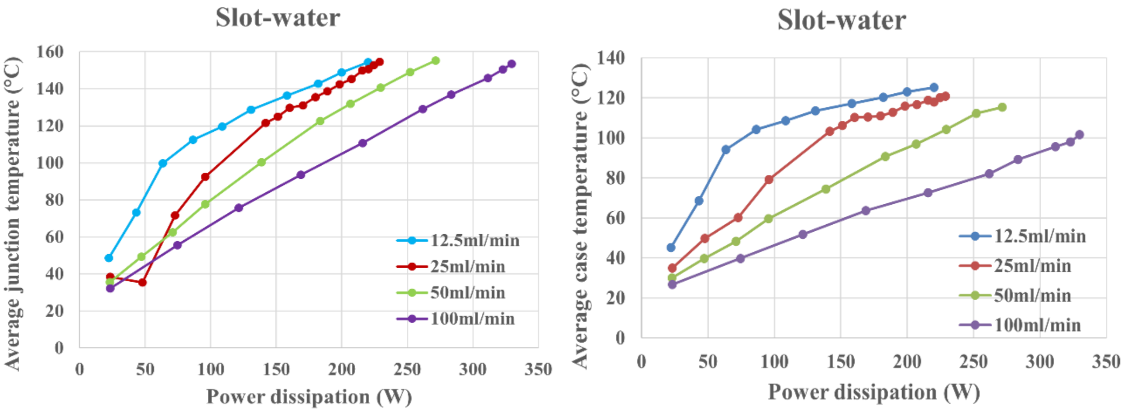

Figure 3.13 Average junction and case temperature of coldplate with water

The variation of average junction temperature (two test points) and case temperature (three test points) are shown in Figure 3.13. All tests at various flow rates are terminated when the junction temperature is close to 160 °C. The average case temperature is reverse proportional to the flow rate. However, the maximum power dissipation is still lower than expected.

3.3.2 Micro-gap structure in mini-channel

To further enhance cooling capability of the maximum power dissipation, a novel mini-channel with micro-gap structure is developed in this research, which can provide more uniform temperature distribution and lower thermal resistance of the coldplate. The concept of micro-gap is oriented from open micro/mini-channel [54]. Open micro-channels with tapered manifolds were reported to facilitate the vapor removal with reduced pressure drops of flow boiling [55]. Smaller size and more channels could lead to better heat dissipation capability in open microchannels [56]. Though the open microchannel configuration can provide comprehensively better flow boiling performance compared to closed microchannel flow boiling, studies of flow boiling in open mini-channels are limited.

In the test, a heating block is used instead of power module to avoid thermal failure at the higher power dissipation. The heating block is designed with same heating area as Wolfspeed^{TM} power module in Figure 3.1. The test section consisted of four parts: the mini-channel coldplate with transparent cover, the Garolite G7 housing block, the heating block and supporting plates. Four Cartridge heaters were inserted into the copper block ($31.75 \times 31.75 \times 72\ mm$). 3 mm thickness of the copper was maintained between the top surface of the heating block and the end of the heaters to simulate the baseplate of the Wolfspeed^{TM} power modules. The mini-channel coldplate was then installed on a Garolite G7 housing block to set up the flow loop along the mini-channel as shown in Figure 3.14. Four holes were drilled through the flow path plenum to install the thermocouples and pressure transducer. A through pocket was created at the center of the housing block to provide the visualization window of the mini-channel coldplate. Three grooves (width×depth: 1 mm×1 mm) with 14 mm intervals were fabricated for the insertion of three K-type thermocouples that can measure the wall temperature of the coldplate. The left space inside these grooves were filled with ceramic fiber to eliminate the effect of the attached heater.

Thermal grease was applied between the top surface of the heating block and coldplate surface. The ceramic fiber was wrapped over the heating block and the coldplate to reduce the heat loss from the test section. The heating block, coldplate, housing block were clamped together by screws and the supporting plates. During tests, the temperature and pressure readings were collected at 0.5 Hz for 60 points after the system reached steady state.

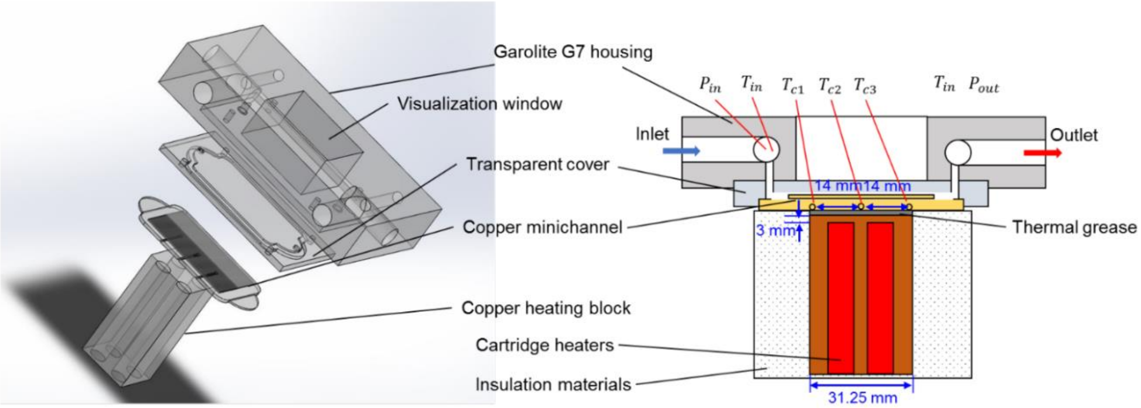

Figure 3.14 Schematic plot of the test setup with heating block

The heat loss P_{loss} to the environment through natural convection and radiation during the experiments is considered and calibrated by the temperature difference between the coldplate surface and ambient temperature in Figure 3.15. The coldplate surface temperature is measured when the heater is on, and the test setup reaches a steady state without working fluid in the ambient environment.

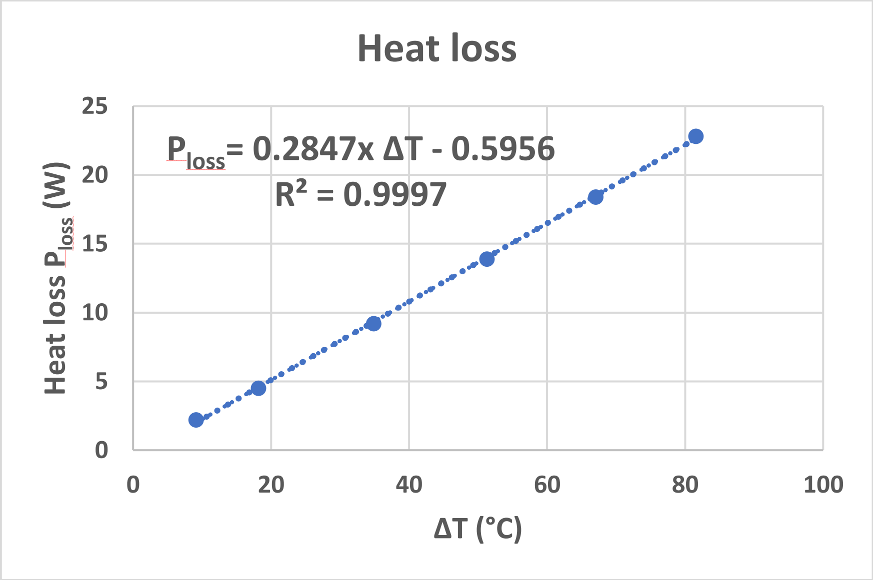

Figure 3.15 Experimental heat loss vs. the temperature difference between the coldplate surface and ambient temperature.

The effective power dissipation (heating power) P_{eff} is calculated by (3.5),

$$P_{eff} = P_h - P_{loss} \tag{3.5}$$

Where P_h is heating power of applied on heating block, equal to input voltage times input current. In the following section, “power dissipation” is used in consistent with previous discussion, which is equivalent to heating power.

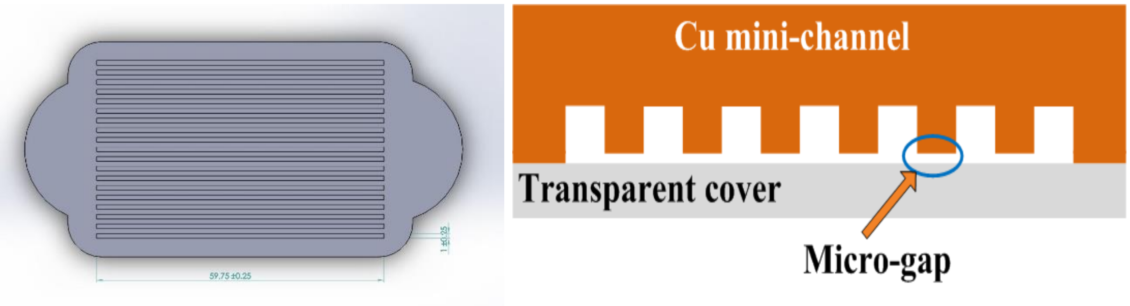

Figure 3.16 Schematic of mini-channel with micro-gap

The mini-channel coldplate with micro-gap structure is shown in Figure 3.16. The total 18 parallel mini-channels (channel width, depth, length: 1 mm×1 mm×59.75 mm) were fabricated on the pure copper substrate (thickness 3.175 mm) via computer-numerical-controlled (CNC) machining. The transparent window was made of polycarbonate plate with a designed pocket where the mini-channel part was installed. The size of the open gaps was varied by changing the depth of the cavity.

The design is based on a micro-gap that can sustain a thin liquid film along the top surface of mini-channels via capillary flow provides the best cooling performance. As shown in Figure 3.17, in a conventional mini-channel with vapor slug formation that causes local dryout and uneven temperature distribution. Conversely, the proposed micro-gap structure allows rewetting flow and vapor expansion across the micro-gap, preventing slug formation. The size of the gaps varied from 60 μm to 460 μm is studied to evaluate the effect of mini-channel flow boiling performance with different gaps. A zero gap (No gap) mini-channel coldplate is fabricated as a baseline. In Figure 3.18, the case temperature distribution of T_{c1}, T_{c2}, T_{c3} (from inlet to outlet) is shown with different gaps at flow rate 25ml/min and power dissipation 400W. It's clear that 60 μm gap coldplate (highlighted by red dash circle) has the best temperature uniformity, which is important to improve the reliability of power module. For the other cases, there are a large temperature difference between inlet and outlet, such as ~10 °C for no gap coldplate.

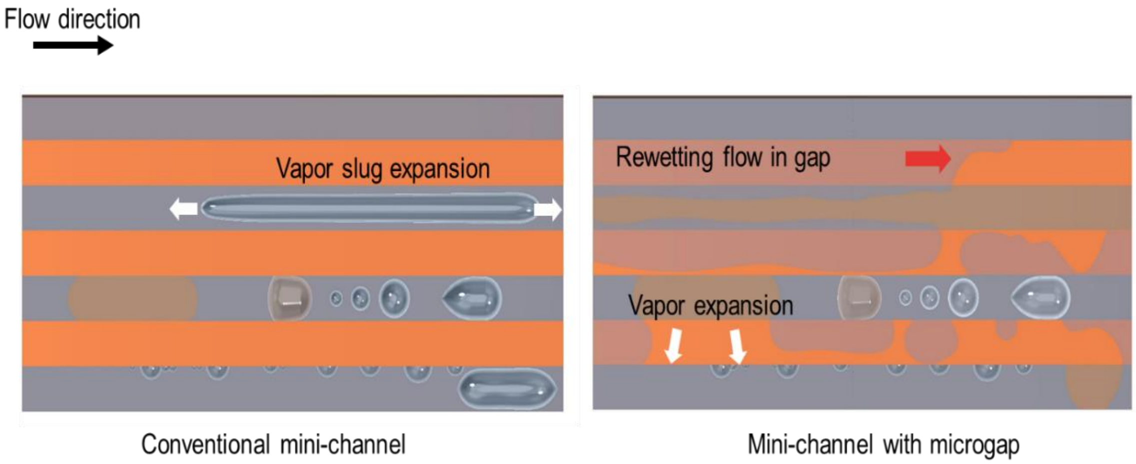

Figure 3.17 A pictorial representation of flow boiling in a conventional mini-channel leading to vapor slug formation (right) and flow boiling with the proposed micro-gap allowing rewetting flow and vapor expansion across mini-channels.

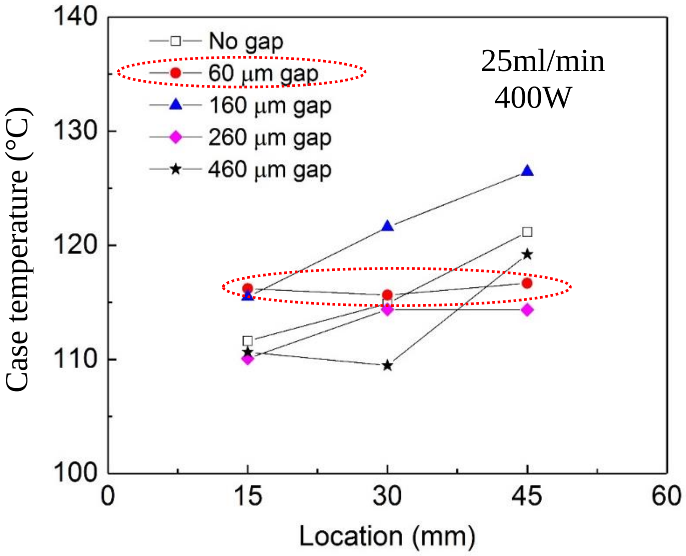

Figure 3.18 Case temperature distribution with different gaps @ 25ml/min, 400W

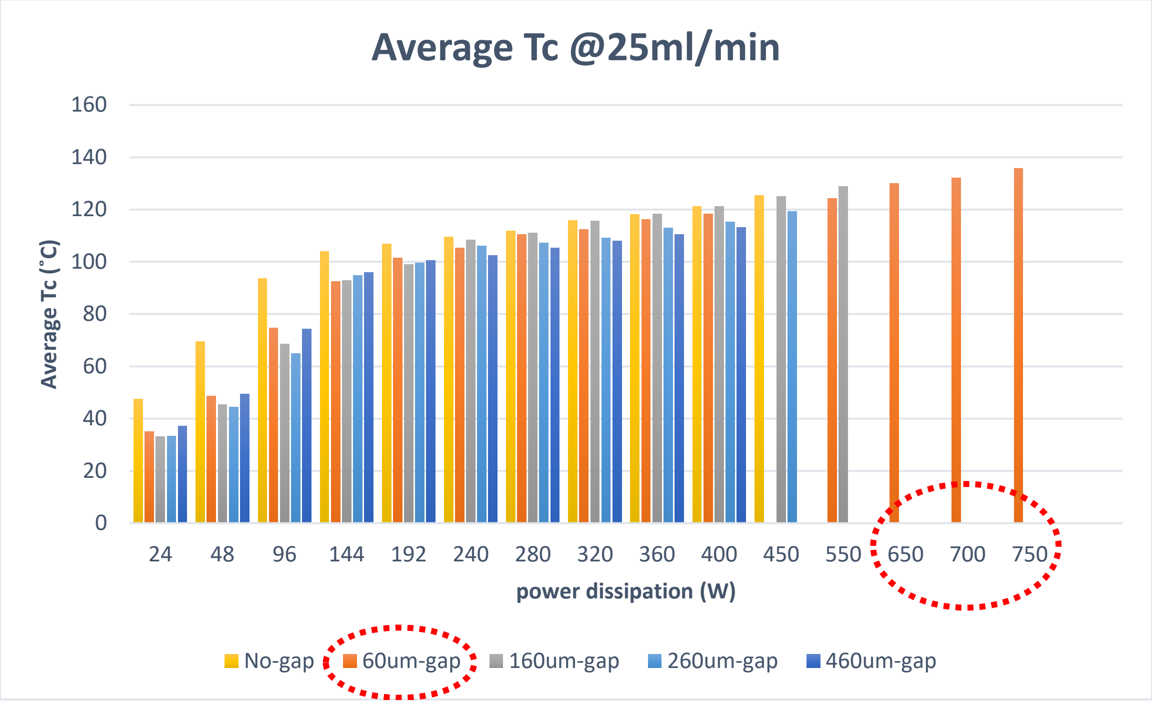

Figure 3.19 Average case temperature with different gaps vs. power dissipation

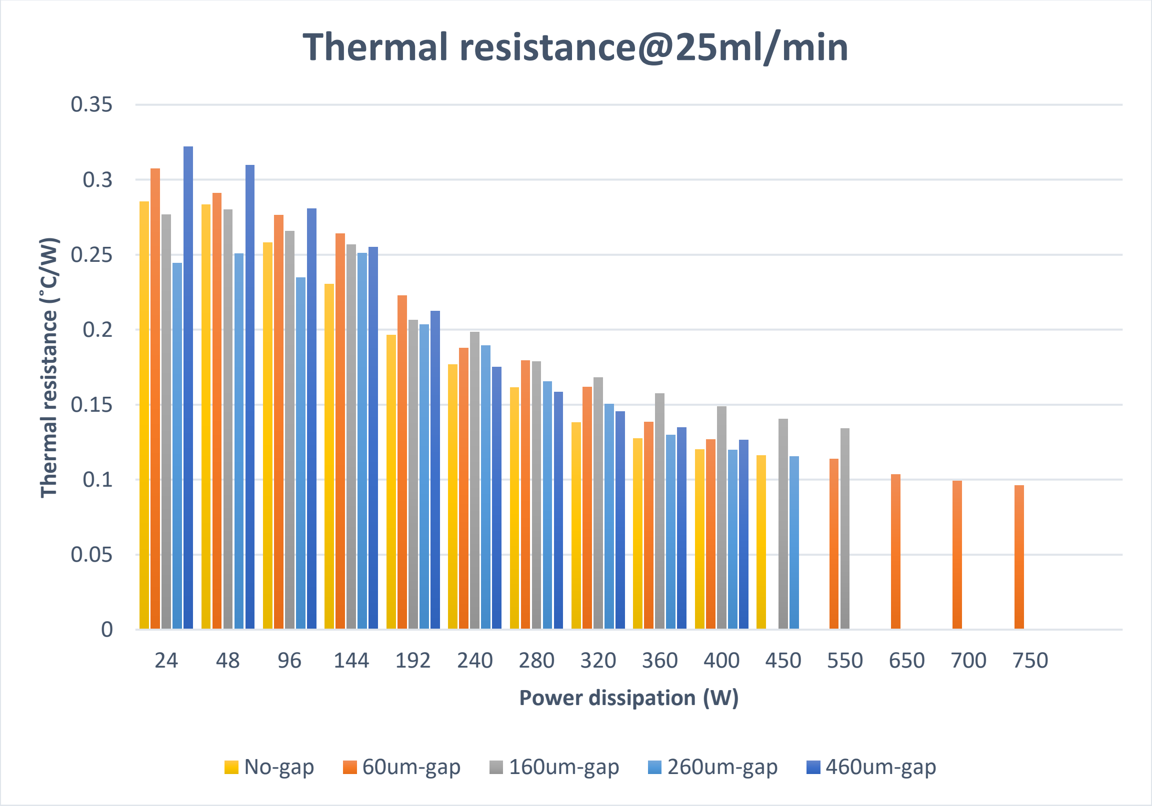

Figure 3.20 Thermal resistance of coldplate with different gaps vs. power dissipation

Figure 3.19 shows the average case temperature vs. power dissipation with different gaps at flow rate 25ml/min. The existence of gaps reduces the values of case temperature at a lower power dissipation. Along with the increase of power dissipation, the difference of case temperature between no gap and with gap coldplate becomes smaller. The last test point reached by all coldplates is 400W, after that, local dryout arises. For 550W power dissipation, only 160 µm gap and 60 µm gap still work, and the others can not be stable due to dryout. When the power dissipation keeps going up to 650W, 60 µm gap is the only one left, until 750W. A significant increase is achieved up to 300W of maximum power dissipation different from 60 µm gap to no gap coldplate.

In Figure 3.20, the thermal resistance of coldplate at flow rate 25ml/min is compared. In all cases, the thermal resistances are decreasing with the increase of power dissipation. It proves two-phase cooling is superior to single-phase cooling. The minimum thermal resistance of 60 µm gap is monitored at 750W, which is 28.1% reduction of no gap coldplate. Therefore, 60 µm gap is the best case in the study with optimal thermal performance, including maximum power dissipation capability, thermal resistance, and temperature uniformity. 60 µm gap is used for the following design and test, compared to conventional (no gap) mini-channel.

The flow in the mini-channel is studied on the pictures by high-speed camera, including no gap mni-channel (Figure 3.21) and 60 µm gap mini-channel (Figure 3.22). The frame rate is 1000 fps. In Figure 3.21 a) and b), the water flow is filled in the channel. The bubble arises in Figure 3.21 c), which shows the onset of nucleate boiling. With more bubbles generated, a large vapor slug is formed resulting in local dryout shown in Figure 3.21 d). It lasts until rewetting flow coming shown in Figure 3.21 e). In this situation, the

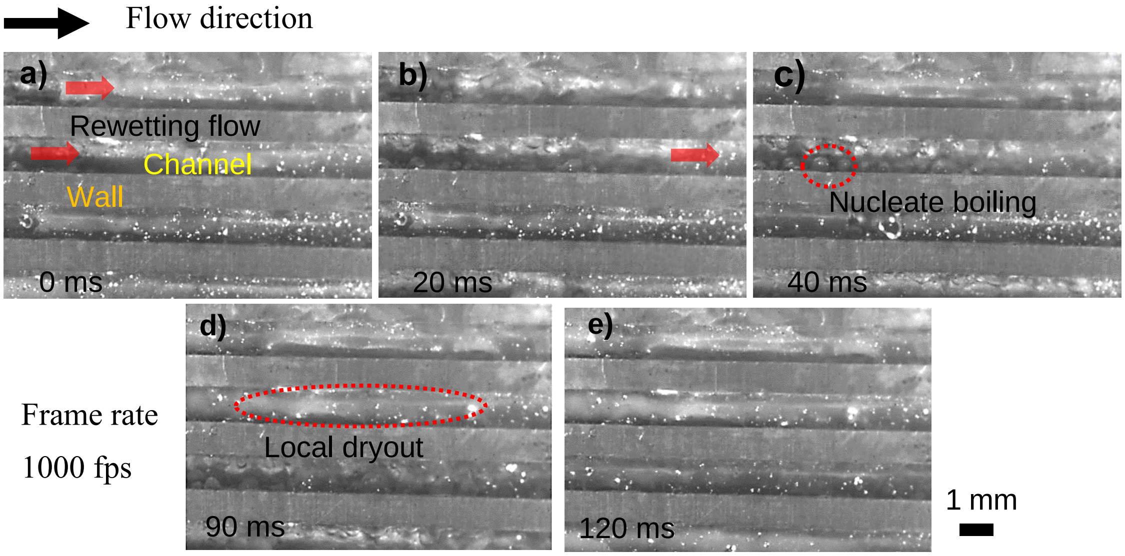

Figure 3.21 Flow pattern in no gap mini-channel at 550W, 25ml/min

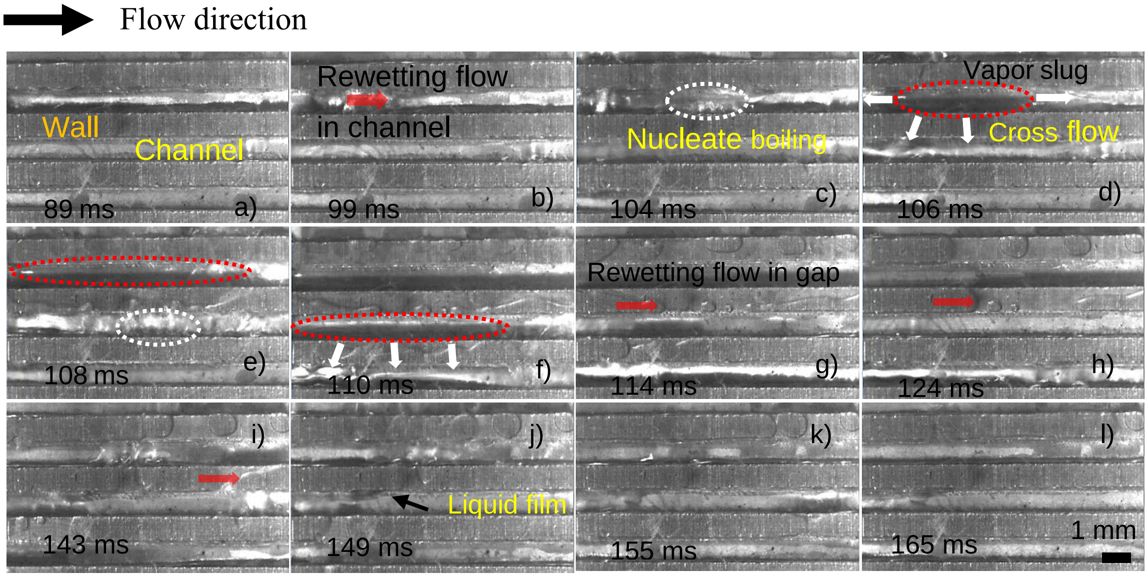

Figure 3.22 Flow pattern in 60 μm gap mini-channel at 650W, 25ml/min

dryout issue caused by large vapor slug is not avoidable. The issue is solved by vapor expansion across the micro-gap as shown in Figure 3.22. Onset of nucleate boiling is shown in Figure 3.22 c). The vapor slug expands across the micro-gap in Figure 3.22 d), and it is observed as well in Figure 3.22 f). A rewetting flow is monitored in the micro-gap as shown in Figure 3.22 g), which makes the channel staying wet, such as liquid film in Figure 3.22

j), until next rewetting flow coming. The results perfectly prove the effectiveness of using micro-gap to enhance thermal performance and avoid local dryout in mini-channel coldplate.

The flow in the mini-channel is studied on the pictures by high-speed camera, including no gap mni-channel (Figure 3.21) and 60 µm gap mini-channel (Figure 3.22). The frame rate is 1000 fps. In Figure 3.21 a) and b), the water flow is filled in the channel. The bubble arises in Figure 3.21 c), which shows the onset of nucleate boiling. With more bubbles generated, a large vapor slug is formed resulting in local dryout shown in Figure 3.21 d). It lasts until rewetting flow coming shown in Figure 3.21 e). In this situation, the dryout issue caused by large vapor slug is not avoidable. The issue is solved by vapor expansion across the micro-gap as shown in Figure 3.22. Onset of nucleate boiling is shown in Figure 3.22 c). The vapor slug expands across the micro-gap in Figure 3.22 d), and it is observed as well in Figure 3.22 f). A rewetting flow is monitored in the micro-gap as shown in Figure 3.22 g), which makes the channel staying wet, such as liquid film in Figure 3.22 j), until next rewetting flow coming. The results perfectly prove the effectiveness of using micro-gap to enhance thermal performance and avoid local dryout in mini-channel coldplate.

3.3.3 Porous structure in mini-channel

Another investigated improvement is the use of a porous structure. The flow boiling performance is enhanced by covering the surface with capillary-porous structures sintered or deposited on the surface [57]. The porous layers on the microchannel surfaces are normally fabricated by sprayed painting [58], diffusion-brazing [59], or sintering [60]. A number of experimental researches on pool boiling from the sintered microporous surfaces

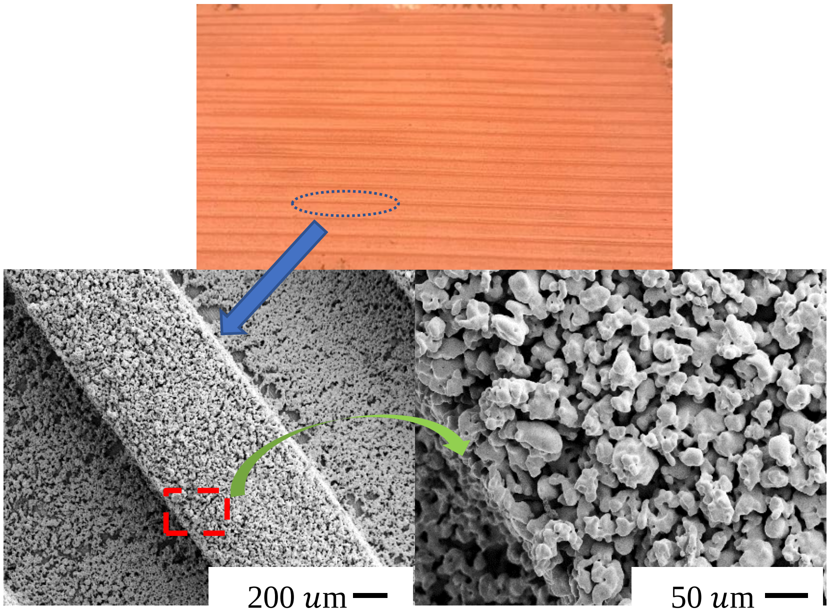

Figure 3.23 Porous structure by copper sintering

have shown that these surfaces provide excellent boiling enhancement [61-65]. The porous mini-channel in this study is fabricated by sintering copper particles on the copper plate, as shown in Figure 3.23. From the SEM (scanning electron microscope) pictures, one can clearly see the porous structure on the surface. The porous structure can hold more liquid on the surface due to capillary force. This means that the channel surface can remain wet even when vapor bubbles generated, which is helpful to avoid local dryout. The thermal performance of porous structure mini-channel is investigated by power module (low power dissipation) and heating block (high power dissipation).

3.3.3.1 Experiment of porous mini-channel by power module

The test is performed at two flow rates: 12.5ml/min and 25ml/min. At each flow rate, different amounts of power dissipation are applied to the module until thermal equilibrium and thermal performance is characterized. In the test, pure water is used as coolant. When the case temperature is lower than 100°C, power module operates in single-phase regime;

when it is equal or higher than 100°C the module enters two-phase regime. The case temperature distribution is shown in Figure 3.24. In single-phase regime, notice the thermal gradient from low to high corresponding to the sequence of Tc_inlet, Tc_middle and Tc_outlet as expected. The transition from single-phase to two-phase on a large scale exhibits two stages. In the first stage, the temperature at outlet attains 100°C first, followed by the middle and eventually by the inlet. This phase is called “initial boiling”. The second stage, in which all temperatures are equal or higher than 100°C, is called “complete boiling”. This is shown in the experimental results of Figure 3.24 for both flow rates. The difference between the two flow rates is that higher flow rate starts entering two-phase regime at higher power dissipation. Another change is thermal distribution. In the two-phase regime, the maximum temperature is not located at the outlet, but in the middle, and is affected by multiple factors, such as channel structure, manifold arrangement and so on. Moreover, the uniformity of thermal distribution is highly improved as shown in phase Figure 3.25. The maximum case temperature difference ΔTc(max) is used to measure the

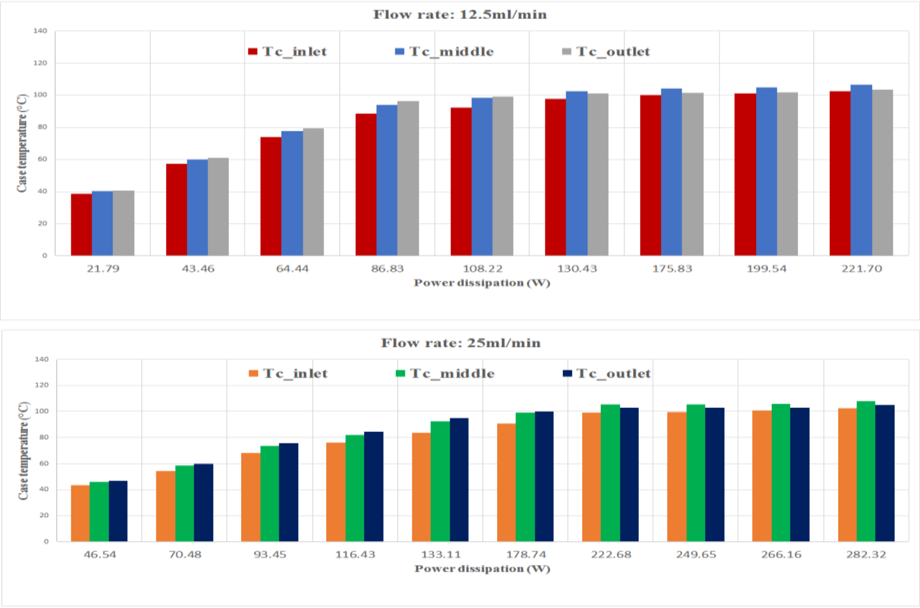

Figure 3.24 Case temperature distribution

uniformity of thermal distribution. According to the Figure 3.25, ΔTc (max) in single-phase regime is calculated between Tc_outlet and Tc_inlet; while ΔTc(max) in two-phase regime is calculated between Tc_middle and Tc_inlet. Comparing the data at the same flow rate, for 12.5ml/min, ΔTc (max) in single-phase regime is equal to 7.9 °C @ power dissipation = 86.83W; and ΔTc (max) in two-phase regime is equal to 3.98 °C @ power dissipation = 175.83W, showing that two-phase cooling has 2 times lower ΔTc (max) compared with single-phase cooling even though dissipated power is double. For 25ml/min, ΔTc (max) in single-phase regime is equal to 11.06 °C @ power dissipation = 133.31W; and ΔTc (max) in two-phase regime is equal to 5.25 °C @ power dissipation = 266.16W, which is similar as 12.5ml/min. This shows that two-phase cooling is effective in improving the uniformity of power module thermal distribution.

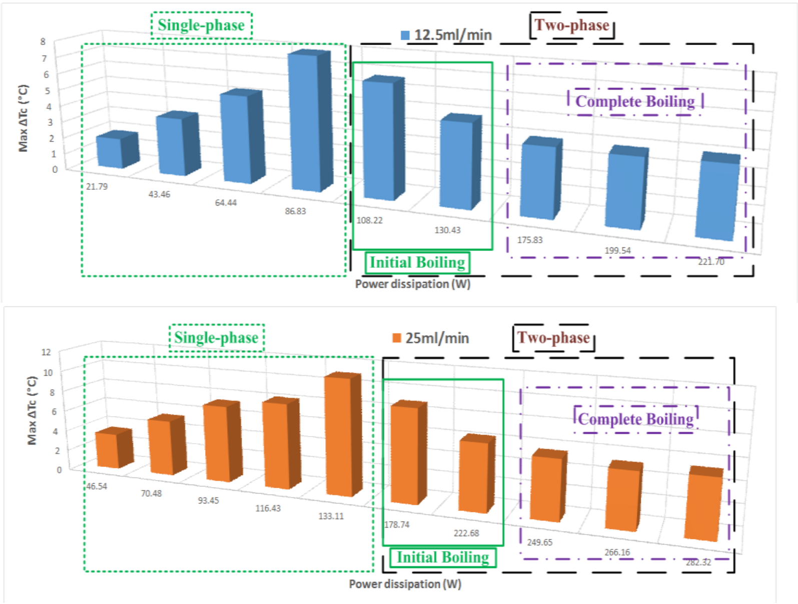

Figure 3.25 Maximum case temperature difference ΔTc(max)

ΔT_{jc} is calculated by Tj measured by NTC thermistor and the lowest case temperature. Based on [48], the lifetime of power module for single-phase and two-phase cooling is estimated using ΔT_{jc} as shown in Table 3.5. At similar power dissipation, despite a higher flow rate, single-phase cooling still has 11°C higher ΔT_{jc} than two-phase cooling, which results in 10 times reduction of estimated lifetime of power module.

Table 3.5 Comparison of estimated lifetime of power module at single- and two-phase cooling

	Power dissipation (W)	Flow rate (ml/min)	ΔT_{jc} (˚C)	Est. Lifetime (cycles)
Single-Phase	133.11	25	31.61	2.08E+08
Two-Phase	130.43	12.5	20.59	2.72E+09

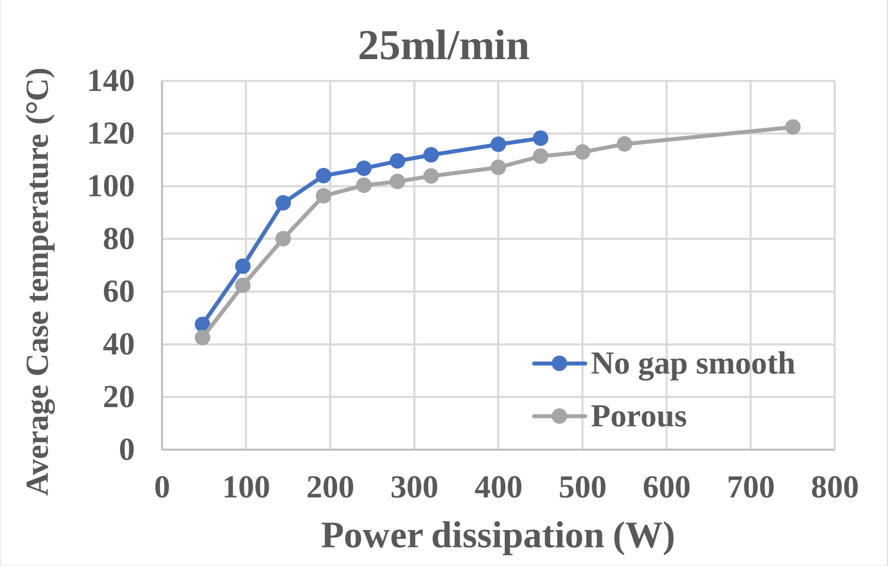

Figure 3.26 Average case temperature of no gap smooth vs. porous coldplate at 25ml/min

3.3.3.2 Experiment of porous mini-channel by heating block

Using heating block instead of power module in a higher heating power is safe and to avoid unnecessary module failure due to the risk from uncertainties. As shown in Figure 3.26, compared with conventional (no gap) coldplate at flow rate 25ml/min, the porous structure has a lower case temperature at the same power dissipation, and the maximum power dissipation is 300W higher, which is same as micro-gap mini-channel. A 37.5% reduction of the thermal resistance is achieved in Figure 3.27, which is a little better than micro-gap mini-channel. Therefore, both micro-gap and porous structure improve the thermal performance of mini-channel coldplate in the maximum power dissipation capability and thermal resistance.

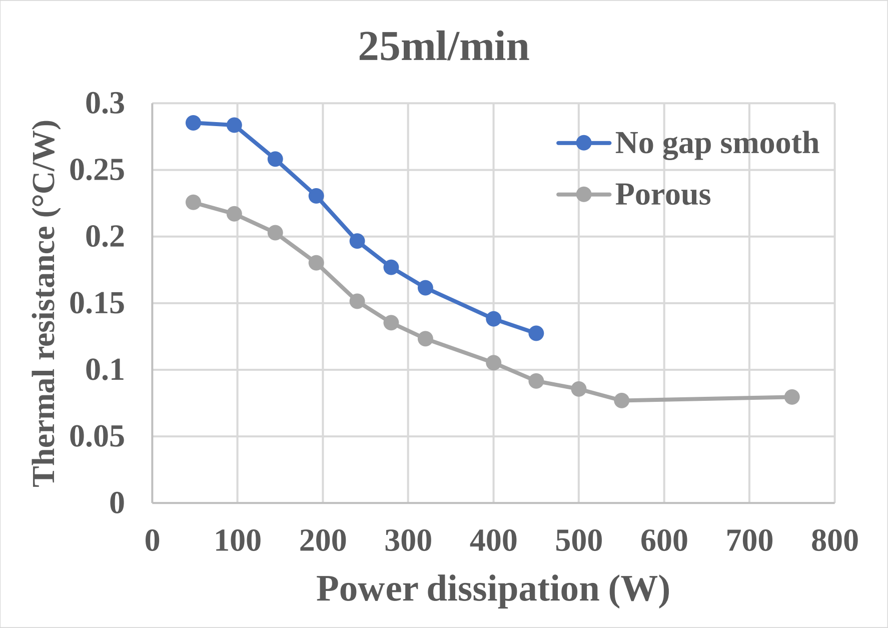

Figure 3.27 Thermal resistance of no gap smooth vs. porous coldplate at 25ml/min

3.3.4 Novel porous mini-channel with micro-gap and reservoir channel

Based on the previous study, a novel porous mini-channel with micro-gap and reservoir channel is proposed. The schematic structure, local image and SEM image are shown in Figure 3.28. The proposed mini-channel introduces a shallow reservoir channel on the top surface of each mini-channel. The reservoir channels provide additional flow path to avoid local dryout. At the same time, combined porous and micro-gap structure is expected to improve thermal performance further.

The proposed porous mini-channel with reservoir channels on the top was fabricated by the conventional high-temperature sintering process. A graphite plate was designed with

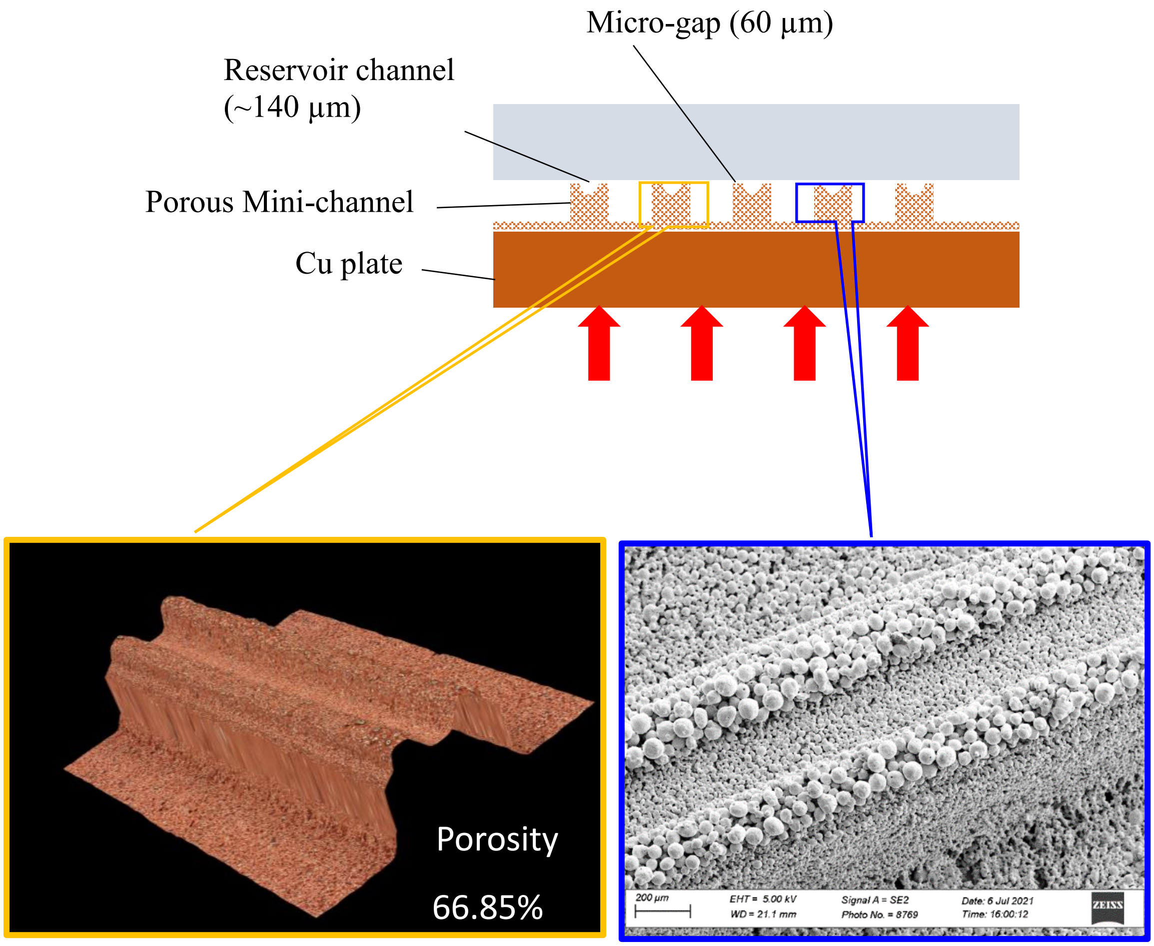

Figure 3.28 Proposed porous mini-channel with micro-gap and reservoir channel

the channel shapes as the sintering mold. A small pocket with the depth of 0.1 mm was first created on the graphite plate to construct the bottom wall with porous structure. 19 mini-channels with 1 mm width and 0.6 mm depth were further fabricated by the end mill. Then the edge of the mini-channels was further deepened by the drill bit (0.5 mm with 30° on the tip, McMASTER-CARR) to 1 mm depth. The copper powder (99.8%, mesh 325 from MiniScience Inc.) was evenly distributed into the channel structures on the sintering mold. A pure copper substrate (thickness, length, and width: 3.175 mm, 91.14 mm and 44.75mm) was then attached to the sintering mold to construct the designed mini-channel structures with reservoir channels on the top surface. Two ceramic plates were used to press the mold and copper substrate during the channel sintering process.

The proposed heat sink with 18 porous mini-channels (channel width, depth, length: 1 mm×1 mm×59.75 mm) with trapezoid reservoir channels on the top were manufactured in the furnace with 1010°C, 30min. Due to the gravity effect during sintering process, there existed minor error on the geometry of the top surface of reservoir channels. The Leica FreDCM8 applied with the optical coherence tomography and SEM images were used to demonstrate the exact size of the reservoir channels.

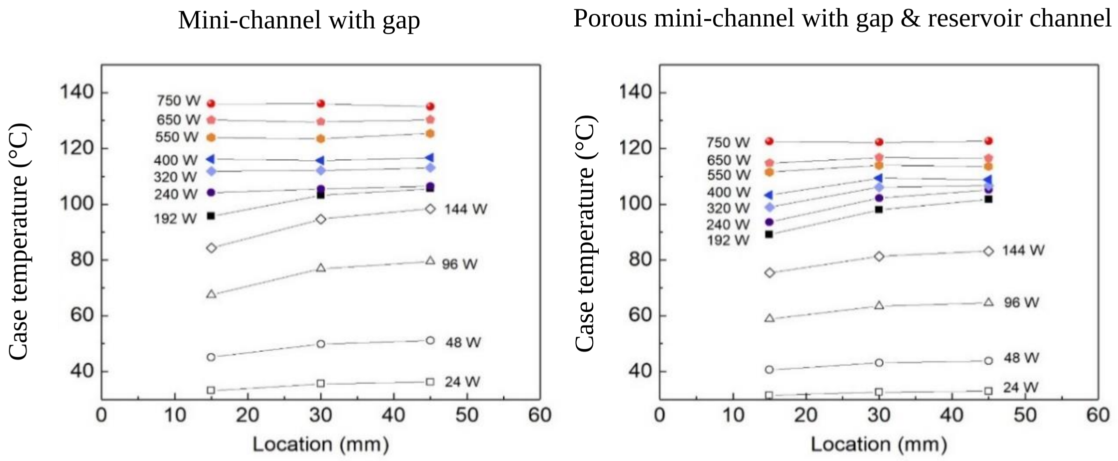

Figure 3.29 Case temperature of mini-channel with gap vs. porous mini-channel with gap & reservoir channel at flow rate 25ml/min

In Figure 3.29, the case temperature distribution at different power dissipation is compared between mini-channel with gap and porous mini-channel with gap and reservoir channel at flow rate 25ml/min, the gap is same as 60μm. The porous mini-channel with reservoir channel keeps the advantage of uniform temperature distribution in two-phase regime. Furthermore, the porous mini-channel with reservoir channel archives a significant reduction in average case temperature, and it’s up to 13 °C when power dissipation is 750W. The lower case temperature means a lower junction temperature, in other words, the proposed porous mini-channel with micro-gap and reservoir channel has a higher heat transfer capability at the same case temperature constrain, which makes it working at the higher power dissipation and fits the cooling requirement of high density heat flux in power module.

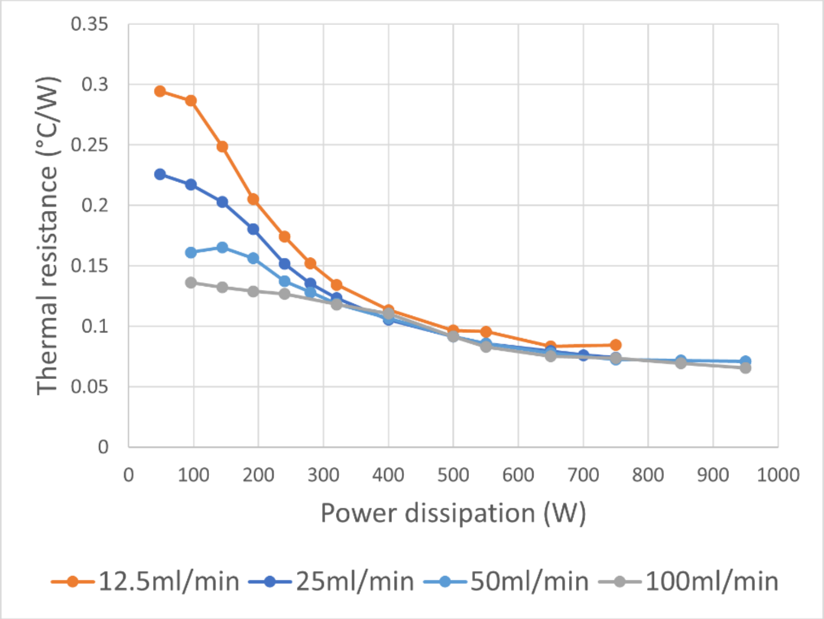

Figure 3.30 Thermal resistance of porous mini-channel with micro-gap and reservoir channel vs. power dissipation at various flow rates

Figure 3.30 shows the thermal resistance of proposed mini-channel vs. power dissipation at four various flow rates. At the low flow rate, such as 12.5ml/min and 25ml/min, in single phase regime, the thermal resistance drops quickly, and slows down when entering the two-phase regime, and saturated at the high power dissipation 750W. At the high flow rate, 50ml/min and 100ml/min, the slop of thermal resistance's variation has a small change from single-phase to two-phase, and close to saturation at power dissipation 950W. High flow rate increases the heat transfer capability, resulting in a lower thermal resistance. The minimum thermal resistance of each flow rate is 0.084°C/W at 12.5ml/min, 0.074°C/W at 25ml/min, 0.071°C/W at 50ml/min, and 0.066°C/W at 100ml/min.

Compared the values between 100ml/min and 12.5ml/min, the thermal resistance is reduced 21.4%.

3.4 Summary

The mini-channel is fabricated by 3D printing to successfully demonstrate the advantages of two-phase cooling. To improve the mini-channel heat transfer capability, slot mini-channel and porous mini-channel are investigated, which is helpful to increase the power dissipation capability, but not enough to satisfy the requirements of power module thermal management. Micro-gap is introduced in the mini-channel design, enhancing the thermal performance significantly. A novel porous mini-channel with micro-gap and reservoir channel is proposed to increase heat transfer capability and avoid local dry out. The proposed structure is expected to improve thermal performance further.

CHAPTER 4

INTEGRATION OF TWO-PHASE MINI-CHANNEL COOLING IN SIC POWER MODULE

The key of improving thermal performance of power module is reducing thermal resistance. In previous discussions, the focus is to design and optimize a high HTC two-phase mini-channel cooling to reduce thermal resistance of coldplate. In this section, the research point is how to reduce thermal resistance of power module.

4.1 Analysis of thermal resistance in the SiC power module

In this section, Wolfspeed^{TM} SiC power module is still used to analyze thermal resistance as shown in Figure 4.1. The integrated cooling solution with two-phase mini-channel (Figure 4.1 (b)) is proposed in the study to replace the conventional cooling (Figure 4.1,(a)). The baseplate and TIM are removed in integrated cooling, and the improvement of thermal performance is estimated below.

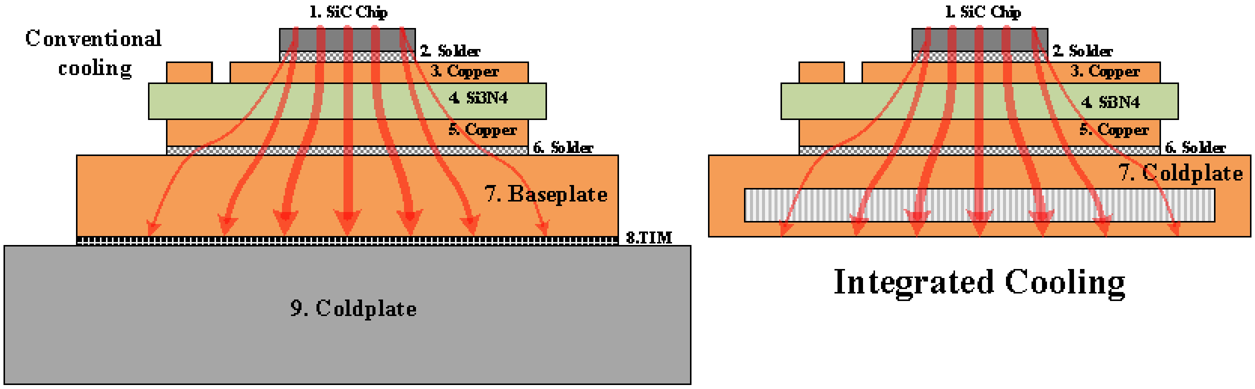

(a) (b)

Figure 4.1 SiC power module with cooling (a) Conventional cooling, (b) Integrated two-phase cooling.

Table 4.1 Thermal resistances of power module with conventional cooling

Material/Layer	Thickness (mm)	Thermal Conductivity (W/m·°C)	Effective Area (mm^2)	Rth / layer (°C/W)
1. SiC (chip)	0.4	20	280	0.071
2. Solder SAC (under chip)	0.1	60	280	0.006
3. Cu (DBC top)	0.3	385	313.12	0.0025
4. Si3N4 (DBC ceramic)	0.635	90	387.97	0.018
5. Cu (DBC bottom)	0.3	385	425.58	0.0018
6. Solder SAC (under DBC)	0.1	60	425.58	0.0039
7. Cu (baseplate)	3	385	880.86	0.0089
8. TIM	0.2	4.6	880.86	0.049
9-a. Cu (coldplate upper part)	2	385	1264.38	0.0041
9-b. Conventional cooling (Convection)	HTC = 10000 $W/m^2 \cdot k$		2800	0.036
Total thermal resistance				**0.202 °C/W**

Table 4.2 Thermal resistances of power module with integrated two-phase mini-channel cooling

Material/Layer	Thickness (mm)	Thermal Conductivity (W/m·°C)	Effective Area (mm^2)	Rth/layer (°C/W)
1. SiC (chip)	0.4	20	280	0.071
2. Solder SAC (under chip)	0.1	60	280	0.006
3. Cu (DBC top)	0.3	385	313.12	0.0025
4. Si3N4 (DBC ceramic)	0.635	90	387.97	0.018
5. Cu (DBC bottom)	0.3	385	425.58	0.0018
6. Solder SAC (under DBC)	0.1	60	425.58	0.0039
7-a. Cu (coldplate upper part)	2	385	713.1	0.0073
7-b. Enhanced two-phase cooling	HTC = 20000 $W/m^2 \cdot k$		3600	0.014
Total thermal resistance				**0.125 °C/W**

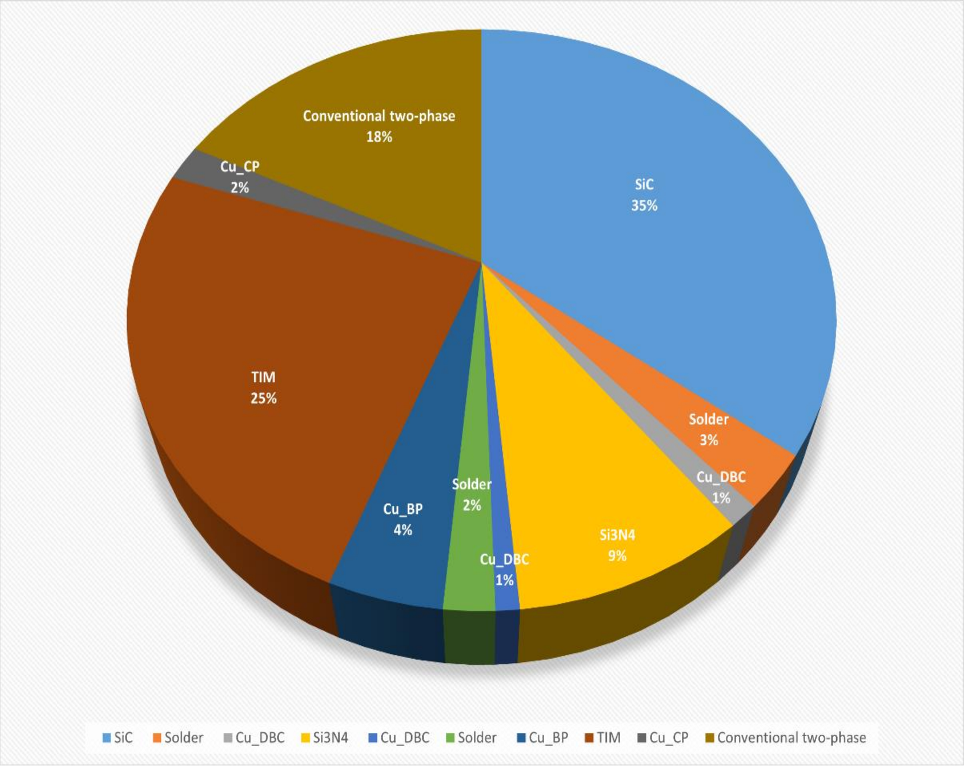

Figure 4.2 Composition of thermal resistances of power module with conventional cooling

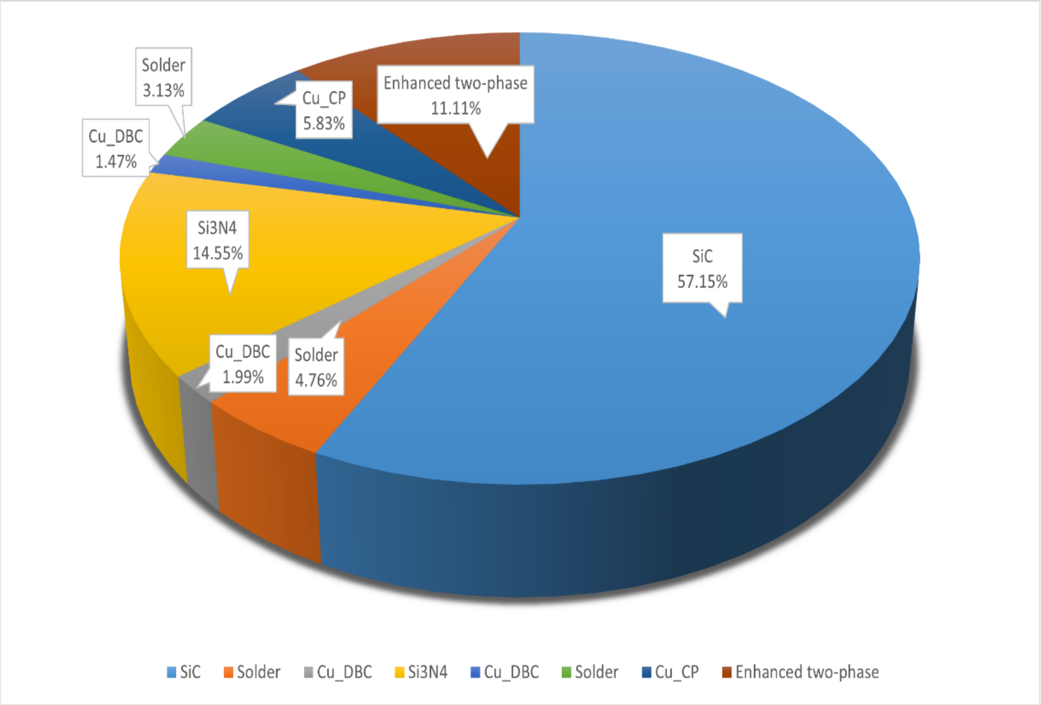

Figure 4.3 Composition of thermal resistances of power module with integrated cooling

According to the equivalent Cauer RC thermal network in section 1.1, there are several layers contributing to the total thermal resistance of power module. The thermal resistance Rth of each layer is calculated by equations (2) and (3). In Table 4.1, thermal resistances of power module with conventional cooling as Figure 4.1 (a) is calculated.

Thermal resistances of power module with integrated cooling as Figure 4.1 (b) is listed in Table 4.2. The 45˚ spreading angle is applied in the calculation of thermal resistance for each layer. In Table 4.1, the thermal resistance from layer 1 to 7 (chip to baseplate) is 0.113°C/W, which perfectly matches the value given in the datasheet. Total thermal resistances in Table 4.1 and Table 4.2 represent thermal resistance from chip to coldplate, that is R_{thja} from junction to ambient. The removal of baseplate and TIM, and the utilization of two-phase mini-channel cooling instead of conventional cooling allow a significant reduction of R_{thja}, 0. 125°C/W vs 0.202°C/W, which is a 38.1% reduction. Figure 4.2 clearly shows that the dominant contributors to the overall thermal resistance are the coldplate, the chip and the TIM layer in the power module with conventional cooling. In the integrated cooling module, as shown in Figure 4.3, the main contributions to the thermal resistance still come from chip and coldplate, however, the proportion of thermal resistance contributed by the coldplate in the integrated two-phase cooling module

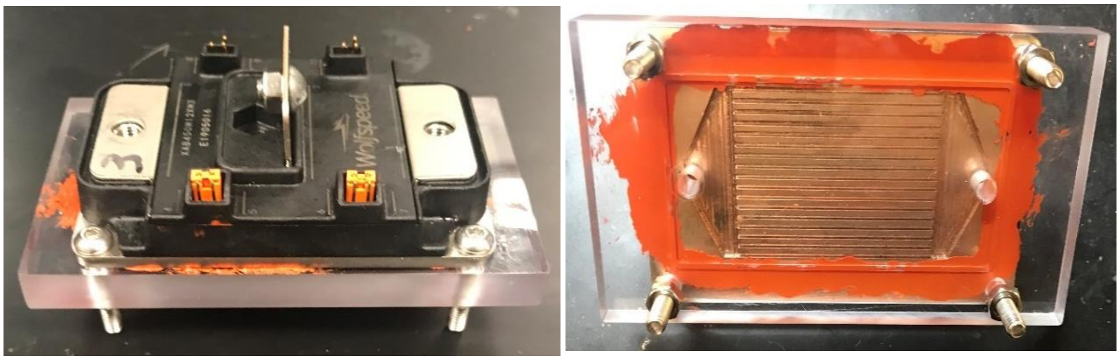

Figure 4.4 Integrated two-phase mini-channel on the backside of SiC power module

decreases to 11.11% of total, vs 18% of total in conventional cooling. Furthermore, based on the dimension and geometry of power module, the designed mini-channel is feasible to integrate the two-phase mini-channel in the baseplate of the power module through a regular milling process.

4.2 Demonstration of integrated two-phase mini-channel cooling on the SiC power module

The same Wolfspeed^{TM} SiC MOSFET module CAB450M12XM3 is used to demonstrate integrated two-phase mini-channel cooling as shown in Figure 4.4. The channels are fabricated on the baseplate of power module on the backside. A glass cover, sealed by silicone gel on the backside surface, is used to observe the coolant flow in the channel.

4.2.1 Experimental setup

Junction temperatures are acquired by thermocouples in direct contact with the surface of chips as shown in Figure 4.5. To guarantee a good contact between thermocouple and chip, and avoid damage to the surface insulation of chip, micropositioners are used to precisely control the position of thermocouples as shown in Figure 4.6 and Figure 4.7.

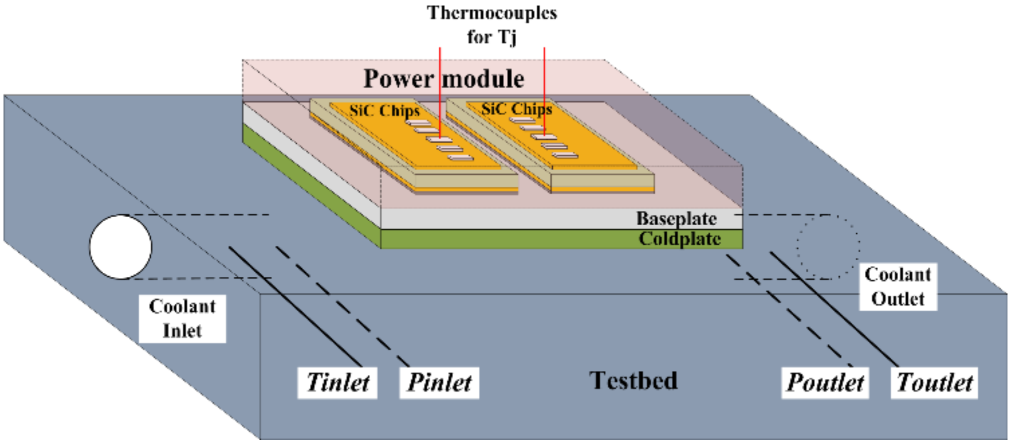

Figure 4.5 Schematic of sensor positions to acquire parameters in the test.

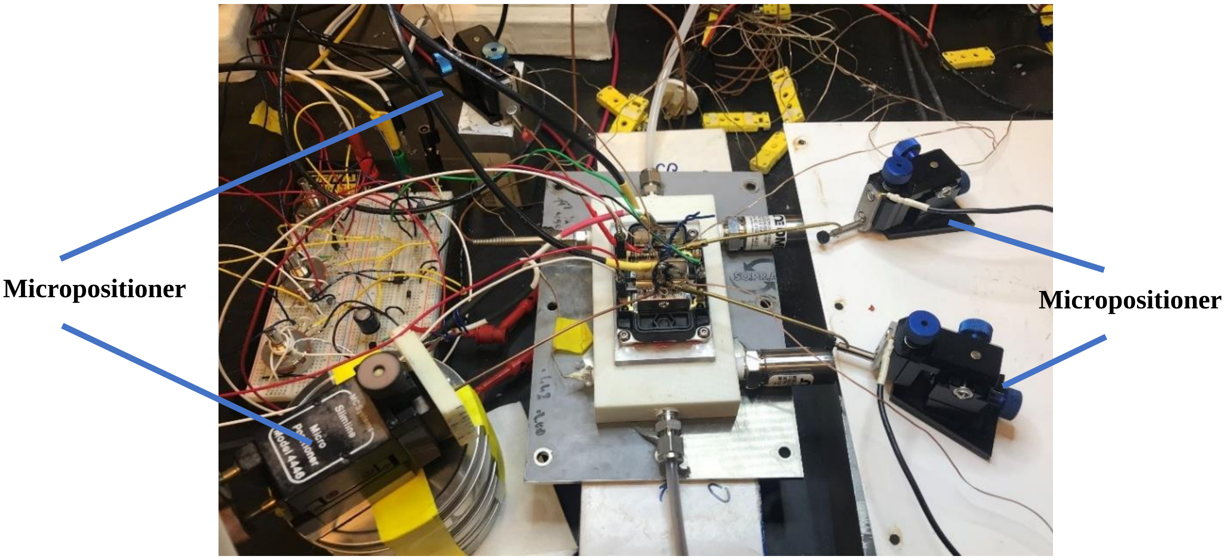

Figure 4.6 Four micropositioners used in test

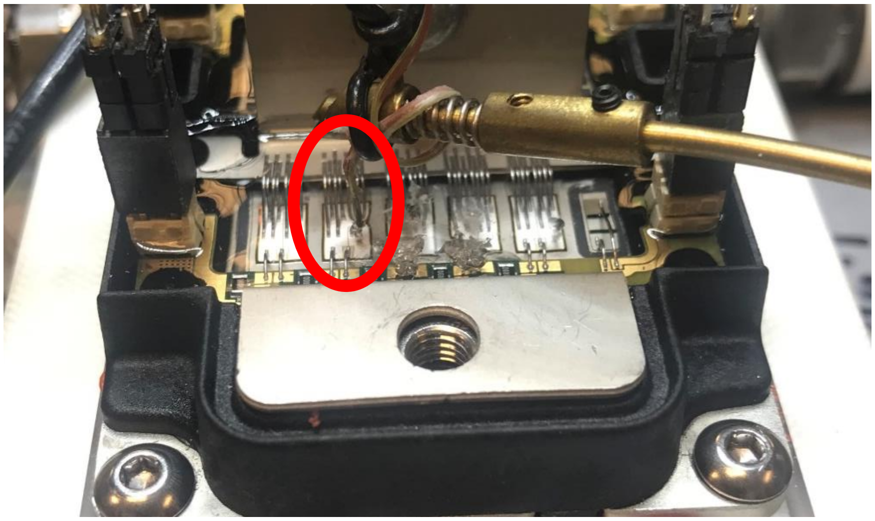

Figure 4.7 Direct contact of thermocouple on the chip

4.2.2 Experimental Validation and Analysis

The test is firstly performed at low flow rate 25ml/min for both coldplates. Different amounts of power dissipation are applied to the module and thermal performance is characterized. The proposed integrated micro-gap mini-channel (IMGMC) cooling and conventional mini-channel (CMC) cooling are tested, using pure water as coolant. Since the boiling temperature of water is 100˚C at 1 atmosphere pressure, the cooling system operates in single-phase regime when water temperature is lower than 100˚C and in two-phase regime when water temperature is higher than 100˚C. In the actual test condition, considering the position of pressure transducer and tolerance of measurement, the two-phase regime starts at the point when Toutlet is an approximate constant and close to 100˚C. The value of Toutlet at flow rate 25ml/min of IMGMC vs CMC is shown as a function of power dissipation in Figure 4.8(a). At the beginning, the linear increase parts of both curves represent single-phase regime. IMGMC starts two-phase regime at 128W of power dissipation, vs CMC at 162W. An early start of two-phase cooling in IMGMC proves that it has a better heat transfer coefficient than CMC due to the larger effective flow area introduced by micro-gap. The coolant pressure drop between the inlet and outlet is shown in Figure 4.8(b). The curve of IMGMC shows that the pressure drop has a linear growth in the single-phase regime (first two measured points around 90W), then a significant increase occurs when two-phase regime starts, then the increase of pressure drop is slow above 150W. This slow increase indicates that the entire system operates in a stable mode in the two-phase regime. The curve of CMC in Figure 4.8(b) shows that the pressure drop keeps increasing rapidly even after two-phase regime starts, which means that two-phase regime is not stable for this cooling system.

Two important parameters in thermal performance of power module are junction temperature T_j and thermal resistance from junction to coolant at inlet $R_{th(j-in)}$. As mentioned above, multiple thermocouples are used to measure the values of T_j, and the temperatures shown in the curves of Fig.13 are average values from the thermocouples. As mentioned in previous section, a non-uniform T_j distribution exists in the system due to unbalances in current distribution and in cooling conditions. Therefore, test is stopped for safety reasons if any individual T_j exceeds 160 ˚C with consideration of the uncertainty in the system.

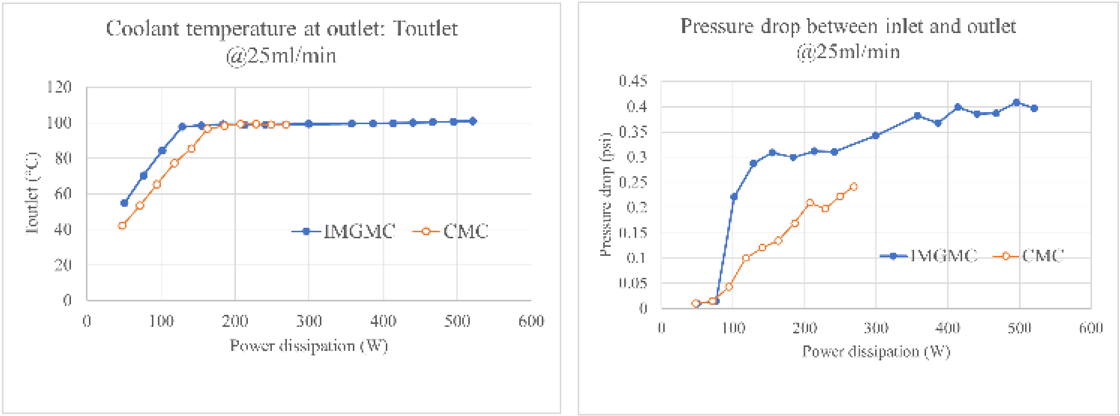

Figure 4.8 (a) Toutlet @25ml/min, (b) Pressure drop @25ml/min.

From Figure 4.9 (a), the maximum power dissipation is 520.7W for IMGMC vs 268.6W for CMC, with a difference of 252.1W, which is approximately a doubling of the cooling capability. Comparing T_j between IMGMC and CMC at similar power dissipation, there is a minor difference in the single-phase regime, which increases rapidly in the two-phase regime as power dissipation increases. The maximum difference of T_j is 46.9 ˚C at the CMC maximum power of 268.6W.

The thermal resistance from junction to coolant at inlet $R_{th(j-in)}$ is calculated as (4.1).

$$R_{th(j-in)} = (T_j - T_{in})/P_{diss} \tag{4.1}$$

Figure 4.8 (b) shows for the IMGMC case an approximately constant thermal resistance during single-phase regime below 100˚C. When two-phase regime occurs above 100˚C, a much larger amount of heat is removed and the $R_{th(j-in)}$ drops rapidly. The thermal resistance then saturates at a low value until dryout occurs at a power dissipation of 520W. The values of $R_{th(j-in)}$ at power dissipation of 268.6W, the last test point of

CMC, are 0.489 ˚C/W for CMC vs 0.314 ˚C/W for IMGMC, with a 36.7% reduction. The percentage reduction approximately matches the calculated value 38.1% in previous section from Tables I and II. As power dissipation increases beyond the max value for CMC, the value of IMGMC $R_{th(j-in)}$ keeps dropping to a value of 0.225 ˚C/W, which is 54% reduction compared with that of CMC at maximum power dissipation. The results clearly show that the proposed IMGMC has a superior thermal performance.

The thermal performance of proposed IMGMC is investigated at different flow rates of 25ml/min, 50ml/min, and 75ml/min. From the plots of T_{outlet} shown in Figure 4.10, IMGMC enters two-phase regime at 128W@25ml/min, 271W@50ml/min, and 390W@75ml/min, respectively. Higher flow rate requires more heat flux to initiate phase transition. At high power dissipation, the value of T_{outlet} is a little higher than 100 ˚C due to high pressure (larger than 1 atmosphere) in the coldplate causing an increase in the actual boiling point of water. Note that in the two-phase regime the outlet temperature is basically the same for the different flow rates, as expected.

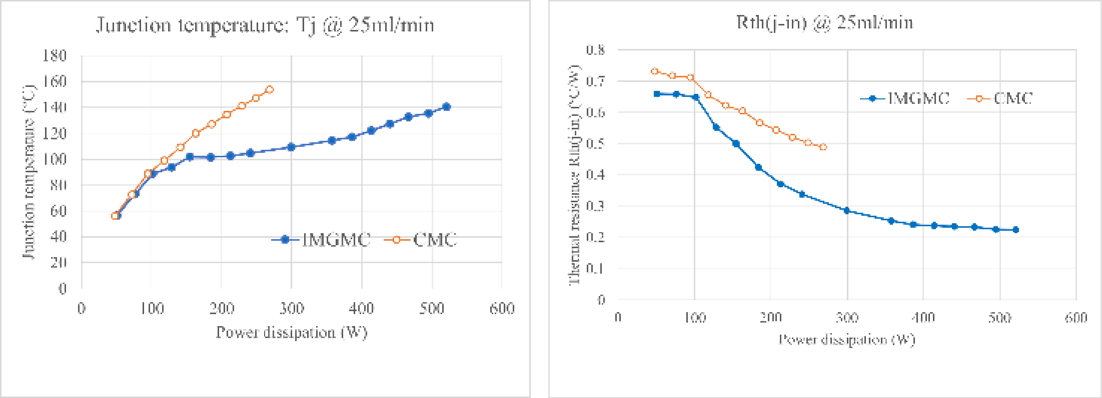

Figure 4.9 (a) $\boldsymbol{T_j}$@25ml/min, (b) $\boldsymbol{R_{th(j-in)}}$@25ml/min.

Junction temperature T_j and thermal resistance $R_{th(j-in)}$ of IMGMC at different flow rates are shown in Figure 4.11 and Figure 4.12 respectively. Due to the increased

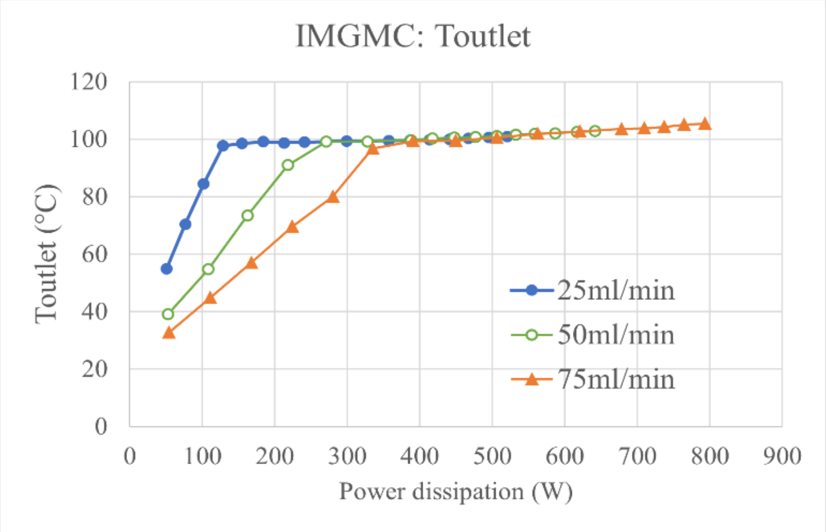

Figure 4.10 Coolant outlet temperature Toutlet of IMGMC at different flow rates.

amount of coolant at higher flow rate, more heat is absorbed by water. According to Figure 4.11, the maximum power dissipation at each flow rate is 520.7W @ 25ml/min, 641.7W @ 50ml/min and 793.2W @ 75ml/min respectively. The difference between them is 121W, 23.2% increase from 25ml/min to 50ml/min, and 272.5W, 52.3% increase from 25ml/min to 75ml/min. An increase in flow rate by 25ml/min, which is very small compared to typical flow rates in single phase coldplates, results in a significant increase in power dissipation, showing better thermal capability. Considering that the required flow rate of current commercial single phase coldplates is up to 8-24 L/min [66,67], several hundred times reduction of flow rate is realized in proposed IMGMC cooling, which can dramatically reduce the size and weight of the entire cooling system.

.As shown in Figure 4.12, the values of $R_{th(j-in)}$ for each flow rate at maximum power dissipation are 0.225 ˚C/W @ 25ml/min, 0.184 ˚C/W @ 50ml/min, and 0.149 ˚C/W @ 75ml/min. The reduction is 18.2% from 25ml/min to 50ml/min, and 33.8% from

25ml/min to 75ml/min, which reflects the improvement of thermal performance obtained by increasing flow rate.

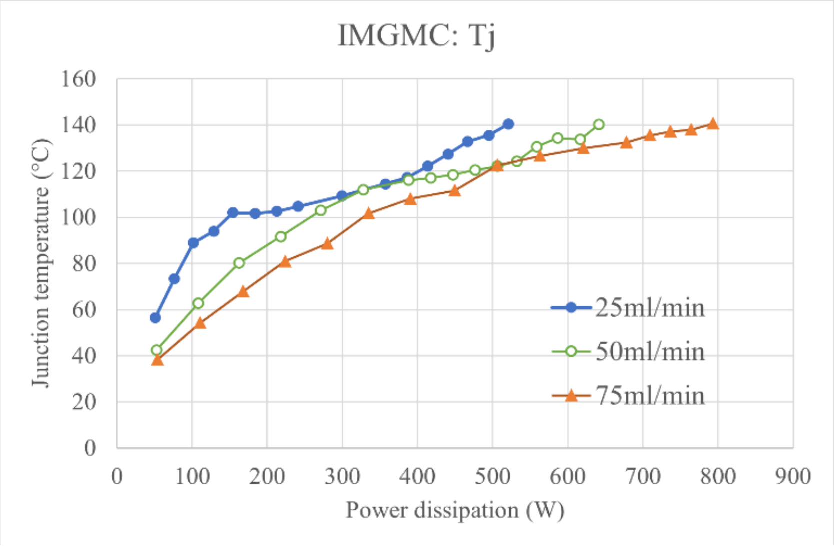

Figure 4.11 Junction temperature $\boldsymbol{T_j}$ of IMGMC at different flow rates

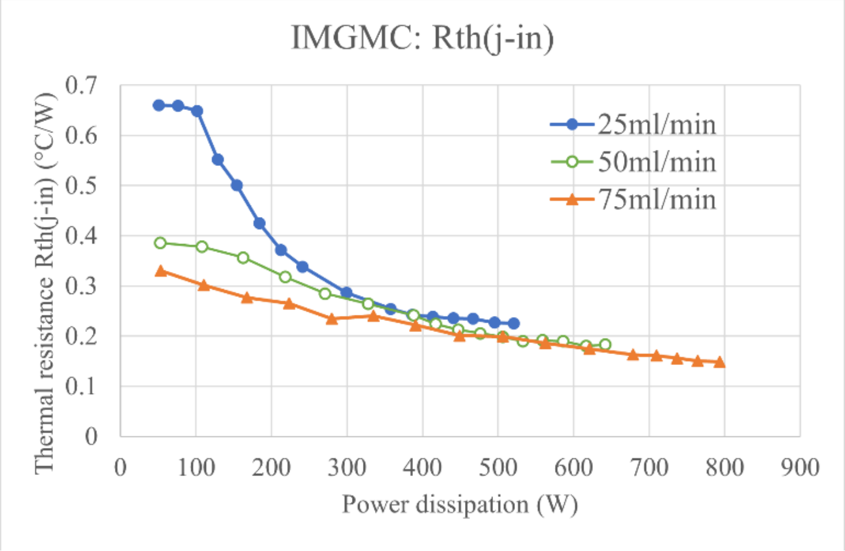

Figure 4.12 Thermal resistance $\boldsymbol{R_{th(j-in)}}$of IMGMC at different flow rates.

The pressure drop is strongly related with stability and reliability of cooling system. A high pressure drop occurs when the coolants flow in a small channel with a high velocity. Therefore, the thermal solutions at small size have higher pressure drop, such as jet impingement on the order of 10.2 psi [68], and up to 11.6 - 26.1 psi with spray cooling [69,70]. The range of pressure drop in a commercial coldplate designed for Wolfspeed^{TM} SiC power module is 2.2 - 14.5 psi as flow rate from 9 to 24_L/min [67].

Table 4.3 Maximum pressure drop at different flow rates

Flow rate	25ml/min	50min/min	75ml/min
Pressure drop inlet to outlet	0.41 psi	0.48 psi	0.57 psi
Pressure drop inlet to atmosphere	2.2 psi	3.5 psi	5.0 psi

In the Table 4.3, the maximum pressure drops at different flow rates are shown. In the first row, the pressure drop from inlet to outlet is small due to the low flow rate compared with conventional single-phase cooling. To fairly compare with other cooling solutions in a single-phase regime, the pressure variation resulted from air expansion during phase transition is considered as shown in 2nd row of Table 4.3. The maximum pressure drops from inlet to atmosphere of proposed cooling solution are 2.2 psi @ 25ml/min, 3.5 psi @50ml/min, and_5.0 psi@75ml/min respectively. It’s similar to the commercial coldplate and better than other cooling solutions for power electronics mentioned previously.

The transparent back plate is designed to allow the visualization of coolant flow in the mini-channels during tests as explained in the previous section. As shown in Fig.17, the flow boiling in proposed IMGMC is recorded by high-speed camera. The test conditions are 25ml/min flow rate and 350W power dissipation, where the system starts a stable two-phase cooling regime. The pictures are shown in time sequence from (a) to (d). There are three walls and two channels as clearly shown in Figure 4.13(a). The coolant flow direction is from right to left. In Figure 4.13 (a), a small vapor slug and a few bubbles are generated in the upper channel at time t_1. As more water evaporates, the vapor slug is enlarged at time t_2 as shown in Figure 4.13 (b). Due to the existence of the micro-gap in the wall, there are paths for vapor expansion across the wall indicated by arrows in Figure 4.13 (c). This provides a mechanism to relieve the vapor slug at time t_3: the micro-gap provides a thin liquid film along the top surface of walls via capillary flow until rewetting flow in channel occurs at time t4, as shown in Figure 4.13 (d), which avoids the local dryout.

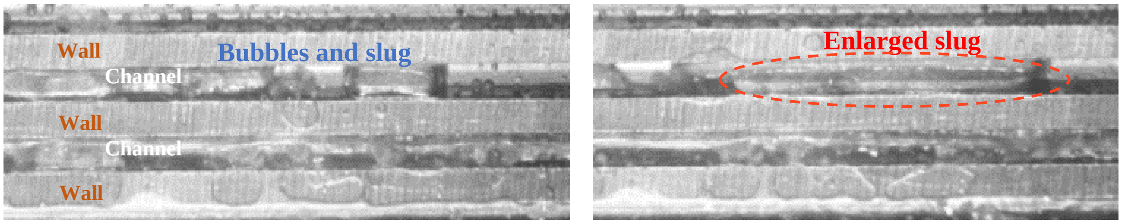

(a) Bubbles and small slug at time t_1

(b) Enlarged slug at time t_2

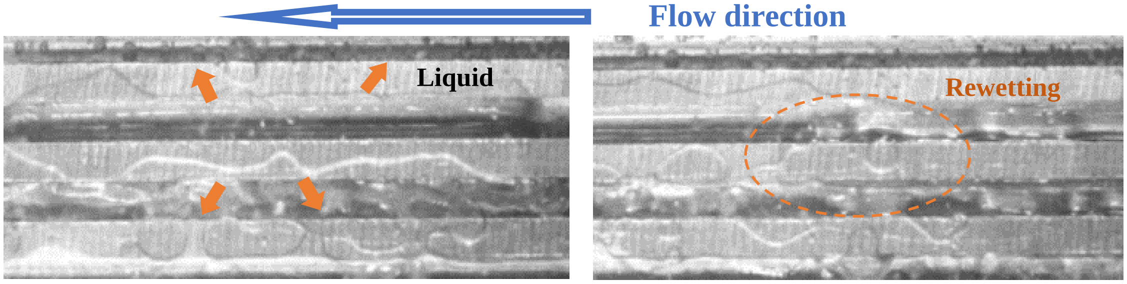

(c) Vapor expansion at time t_3

(d) Liquid film in micro-gap at time t_4

Figure 4.13 Flow boiling in IMGMC by high-speed camera @ 25ml/min, 350W

4.2.3 Summary

A novel SiC power module with water-based two-phase integrated micro-gap mini-channel (IMGMC) cooling is proposed. The proposed module reduces thermal resistance by removing baseplate and thermal interface material. The introduction of mini-channels with a novel micro-gap structure enhances flow boiling performance and increases maximum power dissipation at the same junction temperature. The demonstration of proposed power module is completed successfully on a commercial Wolfspeed^{TM} SiC power module. The experimental results show that total thermal resistance from junction to coolant at inlet $\boldsymbol{R_{th(j-in)}}$of proposed module is reduced 36.7% vs conventional mini-channel (CMC) cooling, which approximately matches the value from theoretical calculation. Approximately doubling of maximum power dissipation is achieved between IMGMC and CMC at 25ml/min flow rate. The study of IMGMC at different flow rates proves that a minor increase of flow rate enables a significant improvement of IMGMC thermal performance. The pressure drop is similar to the commercial coldplate and better than other cooling solutions for power electronics. The visualization of flow boiling in IMGMC validates the superior performance due to the introduction of micro-gap structure in mini-channels. To further improve the thermal performance of micro-gap mini-channel, optimization studies will be performed, varying parameters such as channel roughness and flow distribution.

CHAPTER 5

EFFECT OF CHANNEL HEIGHT ON TWO-PHASE COOLING IN RECTANGULAR PARALLEL MINI-CHANNELS FOR SIC POWER MODULE

For the flow boiling process in a confined space, the channel shape is a crucial design parameter because it directly affects the bubble dynamics and flow patterns, ultimately the heat transfer performance. Choi et al [71, 72] investigated the flow boiling process in 4 different rectangular single microchannels. They suggested that bubbly flow is dominant at a low aspect ratio (height over width) due to the confinement effect and the thickness of the liquid film in the corners decreases with the aspect ratio. Soupremanien et al [73] studied two single mini-channels flow boiling and showed that the aspect ratio could change the onset of nucleate boiling (ONB) characteristics as a result of decreasing cross-sectional area. Singh et al [74] concluded in their research that the annular flow model is good for predicting square cross-section but poor for large aspect ratio rectangular cross-section microchannels by studying flow boiling in a single rectangular microchannel. Some studies also showed the impact of channel shape on flow boiling performance in parallel mini-channels. Pan et al [75] pointed out that an optimal aspect ratio exits at ~0.99 for the highest critical heat flux (CHF) due to the copious existence of liquid film around the corner, and superheat increases with the aspect ratio. Aydin et al [76] showed that the heat transfer coefficient (HTC) peaks when AR=3.54 in 29 parallel microchannels with the same hydraulic diameter (100 μm).

Nonetheless, most studies focused on single micro/mini-channel. A better understanding of the channel shape impact on flow boiling in parallel mini-channels is much needed for application on a bigger scale. In addition, most studies didn't consider the junction temperature of electronic components when evaluating the performance of different channel designs. Some two-phase regimes could surpass the junction temperature limit. Last, the footprint for the heat sink is generally restricted, i.e., the overall width and length of the cooling plate. Although both the hydraulic diameter and aspect ratio could affect the flow boiling performance, the channel height is the more flexible design parameter in practice as the channel width is a trade-off between maximizing the heat transfer area and machining feasibility.

In this study, flow boiling in 33 parallel mini-channels with the same width (0.5 mm) was studied for SiC power module cooling. The channel height impact on the flow boiling performance was experimentally investigated based on heat transfer measurement and visualization via a high-speed camera. The case/wall temperature of the mini-channels was chosen as the main restraint for the testing. The objective of this study is to better understand the impact of a key design parameter on the flow boiling in mini-channels for electric cooling applications.

5.1 Mini-channel coldplate design and fabrication

As shown in Figure 5.1, the geometry of the mini-channel coldplate is chosen based on the cooling purpose of a SiC power module (Wolfspeed CAB450M12XM3). On the same baseplate area (80mmx53mm), three mini-channels coldplates with various channel height are fabricated, shown in Table 5.1. The channel area is width x length, 33mmx44mm, and the width of each channel is fixed at 0.5mm. The test setup is same as previous test as shown in Figure 3.4 and Figure.3.14.

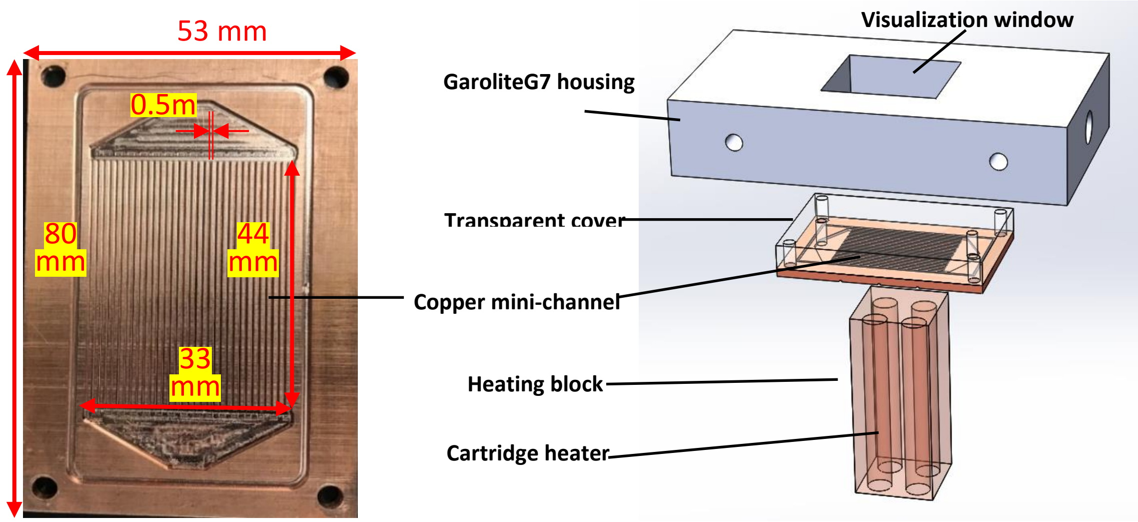

Figure 5.1 Channel size and schematic of the test setup for the mini-channel

Table 5.1 Mini-channel size and geometry

Sample numbers	Channel dimensions Channel width, height, length (mm)	Hydraulic diameters D_h (mm)	Height-to-width ratios H/W	Channel quantities
MC1	0.5 × 0.5 × 44	0.5	1:1	33
MC2	0.5 × 1 × 44	0.67	2:1	33
MC3	0.5 × 1.5 × 44	0.75	3:1	33

5.2 Data reduction

In the thermal management of SiC power module, case temperature, thermal resistance of coldplate, and pressure drop of coolant between the inlet and outlet are essential parameters to be investigated, which exhibit the overall thermal performance of the coldplate. The maximum case temperature of ~150 °C is chosen in the test to simulate actual operating conditions to avoid chip failure [43-45]. As shown in Figure 3.1, there are multiple chips integrated in the power module, that is, the power module fails if any of the chips is overheated. Therefore, the test is set to terminate when any of Tc is up to ~150 °C. The thermal resistance of coldplate R_{th} is calculated by (5.1):

$$R_{th} = [T_{C\_avg} - (T_{in} + T_{out})/2] / Q_h \tag{5.1}$$

Where T_{C_avg} is the average value of three case temperatures in the test, T_{in} is the inlet temperature of the fluid, T_{out} is the outlet temperature of the fluid, and Q_h is heating power, which is derived based on the input voltage (V_{in}) and current (I_{in}).

$$Q_h = V_{in} \cdot I_{in} \tag{5.2}$$

Exit vapor quality, and effective heat transfer coefficient are used to discuss the two-phase cooling performance of mini-channel coldplates.

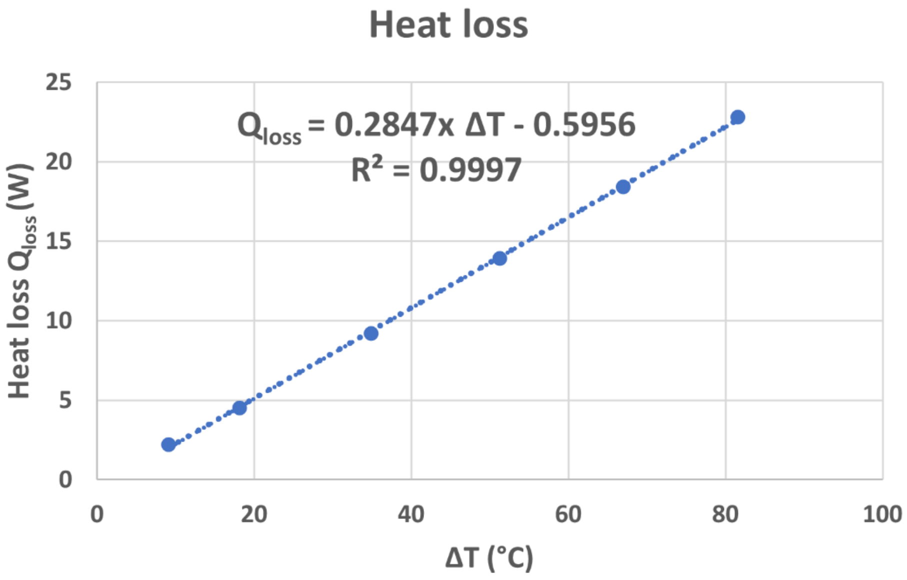

Figure 5.2 Experimental heat loss vs. the temperature difference between the coldplate surface and ambient temperature.

The heat loss Q_{loss} to the environment through natural convection and radiation during the experiments is calibrated by the temperature difference between the coldplate surface and ambient temperature (Figure 5.2). The coldplate surface temperature is measured when the heater is on, and the test setup reaches a steady state without working fluid in the ambient environment.

The effective heating power $Q_{h,eff}$ is calculated by (5.3),

$$Q_{h,eff} = Q_h - Q_{loss} \tag{5.3}$$

The effective heat flux is achieved by (4),

$$HF_{eff} = \frac{Q_{h,eff}}{A_{channel}} = \frac{Q_{h,eff}}{44mm \times 33mm} \tag{5.4}$$

The exit vapor quality is derived based on the energy balance of the working fluid passing through the test section:

$$x = \frac{Q_{h,eff} - \dot{m} \cdot C_p \cdot (T_{sat,out} - T_{in})}{\dot{m} \cdot H_{fg}} \tag{5.5}$$

Where $Q_{h,eff}$ is effective heating power, $\dot{m}$ is the mass flow rate $C_p$is the specific heat capacity of the fluid, T_{in} is the inlet temperature of the liquid and $T_{sat,out}$ is saturation temperature under outlet pressure, x is the exit vapor quality, H_{fg} is the latent heat of vaporization.

Considering the thermal resistance of the copper substrate, the average wall temperature T_{w_avg} is calculated as:

$$T_{w\_avg} = T_{c\_avg} - \frac{Q_{h,eff} \cdot t}{A_0 \cdot k_s} \tag{5.6}$$

where t is the thickness between the thermocouple to the inner surface of Cu substrate and k_s is the thermal conductivity of the Cu substrate. Therefore, the effective HTC is calculated as:

$$h_{c,eff} = -\frac{Q_{h,eff}}{n(W\cdot L+2H\cdot L\cdot \eta_f)\cdot(T_{w\_avg}-T_{sat,avg})} \tag{5.7}$$

$$\eta_f = \frac{\tanh(m\cdot H)}{m\cdot H} \tag{5.8}$$

$$m = \sqrt{\frac{2h_{c,eff}(L+W_f)}{k_s\cdot W_f\cdot L}} \tag{5.9}$$

where the average saturation temperature $T_{sat,avg}$ refers to the saturation temperature under the average characteristic pressure $\overline{p} = (p_{in} + p_{out})/2$. p_{in} is the inlet pressure and p_{out} is the outlet pressure of the channels. W, L, and H refer to the channel width, length, and height respectively. The channel walls are treated as extended fins. W_f is the channel wall width (fin thickness), η_f is the fin efficiency, and m is the fin parameter.

The uncertainties of all measured variables are estimated based on the specific instructions from instrument manufacture. The uncertainties of the heat flux, local HTC, and exit vapor quality are derived following the standard uncertainty propagation method. The maximum uncertainties of the experimental parameters are listed in Table 5.2.

5.3 Experimental results and discussion

The thermal performances of mini-channels are investigated at four various mass fluxes: 24.8 kg/(m^{2}s), 49.6 kg/(m^{2}s), 74.4 kg/(m^{2}s), and 99.2 kg/(m^{2}s), respectively. The parameters of overall coldplate and two-phase cooling performance are discussed in the next sections.

5.3.1 Average case temperature and thermal resistance

In Figure 5.3, the average case temperatures T_{c_avg} are compared vs. effective heat flux HF_{eff}. The sample MC2 (Channel height = 1mm) shows the best heat transfer capability (the highest heat flux under case temperature limit) in all testing conditions, with 52.4W/cm^2 (Q_h=800W)@ 24.8 kg/(m^{2}s), 62.7W/cm^2 (Q_h=950W)@ 49.6kg/(m^{2}s),

Table 5.2. Uncertainty of variables in the test

Parameters	Measurement/Equation	Uncertainty under test
Ambient temperature	K type thermocouple	± 1 ˚C
Input voltage V_{in}	B&K Precision XLN10014	± 0.08%
Input current I_{in}	B&K Precision XLN10014	± 0.08%
Pressure	Omega PX359-100A5V	± 0.25%
Pressure drop	$\Delta p = \sqrt{\Delta p_{in}^2 + \Delta p_{out}^2}$	± (0.0073–0.011) psi
Flow rate/ mass flux	OMEGA FLR1600	± 2%
Effective heat flux	$\Delta Q_{h,eff} = \pm \sqrt{(\frac{\Delta V_{in} \cdot I_{in}}{A_0})^2 + (\frac{V_{in} \cdot \Delta I_{in}}{A_0})^2 + (\frac{\Delta Q_{loss}}{A_0})^2 + (\frac{Q_{h,eff} \cdot \Delta A}{A_0}}$	± (<5%)
Wall temperature	$\Delta T_{w\_avg} = \pm \sqrt{(\Delta \bar{T}_h)^2 + (\frac{Q_{h,eff} \cdot t}{k_s})^2 + (\frac{Q_{h,eff} \cdot \Delta t}{k_s})^2 + (\frac{Q_{h,eff} \cdot t}{k_s^2} \Delta k}$ Where $\Delta \bar{T}_h = \pm 1K$	± 1.5K
Effective HTC	$\Delta h_{c,eff} = \frac{1}{n} \sqrt{\left[\frac{\Delta\left(Q_{h,eff} \cdot A_0\right)}{\left(W \cdot L + 2H \cdot L \cdot \eta_f\right) \cdot \left(T_{w\_avg} - T_{sat}\right)}\right]^2 + \left[\frac{\left(Q_{h,eff} \cdot A_0\right) \cdot \Delta\left(W \cdot L + 2H \cdot L \cdot \eta_f\right)}{\left(W \cdot L + 2H \cdot L \cdot \eta_f\right)^2 \cdot \left(T_{w\_avg} - T_{sat}\right)}\right]^2 + \left[\frac{(Q_{h,eff} \cdot A_0) \cdot \Delta(T_{w\_avg} - T_{sat})}{(W \cdot L + 2H \cdot L \cdot \eta_f) \cdot (T_{w\_avg} - T_{sat})^2}\right]^2}$	< 40%

62.7W/cm^2 (Q_h=950W)@ 74.4kg/(m^{2}s), and c (Q_h=1050W)@ 99.2kg/(m^{2}s) respectively. MC2 has the lowest values of T_{c_avg} at the same heat flux compared the other samples, which indicates a low thermal resistance according to the equation (5.1). The performance of sample MC1 (Channel height = 0.5mm) is not consistent with variation of mass flux. At a low mass flux 24.8 kg/(m^2s), MC1 is stopped at a low heat flux (~25W/cm^2) due to local dryout. However, at the higher mass flux 49.6kg/(m^2s), 74.4kg/(m^2s), 99.2kg/(m^2s), MC1 shows a larger heat flux cooling capability than MC3 (Channel height = 1.5mm). Onset of nucleate boiling (ONB) is labeled in the Figure 5. At all mass fluxes, MC1 with shallow channels occurs ONB at a lowest heat flux, MC3 with deeper channels has ONB at a highest heat flux, and ONB of MC2 is between MC1 and MC3. At a low mass flux 24.8 kg/(m^2s), MC1 starts boiling around T_{c_avg} = 100℃, and MC3 is around T_{c_avg} = 115℃. At a high mass flux 99.2 kg/(m^2s), ONB of MC1 is around T_{c_avg} = 98℃ vs. MC3 around T_{c_avg} = 141℃. It shows that deeper channels have subcooled liquid on top, needs higher superheat for ONB.

Figure 5.4 shows the variation of thermal resistance vs. effective heat flux at various mass fluxes. For all samples, the values of thermal resistance decrease as mass flux increase. In four mass fluxes, MC2 is always the one with the lowest thermal resistance. MC3 has a lower thermal resistance than MC1 in single-phase regime, and above MC1 in two-phase regime. At lower mass fluxes 24.8 kg/(m^2s) and 49.6 kg/(m^2s), the thermal resistance drops quickly and begins to slow down after entering the two-phase regime, which makes a large difference between the minimum and maximum R_{th} values, especially for MC1. For example, at mass flux 24.8 kg/(m^2s) from maximum to minimum the thermal resistance is reduced 75.6% for MC1, 68.8% for MC2, and 34.9% for MC3. At a high mass flux, the decrease rate in thermal resistance is smaller for all samples. At mass flux 99.2 kg/(m^2s) the thermal resistance is reduced 56.2% for MC1, 21.8% for MC2, and 22.7% for MC3.

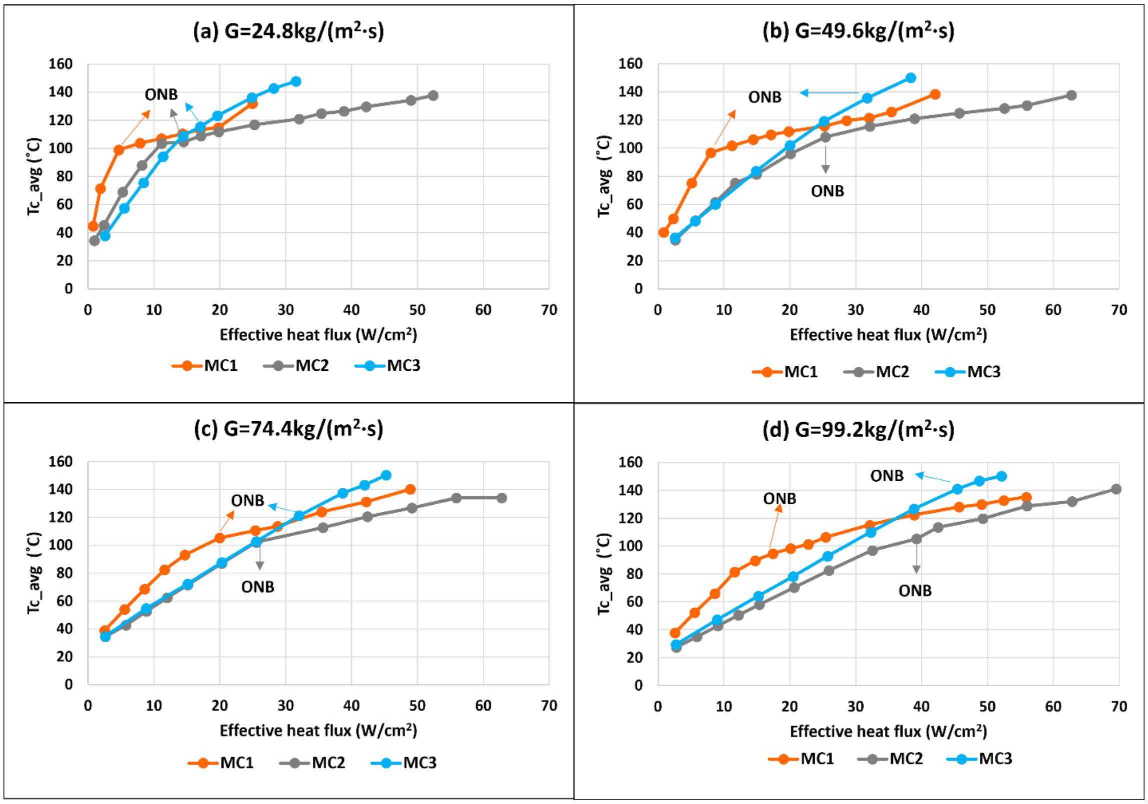

Figure 5.3 Average case temperature vs. effective heat flux at various mass fluxes (a)G=24.8 kg/(m^{2}s), (b) G= 49.6 kg/(m^{2}s), (c) G= 74.4 kg/(m^{2}s), and (d) G= 99.2 kg/(m^{2}s)

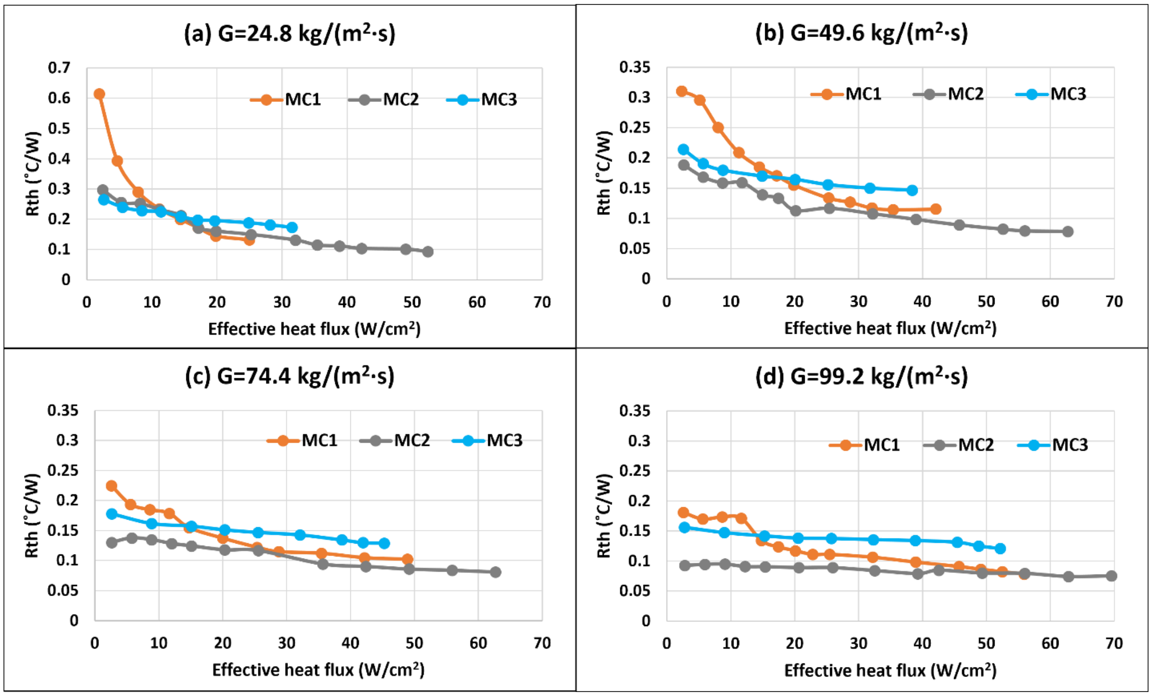

Figure 5.4 Thermal resistance vs. effective heat flux at various mass fluxes (a)G=24.8 kg/(m^{2}s), (b) G= 49.6 kg/(m^{2}s), (c) G= 74.4 kg/(m^{2}s), and (d) G= 99.2 kg/(m^{2}s)

The difference of minimum thermal resistance between MC1 and MC2 becomes smaller as the increase of mass flux, such as MC1, 0.079 ℃/W and MC2, 0.074℃/W at mass flux 99.2 kg/(m^2s). However, MC1 doesn't work at a higher heat flux due to case temperature limitation.

5.3.2 Pressure drop and pumping power

Pressure drop is related with cooling system reliability and cost. A low pressure drop is desired in power module cooling applications [77]. As shown in Figure 5.5, MC1 with smallest channel height and hydraulic diameter shows the highest pressure drop at various heat flux, which is ~ 3 times of MC2 at the same heat flux. The data show the pressure drop of MC3 with largest channel height and hydraulic diameter is lowest at the same heat flux. It means the effect of channel height and hydraulic diameter on pressure drop is not neglected, especially for smaller height. The pressure drop of MC1 and MC2 increase quickly, which means more water is evaporated. On the contrary, the increase of MC3 is slow, which means single-phase cooling dominates. Compared the maximum value of pressure drop between MC2 and MC1, MC2 has a smaller maximum pressure drop than MC1, even working on a larger effective heat flux.

The pumping power is expected being small, to reduce the size and weight of pump and entire cooling system. It is calculated by pressure drop times volumetric flow rate, shown in Figure 5.5, and certainly the pumping power grows as mass flux increases. M1, M2 and M3 have different cross section area. When the comparison is made under the same mass flux, different volumetric flow rates are required for each sample, from low to high, M1<M2<M3 Therefore, at a low pressure drop (single-phase regime and the beginning of two-phase regime), the flow rate dominates the pumping power, MC3 has the largest

pumping power. With the rapid increase in pressure drop, the pumping power of MC1 and MC2 exceeds MC3. In two-phase regime, due to the lower proportion of water, the pumping power of MC1 is larger than MC2 in most cases.

Above of all, MC2 has the best overall thermal performance with low case temperature and thermal resistance. Working on a high heat flux, MC2 has a smaller pressure drop and pumping power than MC1 in most cases. The thermal resistance of MC1 is comparable with MC2 at 99.2kg/(m^{2}s), but the price is a dramatically high pressure drop and pumping power. The overall performance of MC3 is worst.

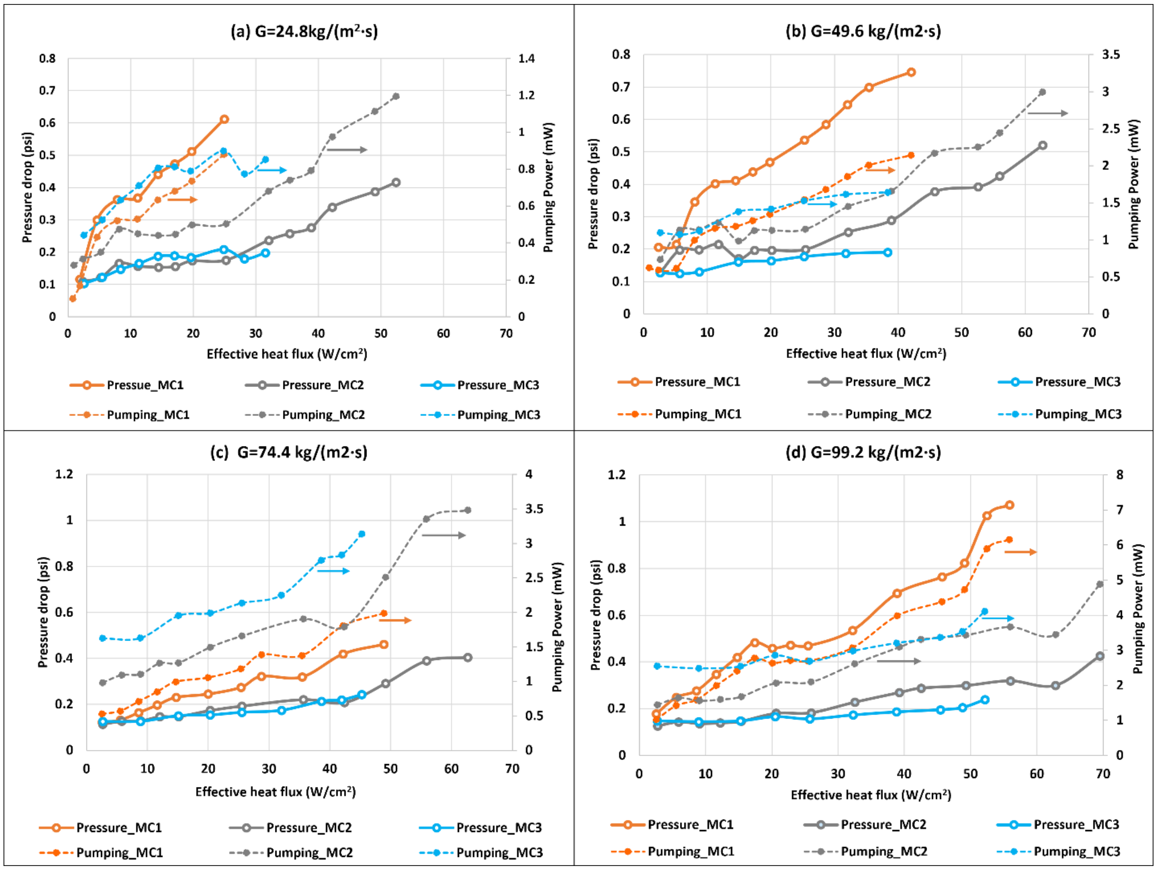

Figure 5.5 Pressure drop and pumping power vs. effective heat flux at various mass fluxes (a)G=24.8 kg/(m2s), (b) G= 49.6 kg/(m2s), (c) G= 74.4 kg/(m2s), and (d) G= 99.2 kg/(m2s)

5.3.3 Maximum vapor quality

Vapor quality is an important parameter to indicate the status of two-phase cooling. For MC1, MC2 and MC3, Figure 5.6 shows the maximum exit vapor quality as a function of mass flux of different mini-channel under the case temperature limit. The exit vapor quality is reversely proportional to mass flux. The values of vapor quality drop quickly as the mass flux increases. From 24.8 kg/(m^2s) to 99.2 kg/(m^2s), the variation of vapor qualities of MC1, MC2, and MC3 is 0.7 to 0.3, 0.69 to 0.12, and 0.18 to 0 respectively. It proves the channel height has a significant effect on vapor quality at the same channel density. An interesting phenomenon is observed that the maximum of heat flux under the case temperature limit is achieved for MC2 at vapor quality equal to 0.12. It indicates that increasing vapor quality alone is not enough to improve the overall thermal performance of power module.

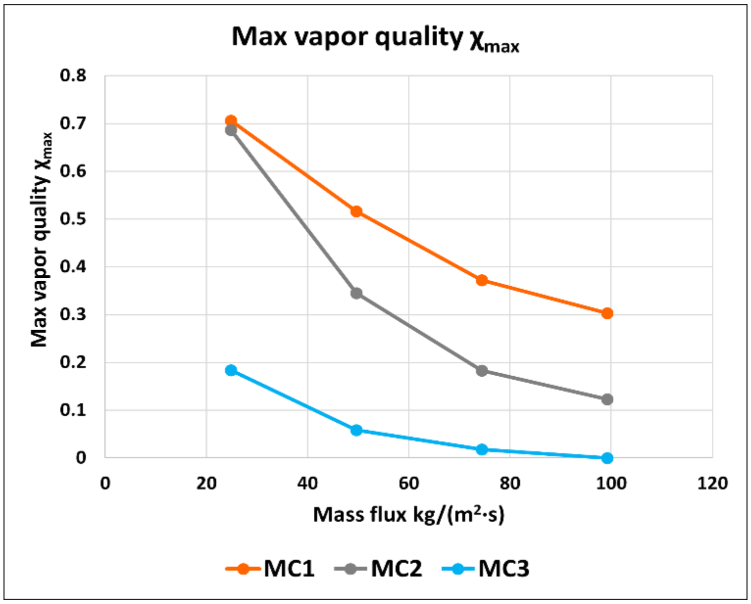

Figure 5.6 Maximum exit vapor quality as a function of mass flux of different mini-channel under the case temperature limit

5.3.4 Two-phase heat transfer

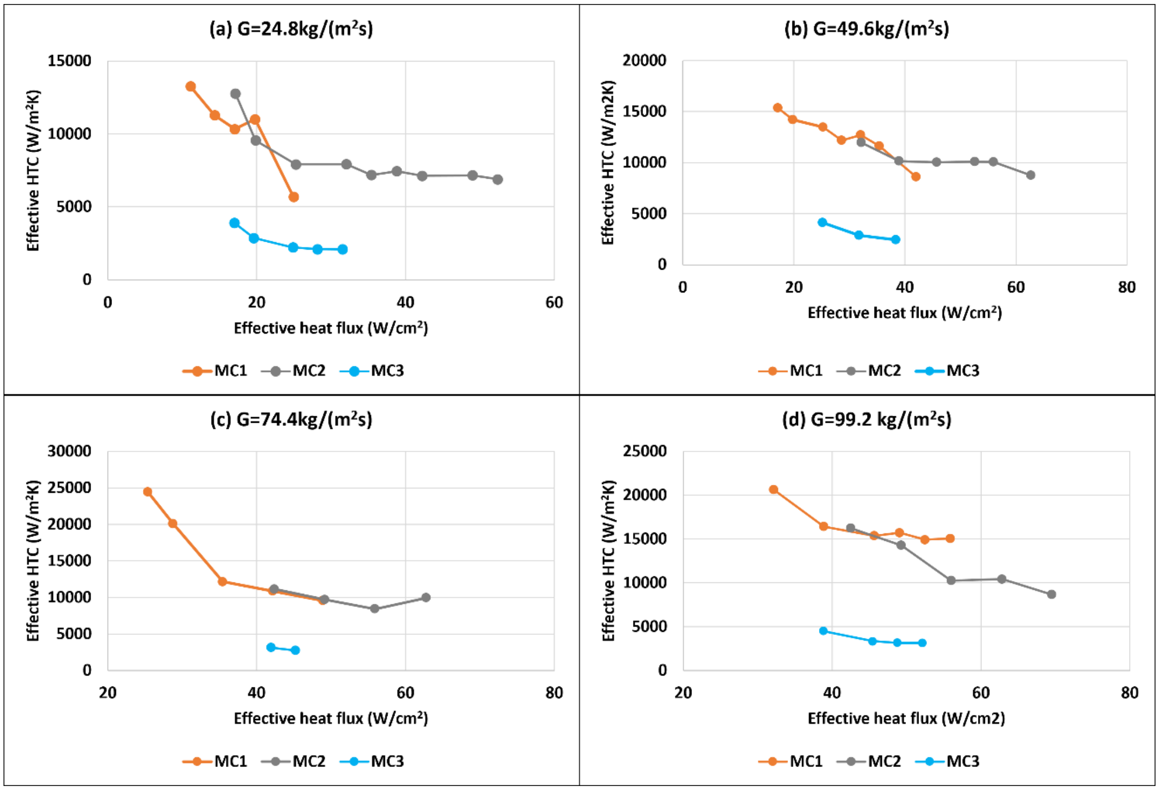

Figure 5.7 Comparison of effective heat transfer coefficients of different mini-channels at various mass fluxes (a)G=24.8 kg/(m^2s), (b) G= 49.6 kg/(m^2s), (c) G= 74.4 kg/(m^2s), and (d) G= 99.2 kg/(m^2s)

Figure 5.7 shows the comparison of effective heat transfer coefficients (HTC) in two-phase regions of three different mini-channels at various mass fluxes. First, the HTC values decrease steadily as the heat flux increases for all mini-channels at all mass fluxes. MC1 and MC2 have close HTC values in all mass fluxes, ranging from 10~20 kW/(m^2K). The difference is that MC1 operated at a lower heat flux until it reached the temperature limit, while MC2 achieved a similar two-phase heat transfer at a higher heat flux. For example, MC1 reached the temperature limit under the heat flux of 48 W/cm^2 with an effective HTC of ~10 kW/m^2K, while MC2 achieved about 63 W/cm^2 heat dissipation with the same HTC. This means that MC1 reached the two-phase region earlier than MC2, which agrees with the ONB differences between MC1 and MC2 in Figure 5.3. Therefore, for parallel mini-channels with a width of 0.5mm particularly, increasing the channel height from 0.5 mm to 1 mm can delay the ONB while achieving similar two-phase heat transfer performance. This helps improve heat dissipation capacity under the same temperature limit.

However, a distinctly low HTC below 5 kW/(m^2K) was observed for MC3 as the channel height increased to 1.5 mm, which is close to the single-phase convection HTC range. This also explains the very low vapor quality in MC3 shown in Figure 5.6. In sub--cooled flow boiling, more liquid occupies the channel space as the channel height increases, causing ONB to occur in higher heat flux (as shown in Figure 5.3). As a result, MC3 requires a higher superheat than the other mini-channels, making the wall temperature of MC3 reach the temperature limit before utilizing the two-phase heat transfer.

5.3.5 Visualization and flow pattern

Visualization via a high-speed camera was carried out to investigate the mechanism of the impact of channel height on flow boiling behavior. Figure 5.8 gives the visualization sequence of flow pattern evolution (time duration 0.07 s) of three mini-channels at the same working condition (G=49.6kg/(m^2s), heating power=500W, effective heat flux=~32W/cm^2). The capture rate of the camera is 1000 frames per second in all cases. The observed area consists of 5 channels in the middle of the outlet regions of the mini-channel, which are labeled as channel #1 ~ channel #5.

Figure 5.8(a) shows the flow evolution in MC1. First, many nucleation sites (circled in red dashed lines at 0.004 s) occurred quickly both in the channels and the gap between the channel and visualization window. This is because the channel walls have a close temperature to the channel bottom surfaces when the channel heights are low. As the evaporation and boiling proceeded, the liquid slug and film retreated as shown in Figure

10(a) from 0.004-0.040 s. Local dryout occurred and liquid islands (circled in blue dashed lines) formed at 0.050 s. After the liquid replenishment and re-distribution at 0.070 s, there are still considerable vapor slugs, which indicates that most of the liquid was saturated from the heating.

The typical bubbly-annular flow was observed in MC2, as shown in Figure 5.8(b). As the channel height increases, unlike MC1, the nucleation mostly occurred at the bottom surface or the corner of the channel sidewalls at 0.000 s because they have higher temperatures compared with the top area of the channel walls. The bubble observed in channel #1 departed from the surface then expanded drastically and finally formed liquid films on the sidewalls (0-0.020 s). This was followed by a similar process in channel #5 as the bubble slug expanded and the liquid film formed, while channels #2-#4 remained still during this period. It suggests an early stage of bubbly-annular flow that the flow boiling hasn't been fully utilized. As the heat transfer data at the mass flux of 49.6 kg/(m^2s) shows, MC2 later reached ~63 W/cm^2 at the wall temperature limit. Film evaporation was observed as the liquid film on the sidewalls shrunk from 0.020-0.070 s.

MC3 showed a completely different flow pattern compared with MC2 and MC1, as Figure 5.8(c) shows. First, no nucleation site was observed. Although there are some vapor slugs on the top of the channel, it does not show any evaporation behavior during the whole period. From 0.040 s to 0.070 s, the liquid film observed on the sidewalls remained the same. This indicates little phase change and most of the heat transfer still relies on the single-phase convection on the bottom of the channel where the subcooled liquid flow occupies. Based on the heat transfer data, the exit vapor quality at this working condition for MC3 is extremely low with a value of 0.024, compared with 0.107 in MC2, and 0.360 in MC1.

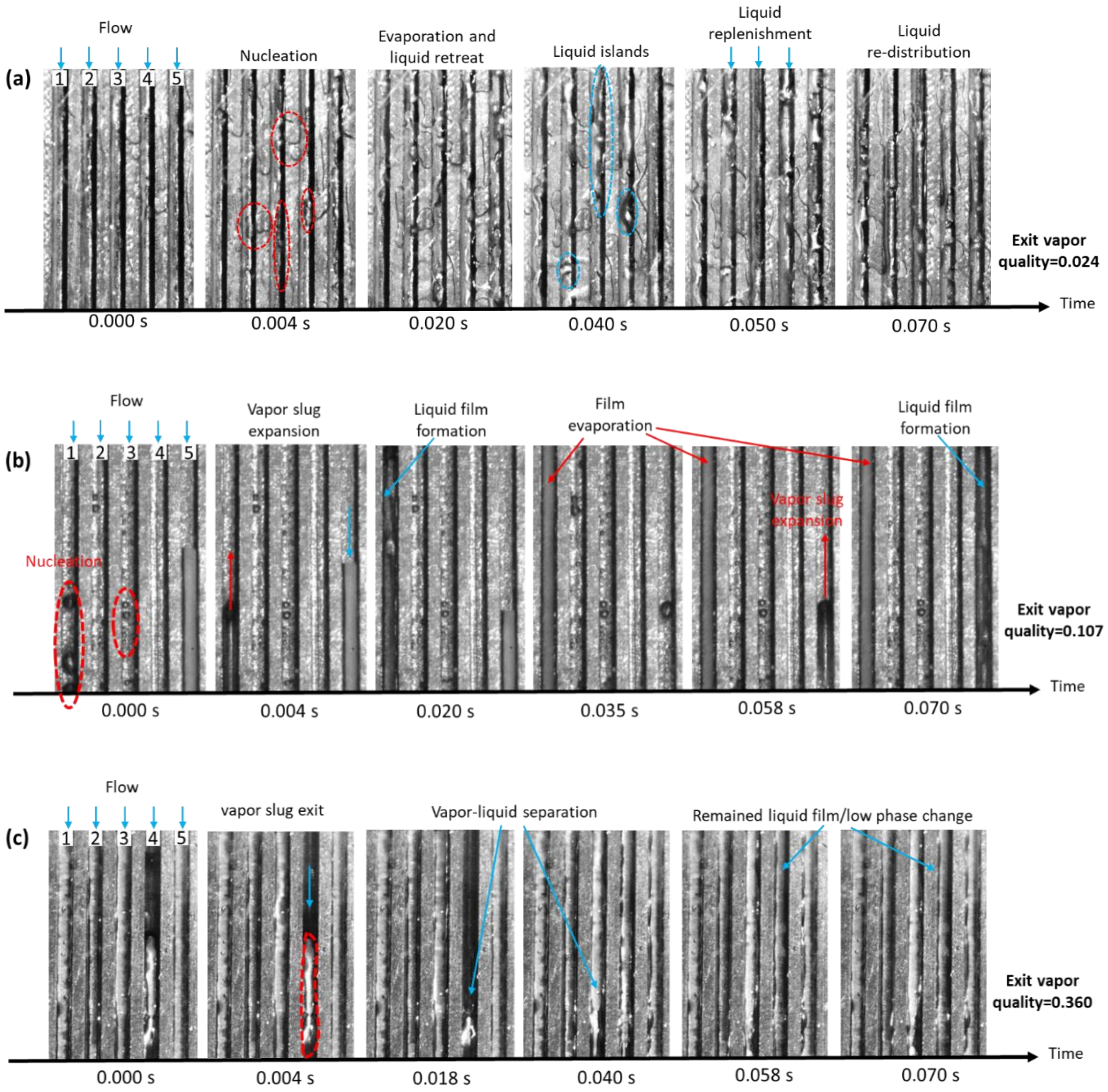

Figure 5.8 The sequence of flow pattern evolution in mini-channels via high-speed camera at the mass flux of 49.6 kg/(m^2s) and total heating power of 500 W (a) MC1 (b) MC2, and (c) MC3

Based on the heat transfer data and visualization analysis, the mechanism of the channel height impact on the flow boiling is demonstrated in Figure 5.9. The channels not only impact the bubble dynamics due to the confinement effect, but it also plays an important role in nucleation and evaporation as the thermal boundary. First, when the channel height is low, less liquid occupies the channel and the walls have a closer temperature to the bottom surface. This enables nucleations to more likely occur at both the bottom and top of the walls and leads to quick local dryout at low heat flux. However, when the channel height increases and more subcooled liquid stores in the channel, the nucleations are more likely to occur at the bottom surface as it has a higher temperature. By increasing the channel height, the larger cross-section area and different wall temperature profiles enable a bubbly-annular flow to fully develop, as shown in Figure 5.8(b).

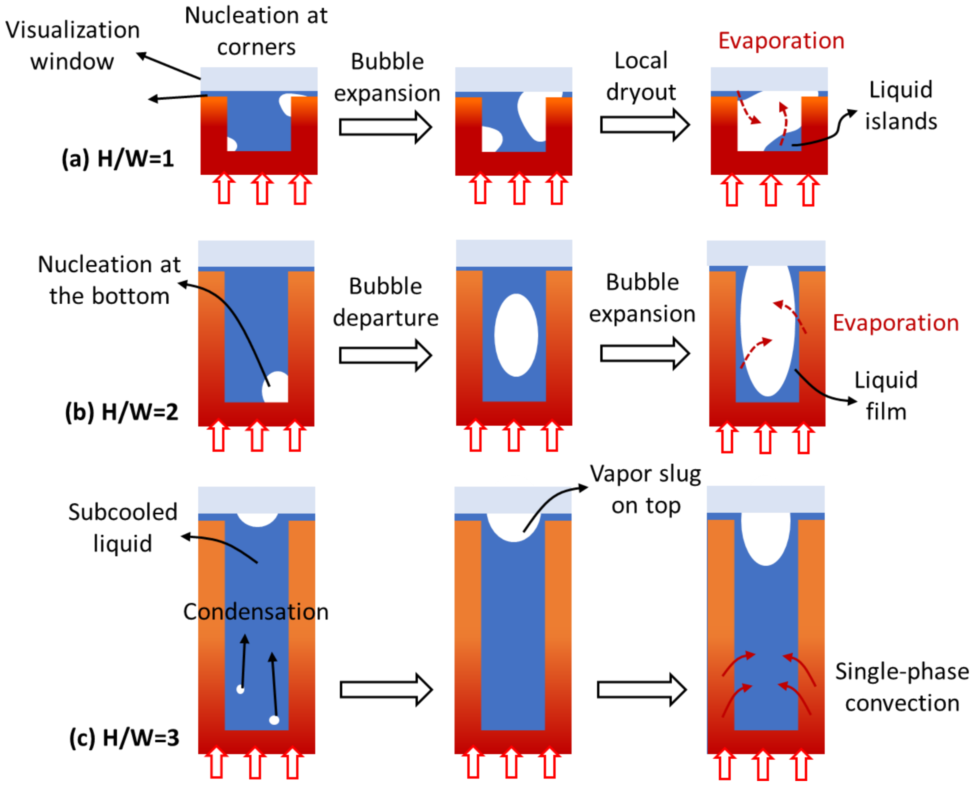

Figure 5.9 Schematic of the channel height impact on the flow pattern evolution

However, if the channel height continues to increase (as shown in Figure 5.9(c)). The majority of the channel area will be occupied by subcooled liquid flow, delaying the ONB to occur under a higher heat flux. The single-phase convection will be the dominant heat transfer mode at the bottom of the channel instead of utilizing efficient two-phase flow boiling. Although large height channels can potentially achieve efficient two-phase heat transfer and high CHF if the heat flux increases, the wall temperature could likely surpass the temperature limit, making this channel shape unfavorable for electronic cooling applications.

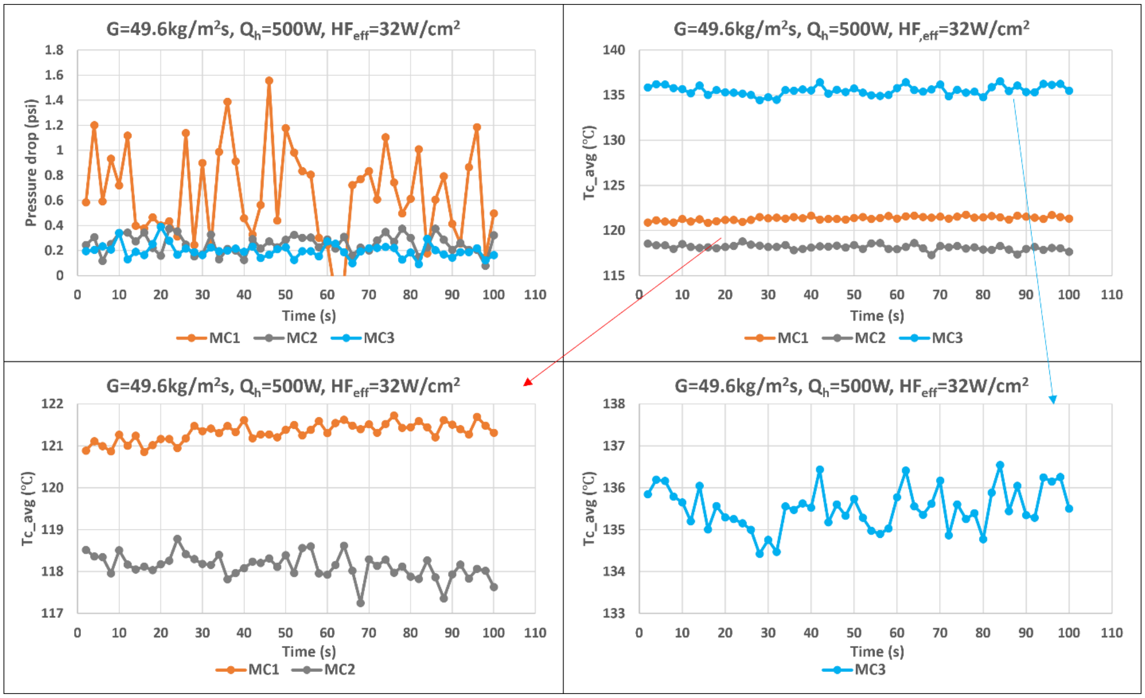

Figure 5.10 Transient case temperature and pressure drop at the mass flux 49.6kg/(m^{2}s) and heating power 500W.

5.3.6 Transient pressure drop and case temperature

The transient pressure drop and case temperature at the mass flux 49.6kg/(m^{2}s), heating power 500W and effective heat flux ~32W/cm^2 are compared for all mini-channels, as shown in Figure 5.10. Due to the high vapor quality, the pressure drop oscillation of MC1 is most significant, and the maximum amplitude is reached 1.6psi. Correspondingly, the pressure drop oscillation is 0.25psi in MC2 and 0.3psi in MC3. On the other hand, due to the worse heat transfer capability, the case temperature with 135℃ and temperature oscillation with 2.1℃ in MC3 are observed, highest among three samples. MC2 has the lowest case temperature with 118℃, and MC1 has the lowest case temperature oscillation with 0.6℃. It indicates the better thermal stability is achieved in a smaller channel height, and vice versa. The oscillation of pressure drop and case temperature in all mini-channels is consistent with previous flow pattern analysis.

5.3.7 Comparison of experimental results and simulation by model

The experimental results are compared with the simulation of two-phase cooling models. In a flow boiling model, besides the geometry of channel and properties of coolant, bubble grow time (τ)/frequency (1/ τ) and liquid film thickness are used to reflect the bubble dynamic and flow pattern. First, Thome model is used to compare the test results. In Thome model [78, 79], three zones, liquid slug dry zone and elongated bubble are defined to occur repeatedly in the channel as Figure 5.11. It is a complete physics-based modelling for slug flow boiling heat transfer within circular micro-channels.

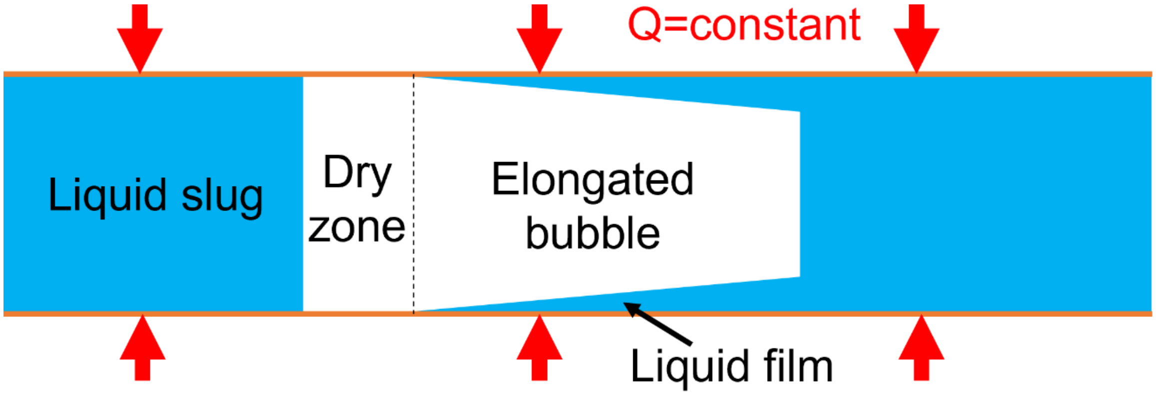

Figure 5.11 Three zone flow boiling model by Thome

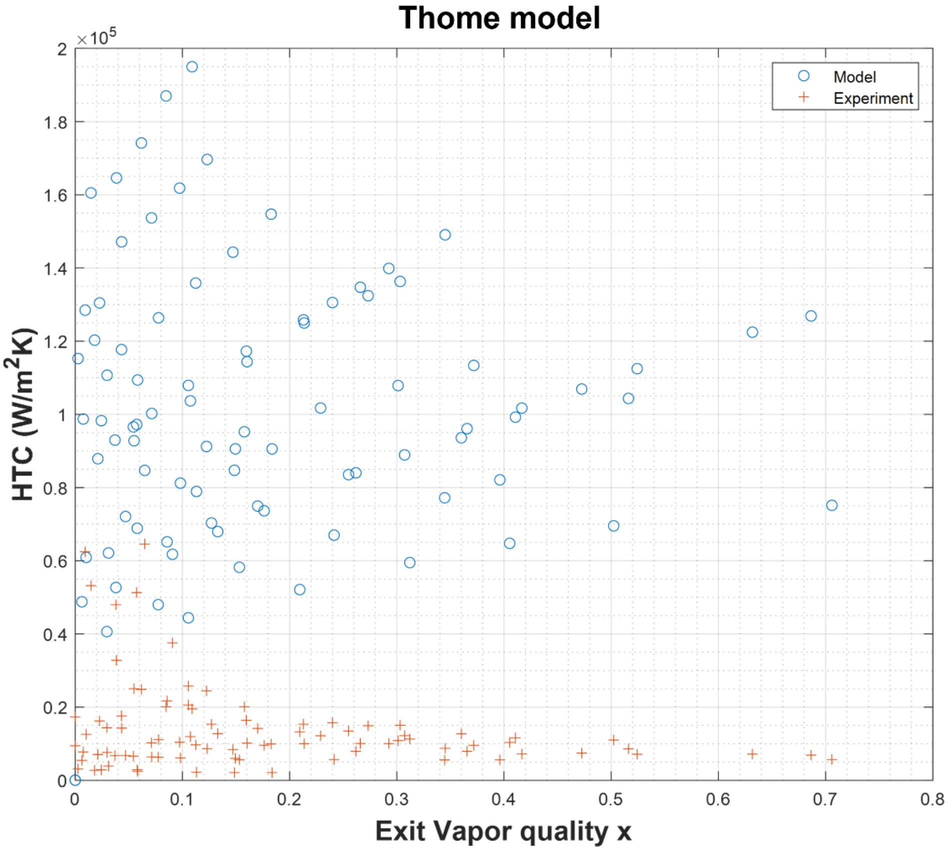

Figure 5.12 HTC vs. Exit vapor quality comparison of Thome model and experiment results

The channel geometry and dimensions, material properties of samples in test are used as input parameters applied in the model. The results compared the model with experiment are shown in Fig 5. 12, they don’t match at all. The main reasons include: 1) the flow pattern is not same, 2) subcooling is not considered in Thome model, 3) the heat flux on each channel side is not uniform in Figure 5.9, not same as assumption in Thome model in Figure 5.11. According to the flow pattern in Figure 5.8, Taylor flow is used to calculate liquid film thickness [80]. For the adiabatic gas-liquid two phase flow in micro-channels, a Taylor flow usually appears as shown in Figure 5.13. The bubble has a hemispherical head and a cylindrical body. With the movement of the bubble, the bubble size, shape and length almost remain unchanged. The liquid film between the bubble and the inner wall keeps uniform thickness. Subcooled flow boiling in Unal model [81] is introduced for bubble grow time calculation in the modified model.

The comparison between modified model and experiment is shown in Figure 5.14. It's clear to see a good match is achieved in most points in Figure 5.14(a). However, there are still two zones with poor match. One is in the low vapor quality zone, where the experimental data have high uncertainties. As shown in Figure 5.14(b) and (c), except the first point with large uncertainty as shown in Figure 5.7, the experiment results are well matched with simulation results of modified model. Another is deep channel (MC3), where the single-phase cooling is dominant with a poor flow boiling performance. Furthermore, the non-uniformity of heat flux on the wall of MC3 is not reflected in the model. To improve the accuracy of model prediction is planned in the future work.

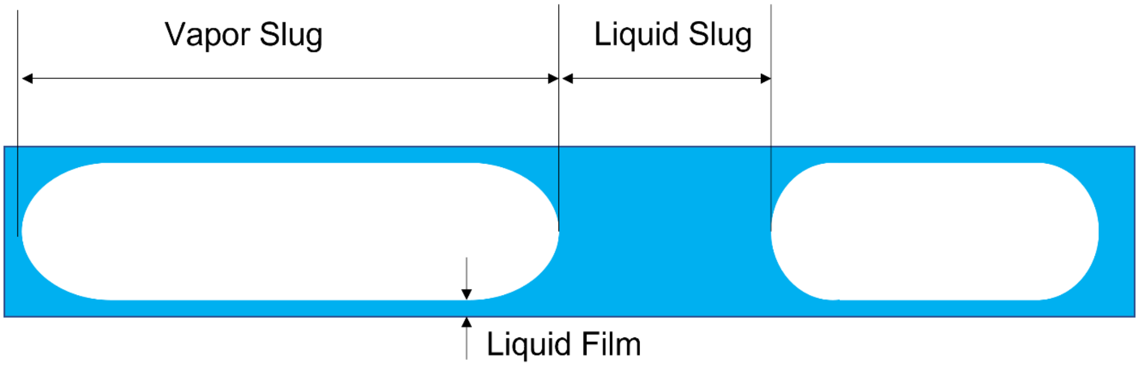

Figure 5.13 Taylor flow

5.4 Summary

The channel height impact on the flow boiling performance was experimentally investigated based on heat transfer measurement and visualization via a high-speed camera. According to the experiment results, the sample MC2 (channel height=1mm) shows the best heat transfer capability (the highest heat flux under case temperature limit) in all

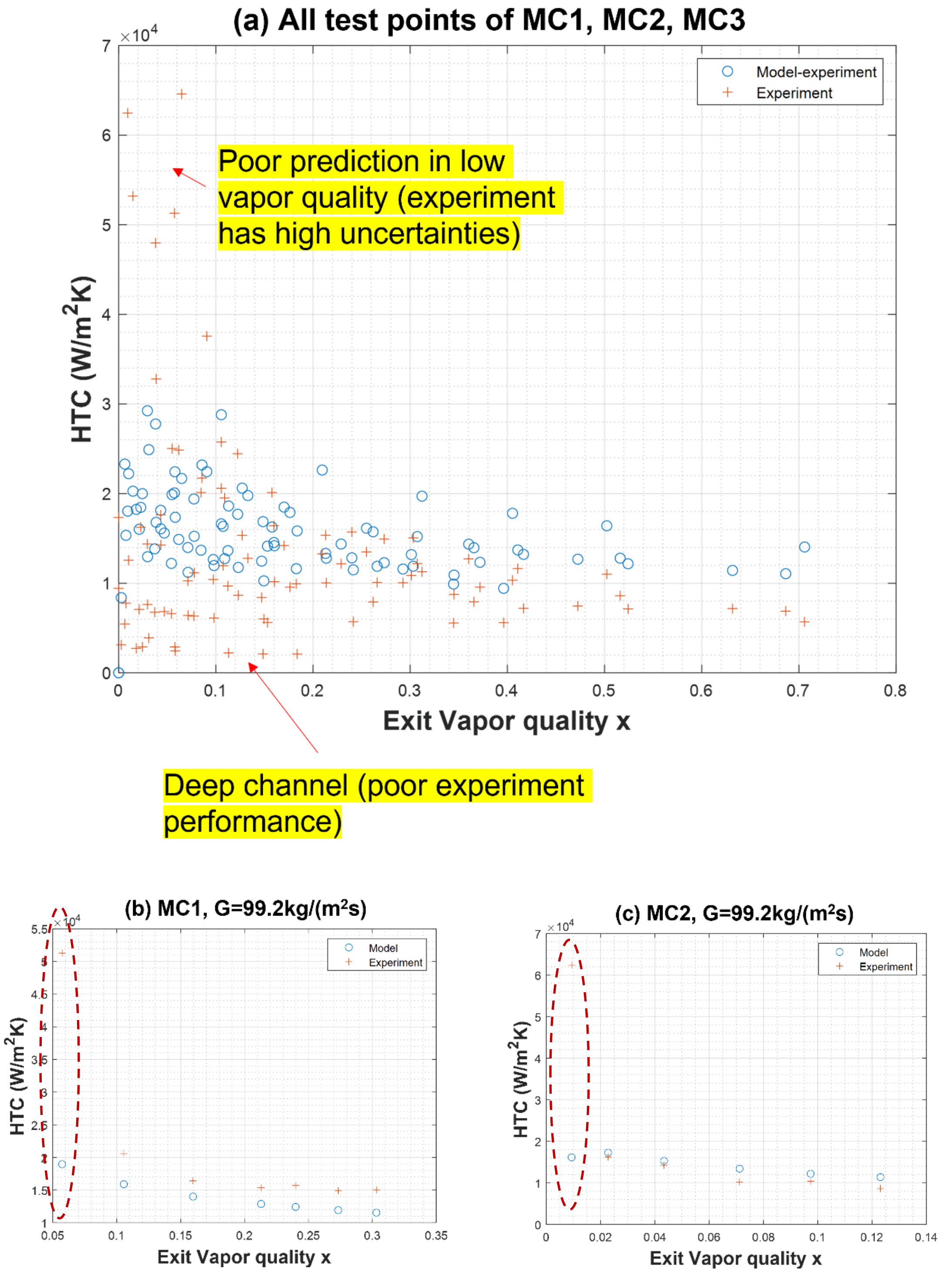

Poor prediction in low vapor quality (experiment has high uncertainties)

Deep channel (poor experiment performance)

Figure 5.14 HTC vs. Exit vapor quality comparison of modified model and experiment results: (a) All test points of MC1, MC2, MC3; (b) MC1, G=99.2kg/(m^2s); (c) MC2, G=99.2kg/(m^2s) testing conditions, with maximum 1050W@ 99.2kg/(m^2s). MC2 has the lowest T_{c_avg} at the same heat flux and the lowest thermal resistance R_{th} with minimum 0.074°C/W @ 99.2 kg/(m^2s). MC1 and MC2 have a good flow boiling performance in two-phase regime, while MC3 (channel height =1.5mm) is occupied by subcooled liquid flow, delaying the ONB to occur under a higher heat flux, resulting in the single-phase convection is the dominant heat transfer mode at the bottom of the channel. Compared MC1 and MC2, MC1 has a larger exit vapor quality and effective heat transfer coefficient, and a smaller case temperature oscillation, reflecting a good flow boiling performance, however, limited by case temperature constrain, the maximum heat flux is smaller than MC2. In the contrast, MC2 has a smaller pressure drop oscillation. The experiment results are compared with flow boiling model. Based on Thome model, the model is modified by introducing subcooled flow and Taylor flow as flow pattern. The simulation results have a good match with experiment results of MC1 and MC2 at two-phase regime.

CONCLUSION

In this study, the objective is to achieve a SiC power module with high thermal performance with two-phase mini-channel cooling. Based on this purpose, the study concentrates on the design and optimization of two-phase mini-channel cooling for SiC power module. The achievements from this study are concluded as below.

Simulation-based evaluation of performance of two-phase cooling applied to power module as described in Chapter 2. Based on the simulation results and analysis, the advantages of two-phase cooling include: increased module power density, increased lifetime, improved electrical performance, reduced required cooling fluid flow rate, reduced system size and weight.

The initial design of mini-channel coldplate for power module fabricated by 3D printing on aluminum in Chapter 3. HFE, with a low boiling point, is used as a dielectric coolant in test. The experiment successfully demonstrates the advantages of two-phase cooling vs single-phase cooling. However, a dryout problem can be observed at a low flow rate. The local dryout tends to happen in the region close to the coolant outlet due to the accumulated heat and vapor flow. Another issue is relatively low maximum cooling power capability, caused by low heat transfer efficient. To solve these problems and improve mini-channel performance, water is used to replace HFE, and slot structure, micro-gap and porous structure are introduced in mini-channel respectively. Micro-gap and porous structure have a better thermal performance compared to smooth and slot structure.

Based on previous study, a novel micro-gap structure with reservoir channel is proposed to improve the overall thermal performance of two-phase mini-channel coldplate. The proposed micro-gap structure allows rewetting flow and vapor expansion across the micro-gap, preventing slug formation. At the same time, porous structure utilizes capillary force to hold more liquid on the surface to act as a reservoir The novel design combined micro-gap and porous structure is demonstrated on a copper plate and reduced case temperature significantly compared with conventional micro-gap mini-channel. An invention disclosure has been filed.

Integration of two-phase mini-channel structure on the module baseplate in Chapter 4. A power module with integrated two-phase mini-channel on the baseplate is proposed, which has a significant reduction of thermal resistance by removal of baseplate and thermal interface material. Furthermore, to remove the baseplate with a function as a heat spreader, a higher HTC cooling is needed. Therefore, two-phase mini-channel is one of the best solutions in this case, which enhances the overall thermal performance of power module.

Study on the effect of channel height on two-phase cooling performance by experiment in Chapter 5. The channel height impact on the flow boiling performance was experimentally investigated based on heat transfer measurement and visualization via a high-speed camera. The experiment results are compared with a modified flow boiling model. The results are helpful to better understand the impact of a key design parameter on the flow boiling in mini-channels for power module cooling applications.

For the further development of power module with integrated mini-channel coldplate, the plans are made to manufacture the proposed micro-gap structure with reservoir channel by chemical wet etch. On the other hand, an optimal flow boiling model is in study, which is helpful to predict the thermal performance of mini-channel coldplate in different dimension and geometry.

REFERENCES

[1] Overview of the DOE VTO Electric Drive Technologies R&D Program, June 7, 2016, Online source.

[2] 2015 International Technology Roadmap for Semiconductors (ITRS), Online source.

[3] 2015 Naval Power and Energy Systems Technology Development Roadmap, Online source.

[4] E. Santi, S. Eskandari, B. Tian, K. Peng, “Power Electronic Modules,” *Power Electronics Handbook* 4e, Ch. 6, Elsevier, 2018

[5] T. Hitachi, H. Gohara, F. Nagaune, “Direct Liquid Cooling IGBT Module for Automotive Applications,” online source, *https://www.fujielectric.com/company/tech/pdf/58-02/FER-58-2-055-2012.pdf*.

[6] K. Hussein, M. Ishihara, N. Miyamoto, Y. Nakata, T. Nakano, J. Donlon, E. Motto, “New compact, high performance 7th cooling for EV/HEV inverters,” *IEEE Applied Power Electronics Conference and Exposition (APEC)*, 2015, pp. 1343 – 1346.

[7] Z. Liang, “Integrated double sided cooling packaging of planar SiC power modules,” IEEE Ener. Conv. Cong. and Expo. (ECCE), 2015, pp. 4907-4912.

[8] B. McPherson, B. McGee, D. Simco, K. Olejniczak, B. Passmore, "Direct liquid cooling of high performance Silicon Carbide (SiC) power modules," *IEEE Inter. Workshop on Inte. Power Pack. (IWIPP)*, 2017, pp.1-5.

[9] D.B. Tuckerman, R.F.W. Pease, High-performance heat sinking for VLSI, Electron Device Letters, IEEE, 2(5) (1981) 126-129.

[10] L. Doretti, C. Zilio, S. Mancin, A. Cavallini, "Condensation flow patterns inside plain and microfin tubes: a review," International Journal of Refrigeration, No.36, 2013, pp. 567-587.

[11] Wenming Li, Fanghao Yang, Tamanna Alam, Jamil Khan, Chen Li, "Experimental and theoretical studies of critical heat flux of flow boiling in microchannels with microbubble-excited high-frequency two-phase oscillations," International Journal of Heat and Mass Transfer, No.88, 2015, pp. 368-378.

[12] Wenming Li, Fanghao Yang, Tamanna Alam, Xiaopeng Qu, Benli Peng, Jamil Khan, Chen Li, "Enhanced flow boiling in microchannels using auxiliary channels and multiple micronozzles (I): Characterizations of flow boiling heat transfer," International Journal of Heat and Mass Transfer, No.116, 2018, pp. 208-217.

[13] Wenming Li, Fanghao Yang, Tamanna Alam, Xiaopeng Qu, Benli Peng, Jamil Khan, Chen Li, "Enhanced flow boiling in microchannels using auxiliary channels and multiple micronozzles (II): Enhanced CHF and reduced pressure drop," International Journal of Heat and Mass Transfer, No.115, 2017, pp. 264-272.

[14] Wenming Li, Xiaopeng Qu, Tamanna Alam, Fanghao Yang, Wei Chang, Jamil Khan, and Chen Li, "Enhanced flow boiling in microchannels through integrating multiple micro-nozzles and reentry microcavities," *Appl. Phys. Lett.* 110, 014104, 2017.

[15] J.R. Thome, Boiling in microchannels: a review of experiment and theory, International Journal of Heat and Fluid Flow, 25(2) (2004) 128-139.

[16] J.R. Thome, State-of-the-art overview of boiling and two-phase flows in microchannels, Heat Transfer Engineering, 27(9) (2006) 4-19.

[17] B. Agostini, M. Fabbri, J.E. Park, L. Wojtan, J.R. Thome, B. Michel, State of the art of high heat flux cooling technologies, Heat Transfer Engineering, 28(4) (2007) 258-281.

[18] P. Cheng, G. Wang, X. Quan, Recent Work on Boiling and Condensation in Microchannels, Journal of Heat Transfer, 131(4) (2009) 043211-043215.

[19] D. Liu, P.-S. Lee, S.V. Garimella, Prediction of the onset of nucleate boiling in microchannel flow, International Journal of Heat and Mass Transfer, 48(25-26) (2005) 5134-5149.

[20] S.G. Kandlikar, Fundamental issues related to flow boiling in mini-channels and microchannels, Experimental Thermal and Fluid Science, 26(2-4) (2002) 389-407.

[21] P. Cheng, H.Y. Wu, Mesoscale and Microscale Phase-Change Heat Transfer, in: J.P.H.A.B.-C. George A. Greene, I.C. Young (Eds.) Advances in Heat Transfer, Elsevier, 2006, pp. 461-563.

[22] S.G. Kandlikar, W.K. Kuan, D.A. Willistein, J. Borrelli, Stabilization of flow boiling in microchannels using pressure drop elements and fabricated nucleation sites, Journal of Heat Transfer, 128(4) (2006) 389-396.

[23] T. Zhang, T. Tong, J.-Y. Chang, Y. Peles, R. Prasher, M.K. Jensen, J.T. Wen, P. Phelan, Ledinegg instability in microchannels, International Journal of Heat and Mass Transfer, 52(25-26) (2009) 5661-5674.

[24] T. Zhang, J.T. Wen, Y. Peles, J. Catano, R. Zhou, M.K. Jensen, Two-phase refrigerant flow instability analysis and active control in transient electronics cooling systems, International Journal of Multiphase Flow, 37(1) (2011) 84-97.

[25] G. Wang, P. Cheng, A.E. Bergles, Effects of inlet/outlet configurations on flow boiling instability in parallel microchannels, International Journal of Heat and Mass Transfer, 51(9-10) (2008) 2267-2281.

[26] L. Wojtan, R. Revellin, J.R. Thome, Investigation of saturated critical heat flux in a single, uniformly heated microchannel, Experimental Thermal and Fluid Science, 30(8) (2006) 765-774.

[27] C.J. Kuo, Y. Peles, Flow boiling instabilities in microchannels and means for mitigation by reentrant cavities, Journal of Heat Transfer-Transactions of the Asme, 130(7) (2008).

[28] C.J. Kuo, Y. Peles, Pressure effects on flow boiling instabilities in parallel microchannels, International Journal of Heat and Mass Transfer, 52(1-2) (2009) 271-280.

[29] S. Vafaei, D. Wen, Critical heat flux (CHF) of subcooled flow boiling of alumina nanofluids in a horizontal microchannel, Journal of Heat Transfer, 132(10) (2010) 102404-102407.

[30] S.-S. Hsieh, C.-Y. Lin, Correlation of critical heat flux and two-phase friction factor for subcooled convective boiling in structured surface microchannels, International Journal of Heat and Mass Transfer, 55(1-3) (2012) 32-42.

[31] H.Z. Cao, H.B. Xu, N. Liang, C.Q. Tian, Experiment investigation of R134a flow boiling process in microchannel with cavitation structure, Heat Transfer Engineering, 32(7-8) (2011) 542-553.

[32] H.T. H. Kubo, and Hiroshi Honda, Effects of size and number density of micro-reentrant cavities on boiling heat transfer from a silicon chip immersed in degassed and gas-dissolved FC-72, Journal of Enhanced Heat Transfer, 6(2-4) (1999) 151-160.

[33] W. Hailei, R.B. Peterson, Enhanced boiling heat transfer in parallel microchannels with diffusion brazed wire mesh, Components and Packaging Technologies, IEEE Transactions on, 33(4) (2010) 784-793.

[34] A.K.M.M. Morshed, F. Yang, M. Yakut Ali, J.A. Khan, C. Li, Enhanced flow boiling in a microchannel with integration of nanowires, Appl. Therm. Eng., 32(0) (2012) 68-75.

[35] N. Singh, V. Sathyamurthy, W. Peterson, J. Arendt, D. Banerjee, Flow boiling enhancement on a horizontal heater using carbon nanotube coatings, International Journal of Heat and Fluid Flow, 31(2) (2010) 201-207.

[36] S. Krishnamurthy, Y. Peles, Flow boiling heat transfer on micro pin fins entrenched in a microchannel, Journal of Heat Transfer, 132(4) (2010) 041007-041010.

[37] D. Guo, J.J. Wei, Y.H. Zhang, Enhanced flow boiling heat transfer with jet impingement on micro-pin-finned surfaces, Appl. Therm. Eng., 31(11–12) (2011) 2042-2051.

[38] P. Wang, P. McCluskey, and A. Bar-Cohen, “Two-phase liquid cooling for thermal management of IGBT power electronic module,” *J. Electron. Packag.*, vol. 135, 2013, pp. 021001-1 – 021001-11.

[39] N. Malu, D.Bora, S. Nakanekar, and S. Tonapi, “Thermalmanagement of an IGBT module using two-phase cooling,” in Proc. IEEE Intersoc. Conf. Therm. Thermomech. Phenom. Electron. Syst., 2014, pp. 1079–1085.

[40] I. Aranzabal ; I. Martinez de Alegria ; J.I. Garate ; J. Andreu ; N. Delmonte, “Two-phase liquid cooling for electric vehicle IGBT power module thermal management,” IEEE Interna. Conf. on Comp., Power Elec. and Power Engin. (CPE-POWERENG), 2017, pp. 495-500.

[41] A. Cebi, A. Celen, A. H. Donmez, Y. Karakoyun, P. Celen, M. S. Cellek, A. S. Dalkilic, T. Taner and S. Wongwises, “A review of flow boiling in mini and microchannel for enhanced geometries,” *Journal of Thermal Engineering*, vol. 4, No. 3, 2018, pp. 2037-2074.

[42] Sujoy Kumar Saha, GianPiero Celata, Satish G.Kandlikar, “Thermofluid Dynamics of Boiling in Microchannels,” *Advances in Heat Transfer*, Vol. 43, 2011, pp. 77-226.

[43] Wolfseed offical website, online source, https://www.wolfspeed.com/xm3-power-module-family.

[44] Infineon offical websit, online source, https://www.infineon.com/dgdl/Infineon-FF450R12KT4P-DS-v02_00-EN.pdf

[45] Infineon offical websit, online source, https://www.infineon.com/dgdl/Infineon-FS380R12A6T4B-DataSheet-v03_01-EN.pdf

[46] https://www.wolfspeed.com/media/downloads/179/CAS120M12BM2.pdf

[47] Fanghao Yang, Xianming Dai, Chen Li, “High frequency microbubble-switched oscillations modulated by microfluidic transistors,” Appl. Phys. Lett. 101, 073509, 2012.

[48] J. Due, S. Nielsen, and R. Nielsen, “Lifetime investigation of high power IGBT modules,” in *Proc. 14th Euro. Conf. Power Elec. Appl.,* Aug.-Sept. 2011, pp. 1-8.

[49] Kang Peng, Enrico Santi, “Analytical Loss Model for Power Converters with SiC MOSFET and SiC Schottky Diode Pair,” Energy Conversion Congress and Exposition (ECCE), 2015 IEEE, pp. 6153-6160, 2015

[50] S. Li, L. M. Tolbert, F. Wang and F. Z. Peng, "P-cell and N-cell based IGBT module: Layout design, parasitic extraction, and experimental verification," 2011 Twenty-Sixth Annual IEEE Applied Power Electronics Conference and Exposition (APEC), Fort Worth, TX, 2011, pp. 372-378

[51] M. Feurtado, B. McPherson, D. Martin, T. McNutt, Ma. Schupbach, W. A. Curbow, J. Hayes, B. Sparkman, “High-Performance 300 kW 3-Phase SiC Inverter Based on Next Generation Modular SiC Power Modules,” PCIM Europe, pp.7-9, 2019.

[52] 3M official website, online source, https://www.3m.com/3M/en_US/company-us/all-3m-products/~/3M-Novec-7100-Engineered Fluid/?N=5002385+3290667247&rt=rud.

[53] J. Ma, W. Li, C. Ren, J. A. Khan, C. Li, “Realizing highly coordinated, rapid and sustainable nucleate boiling in microchannel on HFE-7100,” International Journal of Heat and Mas Transfer, 133, 2019, pp. 1219-1229

[54] D. Cooke and S. G. Kandlikar, "Pool Boiling Heat Transfer and Bubble Dynamics Over Plain and Enhanced Microchannels," Journal of Heat Transfer-Transactions of the Asme, vol. 133, May 2011.

[55] S. G. Kandlikar, T. Widger, A. Kalani, and V. Mejia, "Enhanced Flow Boiling Over Open Microchannels With Uniform and Tapered Gap Manifolds," Journal of Heat Transfer-Transactions of the Asme, vol. 135, Jun 2013.

[56] L. F. Yin, P. X. Jiang, R. N. Xu, H. W. Hu, and L. Jia, "Heat transfer and pressure drop characteristics of water flow boiling in open microchannels," International Journal of Heat and Mass Transfer, vol. 137, pp. 204-215, Jul 2019.

[57] M.E. Poniewski, J.R. Thome, “Nucleate Boiling on Micro-structured Surfaces”. Heat Transfer Research Inc., College Station, TX, 2008.

[58] K.N. Rainey, G. Li and S.M. You, “Flow boiling heat transfer from plain and microporous coated surfaces in subcooled FC-72,” ASME J Heat Transfer, 123 (2001), pp. 918-925

[59] H. Wang and R.B. Peterson, “Enhanced boiling heat transfer in parallel microchannels with diffusion brazed wire mesh”, IEEE Trans Compon Packag Technol, 33 (2010), pp. 784-793

[60] Y. Sun, L. Zhang, H. Xu and X. Zhong, “Subcooled flow boiling heat transfer from microporous surfaces in a small channel”, Int J Therm Sci, 50 (2011), pp. 881-889

[61] A.E. Bergles, M.C. Chyu, Characteristics of nucleate pool boiling from porous metallic coatings, J. Heat Transf.-Trans. ASME 104 (1982) 279e285.

[62] K. Nishikawa, Y. Fujita, Nucleate boiling heat transfer and its augmentation, Adv. Heat Transf. 20 (1990) 1-82.

[63] P.J. Marto, V.J. Lepere, Pool boiling heat transfer from enhanced surfaces to dielectric fluids, J. Heat Transf.-Trans. ASME 104 (1982) 292e299.

[64] S.M. You, T.W. Simon, A. Bar-Cohen, A technique for enhancing boiling heat transfer with application to cooling of electronic equipment, IEEE Trans. Compon. Packag. Manuf. Tech. 15 (1991) 90-96.

[65] J.H. Kim, Enhancement of Pool Boiling Heat Transfer Using ThermallyConductive Microporous Coating Techniques, Ph.D. thesis, The University of Texas at Arlington, Arlington, TX, USA, 2006.

[66] MaxQ Technology, coldplate datasheet, http://maxqtechnology.com/wp-content/uploads/2019/01/007-MXQ-01-new1-1.9.19.pdf

[67] Wieland MicroCool, datasheet, https://www.microcooling.com/wp-content/uploads/2019/08/CP3012_datasheet.pdf

[68] M.-S. Shin, S. Senguttuvan, and S.-M. Kim, "Investigations of Flow and Heat Transfer Characteristics in a Channel Impingement Cooling Configuration with a Single Row of Water Jets," Energies, vol. 14, no. 14, pp. 4327, 2021.

[69] L. Lin and R. Ponnappan, "Heat transfer characteristics of spray cooling in a closed loop," International Journal of Heat and Mass Transfer, vol. 46, no. 20, pp. 3737-3746, 2003.

[70] A. S. Salman, “Enhanced Heat Transfer in Spray Cooling Through Surface Modifications: An Experimental and Computational Study,” Ph.D dissertation, University of South Carolina, 2019.

[71] Choi, C., D. Yu, and M. Kim, Adiabatic two-phase flow in rectangular microchannels with different aspect ratios: Part I–Flow pattern, pressure drop and void fraction. International Journal of Heat and Mass Transfer, 2011. 54(1-3): p. 616-624.

[72] Choi, C., D. Yu, and M. Kim, Adiabatic two-phase flow in rectangular microchannels with different aspect ratios: Part II–bubble behaviors and pressure drop in single bubble. International journal of heat and mass transfer, 2010. 53(23-24): p. 5242-5249.

[73] Soupremanien, U., et al., Influence of the aspect ratio on boiling flows in rectangular mini-channels. Experimental thermal and fluid science, 2011. 35(5): p. 797-809.

[74] Singh, S., et al., Impact of aspect ratio on flow boiling of water in rectangular microchannels. Experimental Thermal and Fluid Science, 2008. 33(1): p. 153-160.

[75] Fu, B.-R., C.-Y. Lee, and C. Pan, The effect of aspect ratio on flow boiling heat transfer of HFE-7100 in a microchannel heat sink. International journal of heat and mass transfer, 2013. 58(1-2): p. 53-61.

[76] Markal, B., O. Aydin, and M. Avci, Effect of aspect ratio on saturated flow boiling in microchannels. International Journal of Heat and Mass Transfer, 2016. 93: p. 130-143.

[77] Darin J. Sharar, Nicholas R. Jankowski; Brian Morgan, "Thermal performance of a Direct-Bond-Copper Aluminum Nitride manifold-microchannel cooler," 2010 26th Annual IEEE Semiconductor Thermal Measurement and Management Symposium (SEMI-THERM), Santa Clara, CA, USA, 2010

[78] J.R.Thome, V. Dupont, A.M. Jacobi, “Heat transfer model for evaporation in microchannels. Part I: presentation of the model,” International Journal of Heat and Mass Transfer 47 (2004) 3375–3385

[79] V. Dupon, J.R. Thome, A.M. Jacobi, “Heat transfer model for evaporation in microchannels part II: comparison with the database,” International Journal of Heat and Mass Transfer 47 (2004) 3387–3401

[80] Chaohong Guo, Jie Tao, Yuyan Jiang, Yanhong Sun, Tao Wang, “Measurement and theoretical analysis of transient liquid film during micro-channel flow boiling,” International Journal of Multiphase Flow 130 (2020) 103365

[81] H.C. Unal, “Maximum bubble diameter, maximum bubble-growth time and bubble-growth rate during the subcooled nucleate flow boiling of water up to 17.7 mn/m2,” Int. J. Heat Mass Transfer. Vol.19, 1976, pp. 643-649